Scuola Normale Superiore di Pisa

Classe di Scienze

PhD Thesis

TD-DFT and TD-DFT/PCM approaches to molecular electronic excited states in gas phase and in solution

---

Author:
Ciro Achille GUIDO

Supervisors:

Prof. J. TOMASI

Prof. B. MENNUCCI

External advisors:

Prof. C. ADAMO

Prof. E. PERPÈTE

President of the PhD Commission:
Prof. V. BARONE

Years 2008 - 2010

In memory of Ciro Guido,
my grandfather

To Maria, Umberto and Dario.

Acknowledgements

I would thank some people that have been really important during my PhD and so for the realization of this Thesis.

Professor Tomasi, his advice has been crucial in these three years. I became a theoretical chemist thanks to his scientific knowledge. He is, for sure, the person who most inspired me.

Professor Mennucci, who patiently followed and supervised me during my PhD. I owe to her my knowledge of solvation models and their applications in quantum chemistry, but especially, I thank her for the huge guidance.

I would like to sincerely thank Prof. Adamo and Dr. Ciofini. I owe a lot to them in scientific and human terms. My Parisian experience has enriched me in both these areas. A special thank is also for their group in Paris: Cyril, Stefania, Guillame, Tanguy, Giuseppe, Roberto, Vincent, Fred, Vinca and Diane.

I am grateful to Prof. Jacquemin, with whom I have worked for some papers and who, together with Carlo, introduced me to the fun part of being a scientist.

I would like to thank Prof. Barone, for all the opportunities he gave me during these years. I also had the pleasure of working with him for the publication of one paper.

A special thanks to Dr. Cappelli, who has also become a friend. Thanks for all the advice during these years.

Finally I would like to thank my group in Pisa for these years and the ties that have been created between us: Carles, Aurora, Filippo, Alessandro, Stefano, Christian....

and Alberto, who is no more. But it is as if he was here.

Contents

Chapter 1

Introduction

The study of molecular systems in their electronic excited states is one of the major issues in many fields of physics, chemistry, biology and material science with very different applications, going from diagnostic tools in medicine to probes in analytical chemistry, or new devices for technological applications or energetics [1],[2],[3]. Moreover, the absorption of visible light and its conversion to other forms of energy is at the heart of some of the most fundamental processes in biology, such as photosynthesis.
The electronic structure of a molecule is determined by the quantum behavior of electrons inside the system, resulting in molecular states with different symmetries and different spin multiplicities. Many processes can occur when the light is absorbed by a molecule, and in particular, the phenomena we here concentrate on are of electronic origin.
Let us illustrate these processes by a Jablonsky diagram in figure 1.1. Jablonsky diagrams can be formulated in a variety of forms, depending on the processes and the systems we are interested to study. The figure here reported shows a typical energy level diagram involved in the dynamics of processes[1] of a molecule in gas phase, starting from a singlet ground state. The transitions between states are depicted as vertical lines to illustrate the instantaneous nature of light absorption, as transitions occur in about 10^{-15} s, a time too short for significant displacement of nuclei, in according to the Franck-Condon principle. During the first absorption step (A in the figure), the molecule is excited from the ground to any (singlet) excited state. The excited molecule then tends to release the excess of energy by fast relaxation to lower electronic states. This could be done in a non-radiative way through the so-called internal conversion (IC) process, or in a radiative way by emitting light, i.e. a fluorescence process (F in the figure). The non-radiative process, IC, is esti-

[1]We excluded a number of other processes, such as quenching or energy transfer

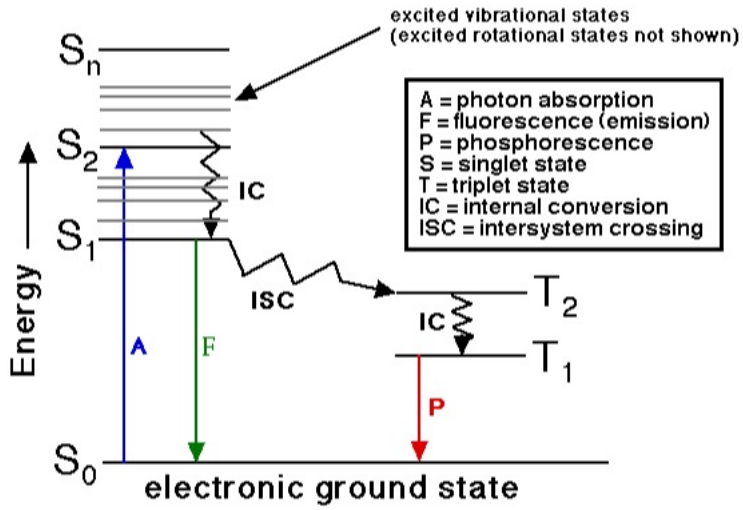

Figure 1.1: A general Jablonsky diagram

mated to be in the timescale of picoseconds, while the radiative lifetime of the lowest excited singlet state (S_1) is often much larger, in the range of nanoseconds. When a molecule possesses a heavy atom, large spin-orbit coupling could occur which can open up more channels for absorption and emission. These can be excitations between triplet states, as well as between triplet and singlet states [2]. In the latter case, the triplet excited state is initially populated by the inter-system-crossing (ISC) process, which is in the time scale of nanoseconds. In the present Thesis only the A and F processes will be analyzed together with the geometrical relaxation accompanying the photophysical evolution of the excited system. In such an analysis another *external* factor will be introduced, namely the effects of the environment. The environment in which a molecule is immersed can in fact alter its states and the corresponding spectroscopic signals. When absorption and emission UV/vis spectra are measured in solvents of different polarity, it is found that the positions, intensities, and shapes of the bands are usually modified. These effects are generally indicated as solvatochromism.

A solvent behaves both as a macroscopic continuum characterized only by physical constants such as density, dielectric constant, index of refraction etc., and a discontinuum medium which consists of individual, mutually interacting solvent molecules. According to the extent of these interactions, there are

[2]Transitions between states of different spin multiplicities, such as triplet-singlet transitions, are governed by the spin selection rule. They are absolutely forbidden when the spin-orbit coupling is absent.

solvents with a pronounced internal structure (e.g. water) and others in which the interaction between the solvent molecules is small (e.g. hydrocarbons). The interactions between species in solvents (and in solutions) are too strong to be treated by the laws of the kinetic theory of gases, yet too weak to be treated by the laws of solid-state physics. Thus, the solvent is neither an indifferent medium in which the dissolved material diffuses in order to distribute itself evenly and randomly, nor does it possess an ordered structure resembling a crystal lattice. Nevertheless, the long-distance ordering in a crystal corresponds somewhat to the local ordering in a liquid. Thus, neither of the two possible models – the gas and crystal models – can be applied to solutions without limitation.
The changes in excited states induced by the environment are a result of physical intermolecular solute–solvent interaction forces. More in detail, we can individuate two main categories: the first category comprises the so-called directional, induced and dispersion forces, which are non-specific and cannot be completely saturated; the second group consists of specific interactions, such as hydrogen-bonding forces, or electron-pair donor acceptor forces. The main interactions are electrostatic in origin, such as the polarity and the local organization of solvent molecules around the solute molecule. This behavior gives rise to a large use of averaged pictures to model the solute-solvent interactions, such as continuum models. However, if we want to treat all those spectral changes which arise from alteration of the chemical nature of the solvated molecules by the medium, (such as proton or electron transfer between solvent and solute, solvent-dependent aggregation, ionization, complexation, or isomerization equilibria) or specific interactions, such as hydrogen bonding, a discrete description also for solvent molecules is needed.

From the above discussion, it is understandable that a detailed analysis of the excited states requires a variety of experimental techniques and this also applies to theoretical simulations. Indeed different computational schemes are required to understand the properties of different states and to model the effects that the solvent has on them.
The aim of the research presented in this Thesis is adressed to investigate the potentiality of the Density Functional Theory (DFT) methods in their time dependent formulation (TD-DFT), and the reliability offered by its combination with a Polarizable Continuum Model (PCM) for the solvent, to determine excitation energies, structures and properties of excited state of molecules in gas and solvent phase.
More in detail, this Thesis has focused on two main topics.
The first is the critical analysis of TD-DFT methods when applied to the cal-

culation of molecular excited state energies and properties. The goal is to assess performances of exchange-correlation functionals and to individuate diagnostic tools to analyse the achieved results. This first part is propedeutic to individuate a good computational protocol within the Linear Response Kohn-Sham (LR-KS) scheme to be coupled with the Time Dependent Polarizable Continuum Model (TD-PCM) approach to treat solute-solvent interactions in describing excited states of solvated molecules. To this aim two alternative couplings between TD-DFT and PCM are tested in describing charge transfer (CT) excitations of large systems in solution and to assess the excitation mechanism in TICT and/or PICT systems. Finally a new self-consistent strategy to describe solvated excited states is developed and implemented whitin the TD-DFT method.
The text is organised as follows:

- Chapter 2 presents the theoretical background, with a short review of DFT and TD-DFT methods, together with a critical analysis of their limits and potentialities on the basis of newly developed diagnostic tools. In parallel a detailed study of accuracy and relability of TD-DFT in determining excited state structures is presented and discussed.

- Chapter 3 presents the extension of TD-DFT approaches to solvation continuum models within PCM framework. Different strategies of possible couplings between TD-DFT and PCM are critically compared when applied to solvent-sensitive molecular probes. Finally, a new self-consistent scheme for calculating excitation enegies in solvent is developed and numerical tests are performed in comparison with precedent approaches.

- Conclusion remarks and future directions are given in chapter 4.

Chapter 2

TD-DFT description of molecular excited states

2.1 Introduction

One of the major problems in reproducing energies and properties of electronic excited states is due to the computational cost of the method to determine the electronic structure.
Nowadays, ab initio methods allow to accurately determine a large set of properties for molecular systems in their ground state. On the contrary, calculations of excited-state properties, including emission phenomena such as fluorescence and phosphorescence, are still a challenge, because they require the nontrivial task of an accurate determination of excited-state structures [4].
On the one hand, fast and cheap purposely tailored semiempirical approaches lack consistency when applied to families of molecules not included in the original training sets. On the other hand, more reliable theoretical tools, such as EOM-CC [5],[6], MR-CI [7],[8], CAS-PT2 [9],[10],[11], SAC-CI [12], [13], are too expensive to afford the study of the large systems of chemical and industrial interest.

At the same time, it is well established that the Kohn-Sham (KS) approach to density functional theory (DFT) can provide an accurate description of a large number of physicochemical properties for the ground electronic state [14]. Furthermore, its current accuracy/cost ratio is significantly lower than that of more sophisticated post-Hatree-Fock approaches. In a similar manner, the time-dependent density functional theory (TD-DFT)[15] could be a viable alternative for the evaluation of excited-state geometries and properties. In the Linear Response-Kohn Sham (LR-KS) scheme [16] of the TD-DFT formulation, based on the extension to the action functional of Hohenberg and

Kohn theorems, as in random phase approximation [17] and Tamm-Damcoff approximation [18], a pseudoeigenvalues equation, where the Lagrange multiplier matrix contains excitation energies, can be written down. Consequently, first-order molecular properties can be calculated by analytical derivatives [19],[20],[21] by using a Z-vector approach [22], and this introduces the calculation of third-order derivatives of exchange-correlation (XC) functional used. The TD-DFT approach presents the typical problems of ground-state DFT methods: the exact XC functional form is unknown, the approximated functionals introduce self-interaction (SI) errors, the asymptotic behavior of XC potential could be incorrect, and the use of a single determinant makes DFT inadequate for cases presenting a near degeneracy of several configurations [14],[23]. Besides, additional drawbacks originating in the LR formulation exist. Actually, almost all implementations of TD-DFT are based on the adiabatic approximation, for which the action functional could be written by using the XC energy functional used in Kohn-Sham time-independent equation. In other words, there are no memory effects, the only time dependence is indirectly taken into account by the density, and an instantaneous reaction of XC potential to the density variations is assumed [24]. From a more applicative point of view, the use of TD-DFT approach presents some difficulties in describing charge transfer and Rydberg excitations. This originates in the form of the operators in the LR-KS equations and the subsequent incapability to follow the reorganization of charge between two separated regions of space or between orbitals of different spatial extent [24],[25].
Despite these limits, there are extended studies that show the very good performances of TD-DFT in reproducing excitation energies and absorption spectra [26], [27], [28], [29], [30].
In this chapter, after an introduction of TD-DFT methods, some of the problems and the difficulties of the LR-KS scheme are critically analysed by introducing an index to test the vertical excitations calculated [31] and a benckmark of the performances in reproducing excited state structures is also presented. The latter constitutes the first systematic study of this type, to the best of our knownledge [32].

2.2 Brief review of Density Functional Theory

The material world of everyday experience, as studied by chemistry and condensed-matter physics, is built up from electrons and a hundred kinds of nuclei, where the basic interaction is electrostatic or Coulombic. All electrons in the lighter elements, and the chemically important valence electrons in most elements, move at speeds much less than the speed of light, and so are non-relativistic. As

nuclei are more massive than electrons, we can assume the Born-Oppenheimer approximation to obtain two Schrödinger equations, one for the electrons and one for the nuclei. We will focus only in the electronic part. The non relativistic time-indipendent many-electron problem becames (in atomic units) [33]:

$$\hat{H}^e|\Psi(\mathbf{x}_1...\mathbf{x}_i...\mathbf{x}_N)\rangle = E|\Psi(\mathbf{x}_1...\mathbf{x}_i...\mathbf{x}_N)\rangle \tag{2.1}$$

Where:

$$\mathbf{x} = \mathbf{r}\sigma \tag{2.2}$$

$$\hat{H}^e = \sum_i^N \hat{t}_i + \sum_i^N \hat{v}_{ext}(\mathbf{r}_i) + \frac{1}{2}\sum_{i,j\neq i}^N \frac{1}{|\mathbf{r}_i - \mathbf{r}_j|} = \hat{T} + \hat{V} + \hat{W} \tag{2.3}$$

$$\hat{t}_i = -\frac{1}{2}\nabla_i^2 \tag{2.4}$$

$$\hat{v}_{ext}(\mathbf{r}_i) = \sum_\alpha^{N_{nuc}} \frac{Z_\alpha}{|\mathbf{r}_i - \mathbf{R}_\alpha|} \tag{2.5}$$

The many-particle wave function $\Psi(\mathbf{x}_1..., \mathbf{x}_i, ..., \mathbf{x}_N)$ contains all the informations of the system. When one is interested in the values of observables corresponding to k-body operators

$$\mathcal{O}^{(k)}[\Psi] = \langle\Psi|\hat{\mathcal{O}^{(k)}}|\Psi\rangle \tag{2.6}$$

the k-order reduced density matrix it suffices

$$\begin{aligned}&\Gamma^{(k)}(\mathbf{x}'_1, ..., \mathbf{x}'_k|\mathbf{x}_1, ..., \mathbf{x}_k) = \\ &\tbinom{N}{k}\int d\mathbf{x}_{k+1}...d\mathbf{x}_N\Psi(\mathbf{x}'_1, ..., \mathbf{x}'_k, \mathbf{x}_{k+1}..., \mathbf{x}_N)\Psi(\mathbf{x}_1, ..., \mathbf{x}_k, \mathbf{x}_{k+1}, ..., \mathbf{x}_N)\end{aligned} \tag{2.7}$$

$$\langle\Psi|\hat{\mathcal{O}}^{(k)}|\Psi\rangle = \int d\mathbf{x}_1...d\mathbf{x}_k\hat{\mathcal{O}}^{(k)}\Gamma^{(k)}(\mathbf{x}'_1, ..., \mathbf{x}'_k|\mathbf{x}_1, ..., \mathbf{x}_k) \tag{2.8}$$

Most operators of interest are either one or two body operators:

$$\Gamma^{(1)}(\mathbf{x}'_1|\mathbf{x}_1) = N\int d\mathbf{x}_2...d\mathbf{x}_N\Psi(\mathbf{x}'_1, \mathbf{x}_2, ..., \mathbf{x}_N)\Psi(\mathbf{x}_1, \mathbf{x}_2, ...\mathbf{x}_N) \tag{2.9}$$

$$\begin{aligned}&\Gamma^{(2)}(\mathbf{x}'_1, \mathbf{x}'_2|\mathbf{x}_1, \mathbf{x}_2) = \\ &\tbinom{N}{2}\int d\mathbf{x}_3...d\mathbf{x}_N\Psi(\mathbf{x}'_1, \mathbf{x}'_2, \mathbf{x}_3..., \mathbf{x}_N)\Psi(\mathbf{x}_1, \mathbf{x}_2, \mathbf{x}_3..., \mathbf{x}_N)\end{aligned} \tag{2.10}$$

The energy is an exact functional solely of the first order density matrix, and

of the diagonal of the second order density matrix:

$$E = \int d\mathbf{x} \left[\tfrac{1}{2}\nabla^2\Gamma^{(1)}(\mathbf{x}|\mathbf{x}')\right]_{\mathbf{x}=\mathbf{x}'} + \int d\mathbf{x} v_{ext}(\vec{\mathbf{x}})\gamma^{(1)}(\mathbf{x}) + \int d\mathbf{x} \int d\mathbf{x}' \tfrac{1}{|\vec{r}-\vec{r}'|}\gamma^{(2)}(\mathbf{x},\mathbf{x}') \tag{2.11}$$

$$\gamma^{(1)}(\mathbf{x}) = \Gamma^{(1)}(\mathbf{x}|\mathbf{x}) \tag{2.12}$$

$$\gamma^{(2)}(\mathbf{x},\mathbf{x}') = \Gamma^{(2)}(\mathbf{x},\mathbf{x}'|\mathbf{x},\mathbf{x}') \tag{2.13}$$

Summing over spin in $\gamma^{(1)}(\mathbf{x})$ the electron density is obtained:

$$\rho(\mathbf{r}) = \sum_{\sigma} \gamma^{(1)}(\mathbf{r}\sigma) \tag{2.14}$$

Since the first order density matrix can be obtained by explicit integration from $\Gamma^{(2)}$:

$$E = E[\Gamma^{(2)}] \tag{2.15}$$

However, given the number of the electrons and the external potential, in principle we have all the information about the system, by solving the Schrödinger equation. Therefore we obtain the wave function and the density of the system: $v_{ext}(\vec{r}) \longrightarrow \rho(\mathbf{r})$.
As $E_{ext} \equiv E_{ext}[\rho(\mathbf{r})]$ (cfr. equations 2.11 and 2.14) we can presume that :

$$E = E[\rho(\mathbf{r})] \tag{2.16}$$

The proof of this statement is given by the first Hohenberg-Kohn theorem [1], whereas the second introduces a variational principle on the energy as a density functional [34]:

Theorem 1 (of Hohenberg and Kohn) *The external potential $v_{ext}(\mathbf{r})$ is (to within an additive constant) a unique functional of the ground state density $\rho(\mathbf{r})$, and therefore :*

$$v_{ext}(\mathbf{r}) \Longleftrightarrow \rho(\mathbf{r})$$

Corollarium 1 *The ground state expectation value of any observable $\hat{\mathcal{O}}$ is a unique functional of the exact ground state density* [2]

$$\mathcal{O}[\rho] = \langle\Psi[\rho]|\hat{\mathcal{O}}|\Psi[\rho]\rangle$$

[1] The first formulation of the theorem (1964) is valid only for non degenerate ground states. However the basic formalism is easily extended to also include degerate cases.

[2] We drop out here the explicit dependence of the density from the electronic coordinate

Therefore:

$$E[\rho] = T[\rho] + W[\rho] + V[\rho] = \mathcal{F}_{HK}[\rho] + V[\rho] \tag{2.17}$$

$\mathcal{F}_{HK}[\rho]$ is the universal HK functional. It is *universal* in the sense that it does not depend on the external potential.

Theorem 2 (variational character of Energy functional) *Given the exact ground state density ρ_0 for an external potential v_0, and a different v-representable density ρ,*

$$E_{v_0}[\rho_0] \leq E_{v_0}[\rho] \tag{2.18}$$

A function $\rho(\mathbf{r})$ is termed pure state v-representable if it is the density of a (possibly degenerate) ground state of the Hamiltonian of the system with some suitably chosen local external potential $v(\mathbf{r})$. By construction, the functionals $F_{HK}[\rho]$ and $E_{v_0}[\rho]$ are defined only for pure-state v-representable functions [14]. However, the original hope that all reasonably well-behaved non negative functions are pure-state v-representable turned to be too optimistic therefore, an extension of the domain of HK functional to arbitrary non-negative functions, integrating to the given particle number N appears desiderable. A possible choice is the Levy-Lieb functional [35],[36], that is defined for all functions $\rho(\mathbf{r})$ which can be represented as the density of some antisymmetric N-particle function. These functions are called *pure state N-representables*.

$$\mathcal{F}_{LL}[\rho] = \inf_{\Psi \to \rho} \langle \Psi | \hat{T} + \hat{W} | \Psi \rangle \tag{2.19}$$

All integrable non-negative functions are N-representable [14],[37], provided that

$$\int dr |\nabla \rho^{1/2}(r)|^2 < +\infty$$

.

Beside the v- and N-representability problems, the form of exact universal functional is unknow. Problems arise not only from the interaction term $\hat{W}$, but also from the kinetic part of the functional. A possible strategy is to use a model system of non-interacting electrons, as pointed out by Kohn and Sham [38].
The central assertion of the Kohn-Sham scheme is [3]:

[3]The subscript s indicate the non-interacting system related quantities

For each interacting system ($\hat{W} \neq 0$ in eq. 2.3), there must be a local mono-electronic potential v_s, such that the exact density of the interacting system is equal to the density of the non-interacting system with external potential v_s.

In the Kohn–Sham formulation, the density is expressed in terms of N orthonormal orbitals,

$$\rho(\mathbf{r}) = \sum_i |\phi_i(\mathbf{r})|^2 \tag{2.20}$$

the universal functional is

$$\mathcal{F}_{KS}[\rho] = -\frac{1}{2}\sum_i \langle\phi_i|\nabla^2|\phi_i\rangle + E_H[\rho] + E_{XC}[\rho] \tag{2.21}$$

where the Hartree (or classical Coulomb) energy is given by,

$$E_H[\rho] = \frac{1}{2}\int\int \frac{\rho(\mathbf{r}_1)\rho(\mathbf{r}_2)}{\mathbf{r}_{12}} d\mathbf{r}_1 d\mathbf{r}_2 \tag{2.22}$$

Here $E_{XC}[\rho]$ is the exchange-correlation (XC) energy functional. It takes into account the electron-electron interactions and the correction to the kinetic energy term of the interacting system. Minimizing the energy gives the Kohn–Sham equation

$$\hat{f}_i^s[\rho]\phi_i(\mathbf{r}) = \varepsilon_i\phi_i(\mathbf{r}) \tag{2.23}$$

where the single-particle Kohn–Sham hamiltonian is

$$\hat{f}_i^s = -\frac{1}{2}\nabla^2 + v_s(\mathbf{r}) + v_H[\rho](\mathbf{r}) + v_{XC}[\rho](\mathbf{r}) \tag{2.24}$$

$$\hat{F}^{KS} = \sum_i \hat{f}_i^s \tag{2.25}$$

Here the Hartree potential is

$$v_H[\rho](\mathbf{r}) = \frac{\delta E_H[\rho](\mathbf{r})}{\delta\rho(\mathbf{r}_1)} = \int \frac{\rho(\mathbf{r}_2)}{\mathbf{r}_{12}} d\mathbf{r}_2 \tag{2.26}$$

and the XC potential is

$$v_{XC}[\rho](\mathbf{r}) = \frac{\delta E_{XC}[\rho](\mathbf{r})}{\delta\rho(\mathbf{r}_1)} \tag{2.27}$$

Since no exact form of the XC functional is known, this functional is approximated in practice. Once a XC approximation is chosen, the equations are to be solved self-consistently. What differentiates between the various approaches to the DFT method is the choice of the exchange-correlation energy functional. The theory provides no restrictions on the choice, therefore, various approximations have been proposed. The principal are the Local Density Approximation (LDA), the Generalized Gradient Approximation (GGA), the global hybrid (GH) functionals and a new generation of hybrid functionals, denoted as range-separeted (RSH) or long-range corrected (LRC).

LDA

Local-density approximations (LDA)[37],[14] are a class of approximations to the XC energy functional that depend solely upon the value of the electronic density at each point in space. Many approaches can yield local approximations to the XC energy. However, overwhelmingly successful local approximations are those that have been derived from the homogeneous electron gas (HEG) model. In this regard, LDA is generally synonymous with functionals based on the HEG approximation applied to realistic systems (molecules and solids).

In general, for a spin-unpolarized system, a local-density approximation for the exchange-correlation energy is written as

$$E_{xc}^{\mathrm{LDA}}[\rho] = \int \rho(\mathbf{r})\epsilon_{xc}(\rho)\ \mathrm{d}\mathbf{r}\ , \tag{2.28}$$

the exchange-correlation energy density ϵ_{xc}, is a function of the density alone. Usually it is assumed, in somewhat arbitrary way, to be able to separate the components of the exchange and correlation functional, which is therefore written as a sum :

$$E_{xc}[\rho] = E_x[\rho] + E_c[\rho] \tag{2.29}$$

so that separate expressions for E_x and E_c are sought. The exchange term takes a simple analytic form for the HEG. Only limiting expressions for the correlation density are known exactly, leading to numerous different approximations for E_c. The exchange-energy density of a HEG is known analytically. The LDA for exchange uses the following expression, due to Dirac [39],

$$E_x^{\mathrm{LDA}}[\rho] = -\frac{3}{4}\left(\frac{3}{\pi}\right)^{1/3}\int \rho(\mathbf{r})^{4/3}\ \mathrm{d}\mathbf{r} \tag{2.30}$$

This expression is obtained under the approximation that the exchange-energy in a system where the density in not homogeneous, is obtained by applying the HEG results pointwise. Analytic expressions for the correlation energy of the HEG are not known except in the high- and low-density limits corresponding to infinitely-weak and infinitely-strong correlation. For a HEG with density ρ, the high-density limit of the correlation energy density is [23]:

$$\epsilon_c = A\ln(r_s) + B + r_s(C\ln(r_s) + D) \tag{2.31}$$

and the low limit

$$\epsilon_c = \frac{1}{2}\left(\frac{g_0}{r_s} + \frac{g_1}{r_s^{3/2}} + \dots\right) \tag{2.32}$$

where the Wigner-Seitz radius is related to the density as

$$\frac{4}{3}\pi r_s^3 = \frac{1}{\rho}. \tag{2.33}$$

Accurate quantum Monte Carlo simulations for the energy of the HEG have been performed for several intermediate values of the density, in turn providing accurate values of the correlation energy density [40]. The most popular LDA's to the correlation energy density interpolate these accurate values obtained from simulation while reproducing the exactly known limiting behavior. Various approaches, using different analytic forms for c, have generated several LDA's for the correlation functional, including

- Vosko-Wilk-Nusair (VWN) [41]
- Perdew-Zunger (PZ81) [42]
- Cole-Perdew (CP) [43]
- Perdew-Wang (PW92) [44]

The exchange-correlation potential corresponding to the exchange-correlation energy for a local density approximation is given by

$$v_{xc}^{\mathrm{LDA}}(\mathbf{r}) = \frac{\delta E^{\mathrm{LDA}}}{\delta\rho(\mathbf{r})} = \epsilon_{xc}(\rho(\mathbf{r})) + \rho(\mathbf{r})\frac{\partial\epsilon_{xc}(\rho(\mathbf{r}))}{\partial\rho(\mathbf{r})} \tag{2.34}$$

In finite systems, the LDA potential decays asymptotically with an exponential form. This is in error: the true exchange-correlation potential decays much slower in a Coulombic manner $(-1/2r)$ [42],[37]. The artificially rapid decay manifests itself in the number of Kohn-Sham orbitals the potential can bind (that is, how many orbitals have energy less than zero). The LDA potential can not support a Rydberg series and underbond states are too high in energy. This results in the HOMO energy being too high, so that any predictions for the ionization potential based on Koopman's theorem are poor. Further, the LDA provides a poor description of electron-rich species such as anions where it is often unable to bind an additional electron, erroneously predicting species to be unstable.

LDA functionals are important in the construction of more sophisticated approximations to the exchange-correlation energy, such as generalized gradient approximations or hybrid functionals, as a desirable property of any approximate exchange-correlation functional is that it reproduce the exact results of the HEG for non-varying densities. As such, LDA's are often an explicit component of such functionals.

GGA

The LDA functional is exact for the homogeneous electron gas, but in general tends to underestimate by around 10% the exchange energy of atoms. For example, for the Ne atom the fair value of E_x is -329 eV while from the Dirac functional a value of -298 eV is obtained with a considerable error (about 4-5 times the binding energy of H_2 molecule).
Among the many faults, it also does not give rise to the right asymptotic behavior. In the 80's efforts to correct the Dirac functional have been proposed, moving from local to nonlocal functional, or to functionals where the energy density depends on the density of its gradient. These methods are also called by the name of the Generalized Gradient Approximation (GGA) [45],[46],[37]. GGA is an improvement quite natural since for the uniform density gradient is zero, while it is not for the usual atomic and molecular density. In general, GGA functionals are of the type:

$$E_{xc}[\rho, \nabla\rho] = \int \rho(\mathbf{r}) f_x(\rho, \nabla\rho, \mathbf{r}) d\mathbf{r} \tag{2.35}$$

One of the most accurate result for exchange part was obtained by Becke [46] on the basis of some reasoning aimed at correcting the bad asymptotic behavior of the energy density of the Dirac exchange functional:

$$E_x^B[\rho, \nabla\rho] = E_x^{LDA}[\rho] + \int \rho(\mathbf{r})\epsilon_x^B(\rho, \nabla\rho, \mathbf{r})d\mathbf{r} \tag{2.36}$$

where

$$\epsilon_x^B(\rho, \nabla\rho, \mathbf{r}) = -\beta\rho^{1/3}\frac{X^2}{1 + 6\beta \sinh^{-1} X} \tag{2.37}$$

with

$$X = \frac{|\nabla\rho|}{\rho^{4/3}} \qquad \text{and} \qquad \beta = 0.0042 \tag{2.38}$$

β was empirically determined to accurately to reproduce the Hartree-Fock exchange energy of noble gases. ϵ_x^B has the correct asymptotic behavior for the exact density. However, it should be noted that the corrected exchange potential:

$$v_x(r) = \frac{\delta E_x}{\delta\rho} = \epsilon_x + \rho\frac{\partial\epsilon_x}{\partial\rho} - \nabla \cdot \frac{\partial E_x}{\partial(\nabla\rho)} \tag{2.39}$$

has an asymptotic behavior that is identical to the exchange energy density. It can be shown that the potential corresponding to the energy density of Becke decays as $-1/r^2$ instead of $-1/r$.
The merit of this functional was very large: from 1988 onwards, the KS-DFT method has become a widely used tool in many fields of theoretical chemistry, replacing the Hartree-Fock method in computational chemistry.
A positive feature of this functional is that the use of $\nabla\rho$ introduced a proper treatment of the shell structure of atoms: this is the main reason for its success in representing the energy exchange. Among the defects it has however to be mentioned that the exchange of Becke (B88) reduces but does not completely eliminate the error of self-interaction. This will be discussed in a next section.
Concerning the correlation part, one of the most used is the Lee, Yang and Parr (LYP) correlation functional [47], based on the expression of Colle and Salvetti. The novelty of this functional is that it was derived from a correlated wave function for the He atom and not from the HEG. Colle and Salvetti [48] approximate the correlation energy formula for the Helium atom in terms of the second order HF density matrix. Lee, Yang and Parr turned this into a functional of the density, gradient and Laplacian. Miehlich, Savin, Stoll and Press [49], later eliminated the Laplacian terms using integration by parts. For closed shell systems the functional is

$$\begin{aligned} E_c[\rho, \nabla\rho] \;=\; & -a \int \tfrac{\rho}{1+d\rho^{-1/3}} \\ & -ab \int \omega\rho^2 \left[C_F\rho^{8/3} + |\nabla\rho|^2 \left(\tfrac{5}{12} - \tfrac{7\delta}{72}\right) - \tfrac{11}{24}\rho^2\nabla\rho|^2\right] dr \end{aligned} \tag{2.40}$$

$$\omega = \frac{exp(-c\rho^{-1/3})}{1+d\rho^{-1/3}}\rho^{-11/3} \qquad \delta = c\rho^{-1/3} + \frac{d\rho^{-1/3}}{1+d\rho^{-1/3}} \tag{2.41}$$

$$a = 0.04918 \qquad b = 0.132 \qquad c = 0.2533 \qquad d = 0.349 \tag{2.42}$$

Hybrid functionals

Two distinct philosophies have emerged in the construction of modern exchange-correlation functionals. Perdew supports the idea that functionals should be derived non-empirically using rigorous quantum-mechanical principles and exact conditions, however Becke advocates the semi-empirical approach whereby a general functional form containing free parameters is proposed, and the parameters are subsequently fitted to minimise the error in exact physical properties. The semi-empirical concept is extensively used and developed within the quantum chemistry community where there is a wealth of known atomic and molecular data that can be used to fit functionals.
Hybrid functionals incorporate a portion of exact exchange from Hartree-Fock theory with exchange and correlation from other sources (ab initio, such as LDA and GGA, or empirical). The exact exchange energy functional is expressed in terms of the Kohn-Sham orbitals rather than the density, therefore sometimes it is indicated as an implicit density functional.
The hybrid approach to approximate the XC density functional was introduced by Axel Becke in 1993 [50], on the basis of the adiabatic connection formula (ACF), which connects the noninteracting KS reference system to the fully interacting real system, through a continuum of partially interacting real systems, all sharing a common density.

Hybridization with Hartree-Fock exchange provides a simple scheme for improving many molecular properties, such as atomization energies, bond lengths and vibration frequencies, which tend to be poorly described with simple *ab initio* functionals of the LDA or GGA type.
A hybrid exchange-correlation functional is usually constructed as a linear combination of the Hartree-Fock exact exchange functional (E_x^{HF}) and any

number of exchange and correlation explicit density functionals. The parameters determining the weight of each individual functional are typically specified by fitting the functional's predictions to experimental or accurately calculated thermochemical data.
Standardised sets of experimental data, collated by Pople and co-workers and known as the Gaussian set [4], were especially suited for the purposes of constructing semi-empirical functionals. For example, the G2 set consists of highly accurate experimental thermochemical data - atomisation energies, ionisation potentials and electron and proton affinities - of a range of atomic and molecular systems, drawn from the first two rows of the periodic table.
As an example, the popular B3LYP (Becke, three-parameter, Lee-Yang-Parr) [46],[47],[50] exchange-correlation functional takes the form:

$$E_{xc}^{\mathrm{B3LYP}} = E_{xc}^{\mathrm{LDA}} + a_0(E_x^{\mathrm{HF}} - E_x^{\mathrm{LDA}}) + a_x(E_x^{\mathrm{GGA}} - E_x^{\mathrm{LDA}}) + a_c(E_c^{\mathrm{GGA}} - E_c^{\mathrm{LDA}}) \tag{2.43}$$

where $a_0 = 0.20$, $a_x = 0.72$, and $a_c = 0.81$ are the three empirical parameters determined by fitting the predicted values to a set of atomization energies, ionization potentials, proton affinities, and total atomic energies;[5]
E_x^{GGA} and E_c^{GGA} are generalized gradient approximations: the Becke 88 exchange functional[6] and the correlation functional of Lee, Yang and Parr,[7] and E_c^{LDA} is the VWN local-density approximation to the correlation functional. Hybrid functionals successfully demonstrate the need to incorporate fully non-local information in order to deliver greater accuracy. In a different phylosophy, a parameter free hybrid functional is the PBE0 of Adamo and Barone [54]. Perdew, Burke and Ernzerhof [45] have introduced a GGA functional in which all the parameters, other than those in its local spin density (LSD) component, are fundamental constants. This is obtained using the Perdew–Wang PW92 [44] correlation functional and the exchange contribution:

$$E_x^{PBE}[\rho, \nabla\rho] = \frac{bX^2}{1 + aX^2} \tag{2.44}$$

where X is defined in eq.(2.38) and $b = 0.00336$, $a = 0.00449$. In the ACF framework the XC functional is written as only one parameter hybrid:

$$E_{XC}[\rho, \nabla\rho] = E_{XC}^{PBE}[\rho, \nabla\rho] + a\left(E_{XC}^{HF} - E_{XC}^{PBE}[\rho, \nabla\rho]\right) \tag{2.45}$$

[4] During the years the number of data collected increases and different set exist, indicated as G1, G2 and G3 [51],[52],[53]

However on the basis of what Perdew and co-workers have shown, the optimum value of the a coefficient can be fixed a priori taking into account that fourth-order perturbation theory is sufficient to get accurate numerical results for molecular systems. Therefore:

$$E_{XC}^{PBE0}[\rho,\nabla\rho] = E_{XC}^{PBE}[\rho,\nabla\rho] + \frac{1}{4}\left(E_{XC}^{HF} - E_{XC}^{PBE}[\rho,\nabla\rho]\right) \tag{2.46}$$

Some problems in DFT-KS

The use of approximate XC functionals gives rise to some problems in the description of the molecular systems. One of these is the asymptotic behavior of the XC potential [46], as we already mentioned in the case of LDA and GGA. Since hybrid functionals contain only a fixed percentage of HF exchange (that shows the correct asymptotic behavior), the correction done is only proportional to this amount. Another well know problem, linked to the asymptotic behavior problem, is the so-called *Self-Interaction* of the density [42]. Approaches that attempt to correct this problem are know as Self-Interaction Correction (SIC). Let us illustrate the problem in few words.
One of the major difference between a quantum electron density and charge distribution is in the classical self-interaction. In fact, an electron interacts with all others but not with itself therefore, for a density of N particles, the right number of interactions is the number of electron pairs without repetition, and scale as N^2, or more precisely $N(N-1)/2$. The number of self-interactions will instead be proportional to N and, for a macroscopic density (eg. $N = 10^{20}$), the fraction of the number of self-interactions with respect to the number of interactions is largely negligible. However for a molecular density this issue is relevant.
In the HF method, which approximates the wave function with a single Slater determinant, but it maintains the proper antisymmetry of the wave function, this requirement is fulfilled in a natural way. In fact, in the energy expression of inter-electronic repulsion

$$E_{HF}^{(2)} = \frac{1}{2}\sum_{i=1}^{N}\sum_{j=1}^{N}\left[\langle ij|ij\rangle - \langle ij|ji\rangle\right] \qquad (h + \sum_{j=1}^{N}[J_j - K_j])\phi_i = \varepsilon_i\phi_i \tag{2.47}$$

it is clear that for $i = j$ (interaction of two electrons in the same spin-orbital or an electron with itself) the Coulomb term is canceled by the terms of exchange.

In the Hartree method the wave function is a product of spin orbitals for which the antisymmetry of the wave function is not covered and the cancellation does not occur in the equations and the self interaction term is eliminated ad-hoc:

$$E_H^{(2)} = \frac{1}{2}\sum_{i=1}^{N}\sum_{j\neq i}^{N}\langle ij|ij\rangle \qquad (h + \sum_{j=1,j\neq i}^{N} J_j)\phi_i = \varepsilon_i\phi_i \tag{2.48}$$

with the result that there is a specific equation for each spin orbital. The correct number of interactions turns out to be $N(N-1)/2$, or all pairs of electrons without repetition.
The electrostatic energy in the DFT method includes the Coulomb term

$$E_H[\rho] = J[\rho] = \frac{1}{2}\int dr_1 \int dr_2 \frac{\rho(r_1)\rho(r_2)}{r_{12}} = \frac{1}{2}\sum_{i=1,j=1}^{N}\langle ij|ij\rangle \tag{2.49}$$

that is the same as the Hartree without the ad-hoc correction, and includes $N^2/2$ total interactions and $N/2 = (N^2 - N(N-1))/2$ spurious interactions. This defect is not unexpected given that we have defined the functional $E_H[\rho]$ as the classic inter-electronic energy. Obviously the functional E_{xc} in its exact form will have to cancel the spurious terms contained in $J[\rho]$. Unfortunately, the exact exchange-correlation energy functional is not known and also with most of the modern functionals is possible to only get a partial cancellation of the spurious terms, so the final energy is also affected by problems of self-interaction. This not precise scaling of the number of interactions with the number of electrons becomes particularly critical in the case, for example, of calculations of ionization energies, where the final result comes from the energy differences between neutral and ionic systems, thus having a different number of electrons. In this and other cases we can not expect effective cancellation of the error of the SI. This issue is also reflected in the behavior of the asymptotic effective potential v_{xc} in the equations of KS.
There are several approaches to correct this problem (see for example references in [37]). The best known is certainly that of Perdew and Zunger (PZ) [42], which has the disadvantage of being orbital-dependent, so we obtain N different KS equations. Other methods make use of a medium approach, based on an approach similar to that of Fermi and Amaldi [55], in which the density is scaled by $N - 1/N$, such as in the ADSIC method [56],[57].

The Long Range Correction Scheme

The local nature of approximate XC functionals in DFT causes serious problems in practical calculations of various molecular properties. Introducing a

fixed amount of the Hartree–Fock (HF) exchange contribution gives in many cases partial solutions of these problems. Nevertheless, some molecular properties such as the longitudinal polarizabilities of all-trans polyenes with increasing number of ethylene units cannot be described even qualitatively by such conventional hybrid functionals. The poor performance of the pure and conventional hybrid functionals for these quantities can be attributed to the (partial) lack of the long-range exchange interaction. In these years, a powerful prescription has been suggested, namely, the so-called long-range correction (LRC) [58] to exchange functionals. The basic idea of LRC is to simply separate the electron– electron Coulomb interaction into short-range (SR) and long-range (LR) parts [59],

$$\frac{1}{r_{12}} = \frac{1 - w(r_{12})}{r_{12}} + \frac{w(r_{12})}{r_{12}} \tag{2.50}$$

by a separation-function $w(r_{12})$, and use the SR part to compute the density functional exchange contribution and the LR part in the form of the HF exchange energy. The functionals obtained in this way, the range-separated hybrid functionals (RSH), have shown dramaticaly improved performance in the problematic cases mentioned earlier. The complementary error function $erfc(\mu r_{12})$ has been employed almost exclusively as $w(r_{12})$ with Gaussian-type basis functions (GTF) for the ease of the computation of integrals over the modified Coulomb operator. Several extensions of LRC (eq. 2.50) have been suggested for further improvements of accuracy [60],[61],[62].
Yanai et al. proposed [63] a general form of the range-separation named Coulomb-attenuated method (CAM),

$$\frac{1}{r_{12}} = \frac{1 - (\alpha + \beta)erf(\mu r_{12})}{r_{12}} + \frac{(\alpha + \beta)erf(\mu r_{12})}{r_{12}} \tag{2.51}$$

CAM indroduces a global mixing of the HF exchange with a fixed ratio, which is determined by α, as well as the range-separated one. In addition, $\alpha + \beta$ indicates the ratio of the HF exchange in $r = \infty$, which is fixed at 1.0 in the original LRC scheme eq (2.50). The introduction of the parameters α and β bridges the pure ($\alpha = \beta = 0$), conventional hybrid ($\alpha = 0$ and $\beta = 0$), and range-separated hybrid ($\beta = 0$) functionals seamlessly.
The performance of the proposed CAM-B3LYP functional with $\alpha = 0.19$, $\beta = 0.46$, and $\mu = 0.33$ has been assessed by several authors [64],[65],[66], [67],[68]. In this Thesis we extensively use the CAM-B3LYP functional to calculate excited state energies and properties in the LR-KS TD-DFT scheme.

2.3 The Time Dependent DFT

The traditional KS-DFT is limited to time independent systems, that is, ground states, and if one wants to establish an analogous time-dependent theory, time-dependent versions of the first and second HK theorems must be formulated and a time-dependent KS equation must be derived. In this section, we present the Runge-Gross theorem [15], which is a time-dependent analogue to HK first theorem and the role of the action integral in a time-dependent variational principle is analysed.

The Runge-Gross theorem can be seen as the time dependent analogue of the first Hohenberg-Kohn theorem and constitutes the cornerstone of the formal foundation of the time-dependent Kohn-Sham formalism.

Theorem 3 (of Runge and Gross) *The exact time-dependent electron density, $\rho(r,t)$, determines the time-dependent external potential, $V(r,t)$, up to a spatially constant, time-dependent function $C(t)$ and thus the time-dependent wave function, $\Psi(r,t)$, up to a time dependent phase factor.*

The wave function is thus a functional of the electron density

$$\Psi(r,t) = \Psi[\rho(t)](t)e^{-i\alpha t} \tag{2.52}$$

with $(d/dt)\alpha(t) = C(t)$. Also in this case, $V(t)$ is a time-dependent external potential and is given as a sum of one-particle potentials

$$V(t) = \sum_{i}^{N} v(r_i, t) \tag{2.53}$$

To prove the Runge-Gross theorem, it must be demonstrated that two densities $\rho_A(r,t)$ and $\rho_B(r,t)$ evolving from a common initial state Ψ_0 under the influence of two different potentials $v^A(r,t)$ and $v^B(r,t)$ are always different if the two potentials differ by more than a purely time-dependent function, that is

$$v^A(r,t) \neq v^B(r,t) + C(t) \tag{2.54}$$

An assumption to be made is that the potentials can be expanded in a Taylor series in time around t_0 The proof proceeds in two steps: First it is shown that the current densities, $j^A(r,t)$ and $j^B(r,t)$, corresponding to $v^A(r,t)$ and $v^B(r,t)$ are always different, and in a second step, it is derived that different current densities require different electron densities. Consequently, for different time-dependent external potentials at $t \neq t_0$, one obtains different time-dependent

electron densities infinitesimally later than t_0. With this, the one-to-one mapping between time-dependent densities and time-dependent potentials is established, and thus, the potential and the wave function are functionals of the density [5].
Furthermore, the expectation value of any quantum mechanical operator is a unique functional of the density because the phase factor in the wave function cancels out.
Strictly speaking, the expectation value implicitly depends also on the initial state, Ψ_0, that is, it is a functional of $\rho(r,t)$ and Ψ_0. For most cases, however, when Ψ_0 is a nondegenerate ground state, $O[\rho](t)$ is a functional of the density alone, because Ψ_0 is a unique functional of its density $\rho_0(r)$ by virtue of the traditional first Hohenberg-Kohn theorem.
The one-to-one mapping between time-dependent potentials and time-dependent functionals represents the first step in the development of a time dependent many-body theory using the density as a fundamental quantity. A second requirement is the existence of a variational principle in analogy to the time-independent case, in which it is given by the above-described second Hohenberg-Kohn theorem [37]. In general, if the time-dependent wave function $\Psi(r,t)$ is a solution of the time-dependent Schrödinger equation with the initial condition

$$\Psi(r,t_0) = \Psi_0(t) \tag{2.55}$$

then the wave function corresponds to a stationary point of the quantum mechanical action integral.

$$A = \int_{t_0}^{t_1} dt \langle \Psi(r,t) | i\frac{\partial}{\partial t} - \hat{H}(r,t) | \Psi(r,t) \rangle \tag{2.56}$$

which is a functional of $\rho(r,t)$ owing to the Runge-Gross theorem, that is,

$$A[\rho] = \int_{t_0}^{t_1} dt \langle \Psi[\rho](r,t) | i\frac{\partial}{\partial t} - \hat{H}(r,t) | \Psi[\rho](r,t) \rangle \tag{2.57}$$

Consequently, the exact electron density $\rho(r,t)$ can be obtained from the Euler

[5] Few years ago, van Leeuwen presented a generalization of the Runge-Gross theorem and proved that a time dependent density $\rho(r,t)$ obtained from a many-particle system can under mild restriction on the initial state always be reproduced by an external potential in a many-particle system with different two-particle interaction.
For two states with equivalent initial state and the same two-particle interaction, van Leeuwen's theorem reduces to the Runge-Gross theorem.

equation

$$\frac{\partial A[\rho]}{\partial \rho(r,t)} = 0 \tag{2.58}$$

when appropriate boundary conditions are applied. Furthermore, the action integral can be split into two parts, one that is universal (for a given number of electrons) and the other dependent on the applied potential $v(r,t) = v_{el-nuc}(r) + v_{appl}(r,t)$

$$A[\rho] = B[\rho] + \int_{t_0}^{t_1} dt \int d^3r \rho(r,t) v(r,t) \tag{2.59}$$

The universal functional $B[\rho]$ is independent of the potential $v(r,t)$ and is given as

$$B[\rho] = \int_{t_0}^{t_1} dt \langle \Psi(r,t) | i\frac{\partial}{\partial t} - \hat{T}(r) - \hat{V}_{e-e}(r) | \Psi(r,t) \rangle \tag{2.60}$$

In summary, the variation of the action integral with respect to the density according to eq. (2.58) is a prescription of how the exact density can be obtained.

2.4 Linear Response KS approach to TD-DFT

The stationary action principle can be applied to derive a time-dependent Kohn-Sham equation in analogy to the time-independent counterpart. The time-dependent Kohn-Sham equations [16] can be conveniently expressed in matrix notation in a basis of, say, M time-independent single-particle wave functions $\{\chi_i(r)\}$ such that

$$\varphi_p(r,t) = \sum_j c_{pj}(t) \chi_j(r) \tag{2.61}$$

Then, the time-dependent KS equation reads

$$i\frac{\partial}{\partial t}\mathbf{C} = \mathbf{F}^{KS}\mathbf{C} \tag{2.62}$$

Here, the i-th column of the matrix $\mathbf{C}$ contains the time-dependent expan-

sion coefficients of $\varphi_i(r,t)$ and $\mathbf{F}^{KS}$ is the matrix representation of the time-dependent Kohn-Sham operator [6] in the given basis.

Multiplication of eq (2.62) from the right with $\mathbf{C}^\dagger$ and then subtraction from the resultant equation of its Hermitian transpose leads to the Dirac form of the time dependent Kohn-Sham equation in density matrix form. This equation reads[7]

$$\sum_q \left(F_{pq}P_{qr} - P_{pq}F_{qr}\right) = i\frac{\partial}{\partial t}P_{pr} \tag{2.63}$$

in which the density matrix P_{pr} is in general related to the electron density via

$$\rho(r,t) = \sum_{p,r}^{N}\sum_{i,j}^{M} c_{pj}(t)c^*_{ri}(t)\chi_j(r)\chi^*_i(r) = \sum_{i,j}^{M}\chi_j(r)\chi^*_i(r)P_{ij} \tag{2.64}$$

To obtain excitation energies and oscillator strengths employing the time-dependent KS approach, two different strategies can be followed. One possibility is to propagate the time-dependent KS wave function in time, which is referred to as "real-time TD-DFT".
The other, most used in quantum chemistry and also in this Thesis, is the linear response approach: using a density matrix formalism, it is shown how the excitation energies are obtained from the linear time-dependent response of the time-independent ground-state electron density to a time-dependent external electric field [16].
Before the time-dependent electric field is applied, the system is assumed to be in its electronic ground state, which is determined by the standard time-independent Kohn-Sham equation, which in the density matrix formulation is:

$$\sum_q \left(F^{(0)}_{pq}P^{(0)}_{qr} - P^{(0)}_{pq}F^{(0)}_{qr}\right) = 0 \tag{2.65}$$

with the idempotency condition

$$\sum_q P^{(0)}_{pq}P^{(0)}_{qr} = P^{(0)}_{pr} \tag{2.66}$$

$F^{(0)}_{pq}$ and $P^{(0)}_{pq}$ correspond to the Kohn-Sham Hamiltonian and density matrix of the unperturbed ground state, respectively. The elements of the time independent Kohn-Sham Hamiltonian matrix are given as [24]

[6] The time-independent counterpart is given in eq. 2.25
[7] We drop out the superscript KS

$$F_{pq}^{(0)} = \int d^3r \varphi_p^*(r) \left\{ -\frac{1}{2}\nabla^2 - \sum_{K=1}^{M} \frac{Z_K}{|r - R_K|} + \int d^3r' \frac{\rho(r')}{|r - r'|} + \frac{\delta E_{xc}}{\delta \rho(r)} \right\} \varphi_q(r) \tag{2.67}$$

In the basis of the orthonormal unperturbed single-particle orbitals of the ground state, these matrices are simply given as [8]

$$F_{pq}^{(0)} = \delta_{pq} \varepsilon_p \tag{2.68}$$

and

$$\begin{aligned} P_{ij}^{(0)} &= \delta_{ij} \\ P_{ai}^{(0)} = P_{ia}^{(0)} &= P_{ab}^{(0)} = 0 \end{aligned} \tag{2.69}$$

Now, an oscillatory time-dependent external field is applied, and the first-order (linear) response to this perturbation is analysed. In general perturbation theory, the wave function or in this case the density matrix is assumed to be the sum of the unperturbed ground state and its first-order time-dependent change,

$$P_{pq} = P_{pq}^{(0)} + P_{pq}^{(1)} \tag{2.70}$$

The same holds for the time-dependent Kohn- Sham Hamiltonian, which to first order is given as the sum of the ground-state KS Hamiltonian and the first-order change

$$F_{pq} = F_{pq}^{(0)} + F_{pq}^{(1)} \tag{2.71}$$

Substituting eqs (2.70) and (2.71) into the time-dependent Kohn-Sham eq. (2.63) and collecting all terms of first order yield

$$\sum_q \left(F_{pq}^{(0)} P_{qr}^{(1)} - P_{pq}^{(1)} F_{qr}^{(0)} + F_{pq}^{(1)} P_{qr}^{(0)} - P_{pq}^{(0)} F_{qr}^{(1)} \right) = i \frac{\partial}{\partial t} P_{pr}^{(1)} \tag{2.72}$$

[8] Again, we follow the convention that indices i, j, etc. correspond to occupied orbitals, a, b, etc. correspond to virtual orbitals and p, q, r, etc. refer to general orbitals.

The first-order change of the Kohn-Sham Hamiltonian consists of two terms. The first contribution corresponds to the applied perturbation, the time dependent electric field itself, and it has been shown that it is sufficient to consider only a single Fourier component of the perturbation, which is given in matrix notation as

$$g_{pq} = \frac{1}{2}[f_{pq}e^{-i\omega t} + f^*_{qp}e^{i\omega t}] \tag{2.73}$$

In this equation, the matrix f_{pq} is a one-electron operator and describes the details of the applied perturbation. Furthermore, the two-electron part of the Kohn-Sham Hamiltonian changes according to changes in the density matrix. The changes in the KS Hamiltonian due to the change of the density are given to first order as

$$\Delta F^{(0)}_{pq} = \sum_{st} \frac{\partial F^{(0)}_{pq}}{\partial P_{st}} P^{(1)}_{st} \tag{2.74}$$

such that the first-order change in the KS Hamiltonian is altogether given as

$$F^{(1)}_{pq} = g_{pq} + \Delta F^{(0)}_{pq} \tag{2.75}$$

The time-dependent change of the density matrix induced by the perturbation of the KS Hamiltonian, this is to first order given as

$$P^{(1)}_{pq} = \frac{1}{2}[X_{pq}e^{-i\omega t} + Y^*_{qp}e^{i\omega t}] \tag{2.76}$$

where X_{pq} and Y_{qp} represent perturbation densities.
Inserting the last four equations into eq. (2.72) and collecting the terms that are multiplied by $e^{-i\omega t}$ yield the following expression

$$\sum_q \left[F^{(0)}_{pq}X_{qr} - X_{pq}F^{(0)}_{qr} + \left(f_{pq} + \sum_{st} \frac{\partial F^{(0)}_{pq}}{\partial P_{st}} X_{st} \right) P^{(0)}_{qr} - P^{(0)}_{pq} \left(f_{qr} + \sum_{st} \frac{\partial F^{(0)}_{qr}}{\partial P_{st}} X_{st} \right) \right] = \omega X_{pr} \tag{2.77}$$

The terms multiplied by $e^{i\omega t}$ lead to the complex conjugate of the above equation. The idempotency condition eq.(2.66) gives an expression for the first

order change of the density matrix of the form

$$\sum_q \left[P^{(0)}_{pq}P^{(1)}_{qr} + P^{(1)}_{pq}P^{(0)}_{qr}\right] = P^{(0)}_{pq} \tag{2.78}$$

which restricts the form of the matrix $\mathbf{X}$ in eq. (2.77) such that

- occupied-occupied and virtual-virtual blocks (X_{ii} and Y_{aa}) are zero,
- only the occupied-virtual and virtual-occupied blocks (X_{ia} and Y_{ai}), respectively, contribute and are taken into account.

Remembering the diagonal nature of the unperturbed KS Hamiltonian and density matrixes, one obtains the following pair of equations:

$$F^{(0)}_{aa}X_{ai} - X_{ai}F^{(0)}_{ii} + \left(f_{ai} + \sum_{bj}\left[\frac{\partial F^{(0)}_{ai}}{\partial P_{bj}}X_{bj} + \frac{\partial F^{(0)}_{ia}}{\partial P_{jb}}Y_{bj}\right]\right)P^{(0)}_{ii} = \omega X_{ai} \tag{2.79}$$

$$F^{(0)}_{ii}Y_{ai} - Y_{ai}F^{(0)}_{aa} - \left(f_{ia} + \sum_{bj}\left[\frac{\partial F^{(0)}_{ia}}{\partial P_{bj}}X_{bj} + \frac{\partial F^{(0)}_{ai}}{\partial P_{jb}}Y_{bj}\right]\right)P^{(0)}_{ii} = \omega Y_{ai} \tag{2.80}$$

In the zero-frequency limit ($f_{ai} = f_{ia} = 0$), that is, under the assumption that the electronic transitions occur for an infinitesimal perturbation, one obtains a non-Hermitian eigenvalue equation, the LR-KS equation,

$$\begin{bmatrix} \mathbf{A} & \mathbf{B} \\ \mathbf{B}^* & \mathbf{A}^* \end{bmatrix}\begin{bmatrix} \mathbf{X} \\ \mathbf{Y} \end{bmatrix} = \omega \begin{bmatrix} \mathbf{1} & \mathbf{0} \\ \mathbf{0} & -\mathbf{1} \end{bmatrix}\begin{bmatrix} \mathbf{X} \\ \mathbf{Y} \end{bmatrix} \tag{2.81}$$

the structure of which is equivalent to the Time Dependent Hartree-Fock (TD-HF) [33].
Here, the elements of the matrices A and B are given as

$$\begin{aligned} A_{ia\sigma,jb\tau} &= \delta_{ij}\delta_{ab}\delta_{\sigma\tau}(\varepsilon_a - \varepsilon_b) + \langle i_\sigma j_\tau | a_\sigma b_\tau\rangle - C_{HF}\delta_{\sigma\tau}\langle i_\sigma a_\sigma | j_\tau b_\tau\rangle \\ &\quad + (1 - C_{HF})\langle i_\sigma j_\tau | f_{xc} | a_\sigma b_\tau\rangle \end{aligned} \tag{2.82}$$

$$\begin{aligned} B_{ia\sigma,jb\tau} &= \langle i_\sigma b_\tau | a_\sigma j_\tau\rangle - C_{HF}\delta_{\sigma\tau}\langle i_\sigma a_\sigma | b_\tau j_\tau\rangle \\ &\quad + (1 - C_{HF})\langle i_\sigma b_\tau | f_{xc} | a_\sigma j_\tau\rangle \end{aligned} \tag{2.83}$$

Equations (2.81) - (2.83) represent the TD-DFT formalism, which is solved

to obtain excitation energies ω and transition vectors $|\mathbf{X}+\mathbf{Y}\rangle$ when the unperturbed KS Hamiltonian , from which the response is derived, contains a so-called pure DFT XC potential or also parts of Hartree-Fock exchange. Indeed, the elements of the matrices $\mathbf{A}$ and $\mathbf{B}$ contain also the response of the Hartree-Fock exchange potential, as well as the one of the chosen XC potential at a rate determined by the factor C_{HF} determined in the hybrid XC functional. It becomes apparent that the equations contain TD-HF and pure (i.e. no hybrid functional used) TD-DFT as limiting cases if $C_{HF}=1$ or $C_{HF}=0$, respectively.

In the so-called adiabatic local density approximation (ALDA) [16] the originally non-local (in time) time-dependent xc kernel is replaced with a time-independent local one based on the assumption that the density varies only slowly with time. This approximation allows the use of a standard local ground-state xc potential in the TD-DFT framework. In the ALDA, the response of the xc potential corresponds to the second functional derivative of the exchange-correlation energy, which is also called the xc kernel, and is given as

$$\langle i_\sigma j_\tau | f_{xc} | a_\sigma b_\tau \rangle = \int d^3r d^3r' \varphi_i^*(r)\varphi_a(r)\frac{\delta^2 E_{XC}}{\delta\rho(r)\delta\rho(r')}\varphi_b^*(r')\varphi_j^*(r') \tag{2.84}$$

In analogy to TDHF and CIS, the Tamm-Dancoff approximation (TDA) to TD-DFT has also been introduced [69]. It corresponds to neglecting the matrix $\mathbf{B}$ in eq. (2.81), that is, only the occupied-virtual block of the initial $\mathbf{K}=\mathbf{X}+\mathbf{Y}$ matrix (2.81) is taken into account. This leads to a Hermitian eigenvalue equation

$$\mathbf{AX}=\omega\mathbf{X} \tag{2.85}$$

where the definition of the matrix elements of $\mathbf{A}$ is still the same as in eq. (2.82).
It is worthwhile to note that TDA/TD-DFT is usually a very good approximation to TD-DFT [70]. A possible reason may be that in DFT correlation is already included in the ground state by virtue of the XC functional, which is not the case in HF theory. Since the magnitude of the $\mathbf{Y}$ amplitudes and the elements of the $\mathbf{B}$ matrix are a measure for missing correlation in the ground state, they should be even smaller in TD-DFT than in TD-HF and, thus, be less important. TD-DFT is also more resistant to triplet instabilities than TD-HF.

2.5 Analytical Gradients of LR-KS energy

Since molecular properties can be derived as analitical derivatives of the system energy, an important advance for Quantum Chemical applications of TD-DFT has been the implementation of analytic derivatives [19],[20] for TD-DFT excited states.
This is primarily a matter of calculating

$$\omega^{\xi} = \frac{\partial \omega}{\partial \xi}$$

to add to

$$E^{\xi}_{GS} = \frac{\partial E_{GS}}{\partial \xi}$$

to obtain

$$E^{\xi}_{K} = \frac{\partial E_{K}}{\partial \xi},$$

the derivative of the energy of the excited state K with respect to a generic perturbation ξ.
This derivative expression

$$\begin{aligned}\omega^{\xi}_{K} = &\frac{1}{2}\langle \mathbf{X}_K + \mathbf{Y}_K | (\mathbf{A}+\mathbf{B})^{\xi} | \mathbf{X}_K + \mathbf{Y}_K \rangle + \\ &\frac{1}{2}\langle \mathbf{X}_K - \mathbf{Y}_K | (\mathbf{A}-\mathbf{B})^{\xi} | \mathbf{X}_K - \mathbf{Y}_K \rangle \end{aligned} \tag{2.86}$$

does not involve the derivatives of the excitation amplitudes [i.e., the left and right eigenvectors of eq. (2.81)] because they have been variationally determined, but it does require the knowledge of the change in the elements of Fock matrix in the MO basis which in turn requires the knowledge of the MO coefficients derivatives, which are the solution of the couple perturbed Kohn-Sham equations (CPKS).
It is well known, however, that there is no need to solve the CPKS equations for each perturbation, but rather only for one degree of freedom, to find the so called Z-vector or relaxed density, which represents the orbital relaxation contribution to the one-particle density matrices (1PDM) involved in all post-SCF gradient expressions.

$$\mathbf{P}^{K} = \mathbf{P}^{0} + \mathbf{P}^{K}_{\Delta} \tag{2.87}$$

$$\mathbf{P}^{K}_{\Delta} = \mathbf{T}^{K} + \mathbf{Z}^{K} \tag{2.88}$$

The $\mathbf{T}^K$ contains the occupied-occupied and virtual-virtual blocks of $\mathbf{P}^\Delta$

$$\begin{aligned} P^\Delta_{kl} &= -\frac{1}{2}\sum_a [(X+Y)_{ka\sigma}(X+Y)_{al\sigma} \\ &\quad +(X-Y)_{ka\sigma}(X-Y)_{al\sigma}] \end{aligned} \tag{2.89}$$

$$\begin{aligned} P^\Delta_{bc} &= -\frac{1}{2}\sum_i [(X+Y)_{ib\sigma}(X+Y)_{ci\sigma} \\ &\quad +(X-Y)_{ib\sigma}(X-Y)_{ci\sigma}] \end{aligned} \tag{2.90}$$

The $\mathbf{Z}^K$ matrix in eq. (2.88) collects the occupied-virtual blocks of $\mathbf{P}^\Delta$. Such blocks are obtained by solving the following Z-vector equation [20]:

$$G^+_{ai\sigma}[P^\Delta_{bj}] + \delta_{ab}\delta_{ij}\delta_{\sigma\sigma'}(\varepsilon_{a\sigma} - \varepsilon_{i\sigma})P^\Delta_{ai\sigma} = L_{ai\sigma} \tag{2.91}$$

where we define two contractions of a nonsymmetric density matrix $\mathbf{P}$ with the four-indexes portion of the $\mathbf{A}+\mathbf{B}$ and $\mathbf{A}-\mathbf{B}$ matrices into the two-electron integrals portion of a nonsymmetric Fock-like matrix, i.e.

$$\begin{aligned} G^+_{pq\sigma}[P_{rs}] = \sum_{rs\sigma'} \big[2(pq\sigma|rs\sigma') + 2f^{Xc}_{pq\sigma,rs\sigma'} \\ -c_X\delta\sigma\sigma' \left[(ps\sigma|rq\sigma') + (pr\sigma|sq\sigma')\right]\big] P_{rs\sigma'} \end{aligned}$$

$$G^-_{pq\sigma}[P_{rs}] = \sum_{rs\sigma'} \left[\left[(ps\sigma|rq\sigma') + (pr\sigma|sq\sigma')\right]\right] P_{rs\sigma'} \tag{2.92}$$

The Lagrangian $L_{ai\sigma}$ depends only from occupied-occupied and virtual-virtual blocks of $\mathbf{P}^\Delta$, i.e T^K_{ij} and T^K_{ab}

$$L_{ai\sigma} = C1_{ai\sigma} - C2_{ai\sigma} + G^+_{ai\sigma}[P^\Delta_{kl}] + G^+_{ai\sigma}[P^\Delta_{bc}] \tag{2.93}$$

$$\begin{aligned} C1_{ai\sigma} &= \sum_b (X+Y)_{bi\sigma}G^+_{ba\sigma}[(X+Y)_{rs}] \\ &\quad +\sum_b (X-Y)_{bi\sigma}G^-_{ba\sigma}[(X-Y)_{rs}] \\ &\quad +\sum_b (X+Y)_{bi\sigma}G^{Xc}_{ba\sigma}[(X+Y)_{rs}] \end{aligned} \tag{2.94}$$

$$
\begin{aligned}
C2_{ai\sigma} &= \sum_j (X+Y)_{aj\sigma} G^{+}_{ij\sigma}[(X+Y)_{rs}] \\
&\quad + \sum_j (X-Y)_{aj\sigma} G^{-}_{ij\sigma}[(X-Y)_{rs}] \qquad (2.95)
\end{aligned}
$$

This allows the calculation of excited-state structure and properties such as true dipole moments, rather than just transition dipole moments, showing that such properties are also accessible from TD-DFT [20].

2.6 Critical analysis of fuctionals performances in LR-KS: a new diagnostic index

From an applicative point of view, the use of LR-KS approach to TD-DFT in combination with approximated XC functionals presents some difficulties in describing charge transfer (CT) and Rydberg (Ry) excitations, absorption spectra of systems with many electron excitations (such as in polyenes) or with open shell ground state [25],[24]. In any case, in the literature there are extended studies showing the very good TD-DFT performances in reproducing excitation energies for transitions with a local character, such as n-π^* and π-π^* [26]-[30]. The situation, however, is more complicated than what it could appear as, in some cases, TD-DFT well performs also for those excitations for which we expect possible failures, such as intramolecular charge transfer excitations[71]. Here an analysis on the performances of the Linear Response (LR) TD-DFT approach in determining electronic excitation energies is presented. The analysis is focused on local or nonlocal changes in the electronic density and on the role played by the Hartree Fock Exchange (HF-X). We introduce a new diagnostic index linked to the variation in the charge centroid of the single electron components of the excitation. It is shown how this index can be used as a diagnostic test for the description of the nature of the excitation studied by different hybrid functionals. It is in fact difficult to achieve a clear and unequivocal picture only by looking at the molecular orbitals involved, especially for large systems.
We compare the new index with the $\mathbf{\Lambda}$ index proposed by Tozer and collaborators [72], which is based on the overlap of the absolute value of the molecular orbitals involved in the excitation, and we analyse the respective potentialities in achieving a good diagnosis of TD-DFT accuracy with Rydberg and charge-transfer excitations. Finally, we show that the principal effect of increasing the HF-X percentage is to increase orbital energy differences, making any analysis based only on the evaluation of shape and extension of molecular orbitals not enough to obtain an exhaustive diagnostic index for TD-DFT users.

2.6.1 Definition of the Γ index

In 2003, Dreuw et Al. [73] showed that, in the case of intermolecular CT (iCT), for which the product function $\phi_i(r)\phi_a(r) \rightarrow 0$,

$$A^{iCT}_{ia\sigma,jb\tau} = \delta_{ij}\delta_{ab}\delta_{\sigma\tau}(\varepsilon_a - \varepsilon_b) - C_{HF}\delta_{\sigma\tau}\langle i_\sigma a_\sigma | j_\tau b_\tau\rangle \quad (2.96)$$

$$B^{iCT}_{ia\sigma,jb\tau} = 0 \quad (2.97)$$

Starting from this point, a diagnostic test, based on the overlap of absolute values of molecular orbitals, was recently presented by Peach et al. [72], to analyse the performance of XC functionals in reproducing local, Rydberg and intramolecular CT excitations. They proposed index is defined as:

$$\mathbf{\Lambda} = \frac{\sum_{ia} K_{ia}^2 \int |\phi_i(r)||\phi_a(r)|dr}{\sum_{ia} K_{ia}^2} \quad (2.98)$$

where

$$K_{ia} = X_{ia} + Y_{ia} \quad (2.99)$$

This index measures the overlap between the different KS orbitals involved in the excitation, and, for GGA and hybrid functionals, it can be correlated to the error of TD-DFT excitation energies with respect to more correlated wave function based methods. However,as the authors themselves pointed out, a correlation between the errors and Λ values is present only for Λ values lower than 0.4 for GGA and 0.3 for hybrid functionals. By contrast, for $\Lambda > 0.4$ we cannot be sure to obtain accurate values of excitation energies by using hybrid functionals [74]. It is also worth noting that the range-separated hybrid functionals, such as CAM-B3LYP do not show this correlation between excitation energy errors and values of Λ [72].

Our considerations start from the observation that the TD-DFT low accuracy in describing CT excitations (both intra or intermolecular) or Rydberg excitations is linked to a not correct description of the local variation of electronic density during excitation. As Ziegler et al.[75] recently pointed out, the GGA Hessian can be used to describe changes in energy due to small perturbations of electron density, but it should not be applied to one-electron excitations involving the density rearrangement of a full electron charge. The Hartree-Fock Hessian describe larger pertubations to electron density, due to the complete self interaction cancellation by mean of exact exchange that is only partially taken into account in hybrid functionals. Therefore, an index able to describe the amount of this spatial rearrangement could warn the user when the XC-functional is inadequate. We expect a small variation of electron density for local valence excited states and higher values in the case of Rydberg or CT states. We define the index, Γ, in order to describe the variation of the single electron charge sferoids after excitation as:

$$\Gamma = \sum_{ia} K_{ia}^2 \Delta_{ia} \tag{2.100}$$

where

$$\Delta_{ia} = |\Delta_a - \Delta_i| = ||\langle\phi_a|r^2|\phi_a\rangle - \langle\phi_a|r|\phi_a\rangle^2| - |\langle\phi_i|r^2|\phi_i\rangle - \langle\phi_i|r|\phi_i\rangle^2|| \tag{2.101}$$

By definition, Γ constitutes a measure of the difference of the variance of electronic position in passing from occupied to virtual orbital. It is the difference between the size of the molecular orbitals involved in the description of the transition, if we represent the *size* by a sphere of radius equal to the root mean square of the distance of the electron in the orbital from the centroid of charge[76]. We note that Γ is not a limited quantity. We implement Γ in a locally modified version of G09 program, by the use of first and second moments in the atomic orbital basis set.

2.6.2 Systems and methods.

We analysed twelve different molecular systems: N_2, CO, H_2CO, HCl, Tetracene, DMABN, a model Dipeptide, Benzene, IDMN, JM, Prodan and TriazeneII (the relative structures are showed in figure 2.1).
They span a large set of different excitations, namely local, Rydberg and CT.

TriazeneII was studied by Preat et al.[77], and its excitation energies were analysed in terms of Λ by Peach et al. IDMN, JM and Prodan systems are examples of charge transfer in extended systems with delocalization of charge. Benzene is a typical Rydberg system as N_2, CO, H_2CO.
All DFT and TD-DFT calculations have been carried out with a locally modified version of the G09 program [78], using different exchange-correlation functionals characterized by a different Hartree-Fock exchange (HF-X) contribution. They include 3 global hybrids (GH), namely B3LYP [50] (20% of HF-X), PBE0 [54] (25% of HF-X) and BH&HLYP [79] (50% of HF-X) and one Range-Separated Hybrid (RSH), CAM-B3LYP [63]. A pure GGA functional is also tested, namely PBE [45], to compare data obtained by Tozer and co-workers [72],[74].
The extended basis set d-aug-cc-pVTZ was selected to compute excitation energies of N_2, CO, H_2CO, and Benzene in order to achieve converged results for Rydberg excitations [80] and to compare with the results of Peach et Al [72]. The other systems were studied using the cc-pVTZ basis set.
Finally, for Triazene II system the 6-311+G(2d,p) basis set was used, to make a direct comparison with Preat [77] and Peach [74] results . SAC-CI calculations were performed for IDMN, JM and Prodan, respectively with cc-pVTZ,

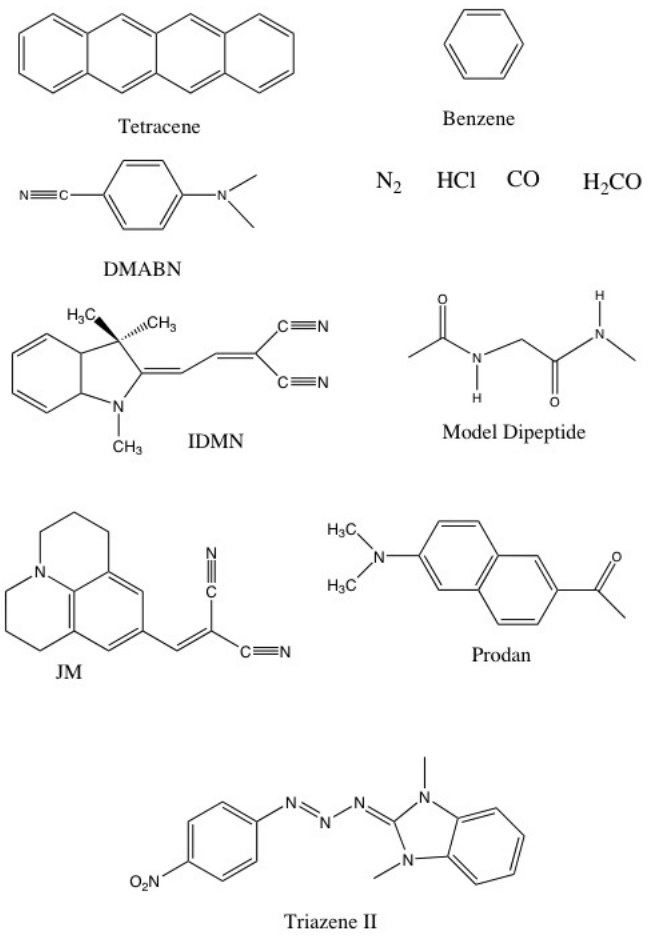

Figure 2.1: Structures of studied systems

6-311G(d) and 6-31+G(d) basis sets, by fixing tightest level of convergence (level three). Ground state geometry calculations were performed at MP2/6-31G(d) level, with the exception of N_2 and CO (experimental geometries [81]) and TriazeneII, for which we use the geometry reported in ref. [77] for PBE, PBE0 and CAM-B3LYP TD-DFT calculations.
We check that ground state geometries are actual minima by performing harmonic vibrational frequency calculations of all optimized structures.

2.6.3 Results and Discussion

In this section we analyse the performance of different functionals in determining vertical excitations energies in terms of the two indexes Λ and Γ.
We recall here that for GGA and hybrid functionals, Tozer et al. have shown that Λ values lower than 0.3 and 0.4, respectively are usually correlated with large errors.
We individuate three main type of excitations, namely Local (L), Rydberg (Ry) and intramolecular Charge Transfer (CT), and discuss correlations between the error reported by each functional and values of Λ and Γ for each set. The term *error* is here used to refer to the differences in the excitation energy obtained at TD-DFT level with respect to the reference data obtained with more correlated methods. More in detail, the errors are defined as TD-DFT minus reference values.
Let us start the analysis with local excitations in N_2, CO, H_2CO, Benzene, Tetracene, DMABN and model dipeptide. In figure 2.2 we report plots of TD-DFT errors in function of both indexes and correlation plots between Λ and Γ.
In general local excitations are well reproduced by all functionals for all systems, the absolute overlap is large and the reorganization of charge is usually small. Coherently we find large values of Λ (typically 0.5-0.8) and small values of Γ, most of which are in the range 0-5. Greater values are obtained with BH&HLYP and CAM-B3LYP functionals in the case of small systems, for which larger errors are obtained.
For all functionals when Γ increases, Λ decreases. As Γ index constitutes a measure of the *size* difference between the MOs involved in the transition, one can see that the excitations here studied involve MOs that are quite similar.
We expect that the Γ index here defined is more sensitive in describing excitations that involve transitions to more diffuse orbitals such as in Rydberg transitions reported in figure 2.3. As figure 2.3 shows, for $\Gamma > 60$ excitation energies are quite accurate (i.e. absolute values of the error are lower than 0.5 eV). In general, for such kind of excitations $\Lambda < 0.3$ and therefore the use of only this index is not able to warn the user about the real performances of the

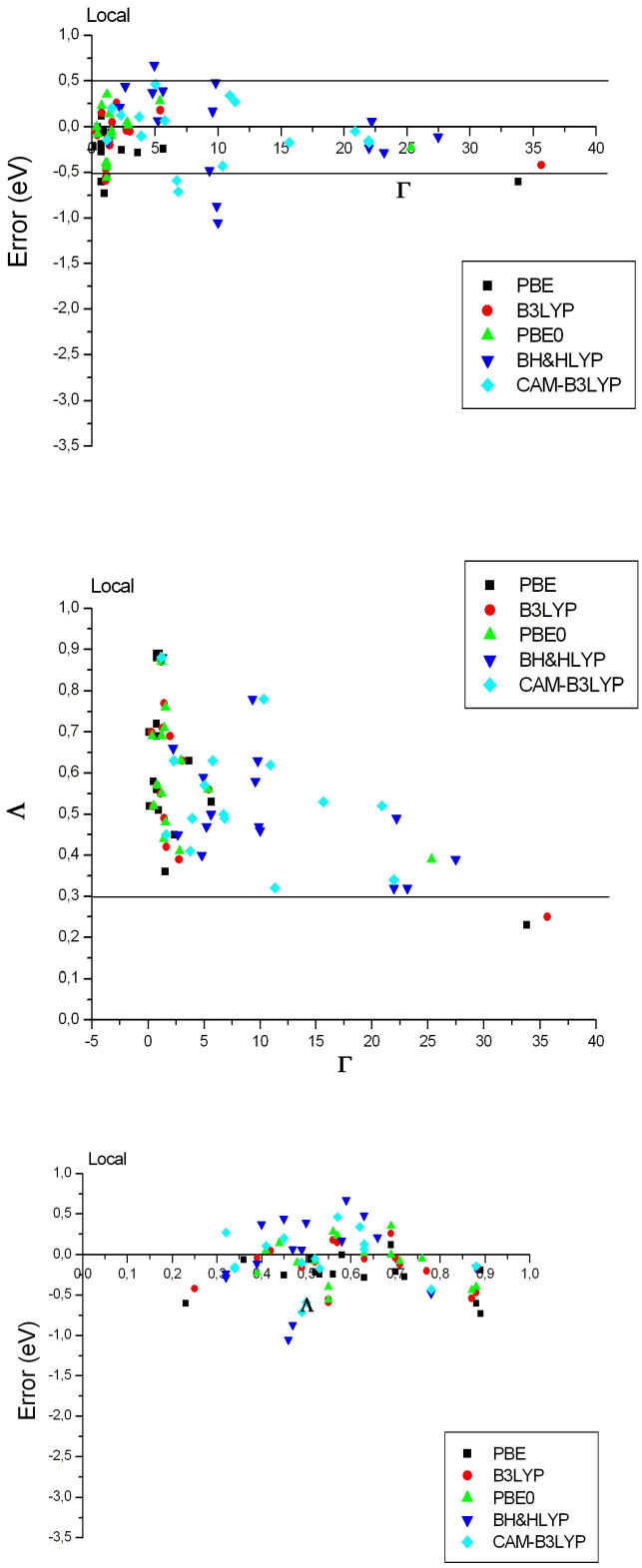

Figure 2.2: TD-DFT dispersion data for Local excitation

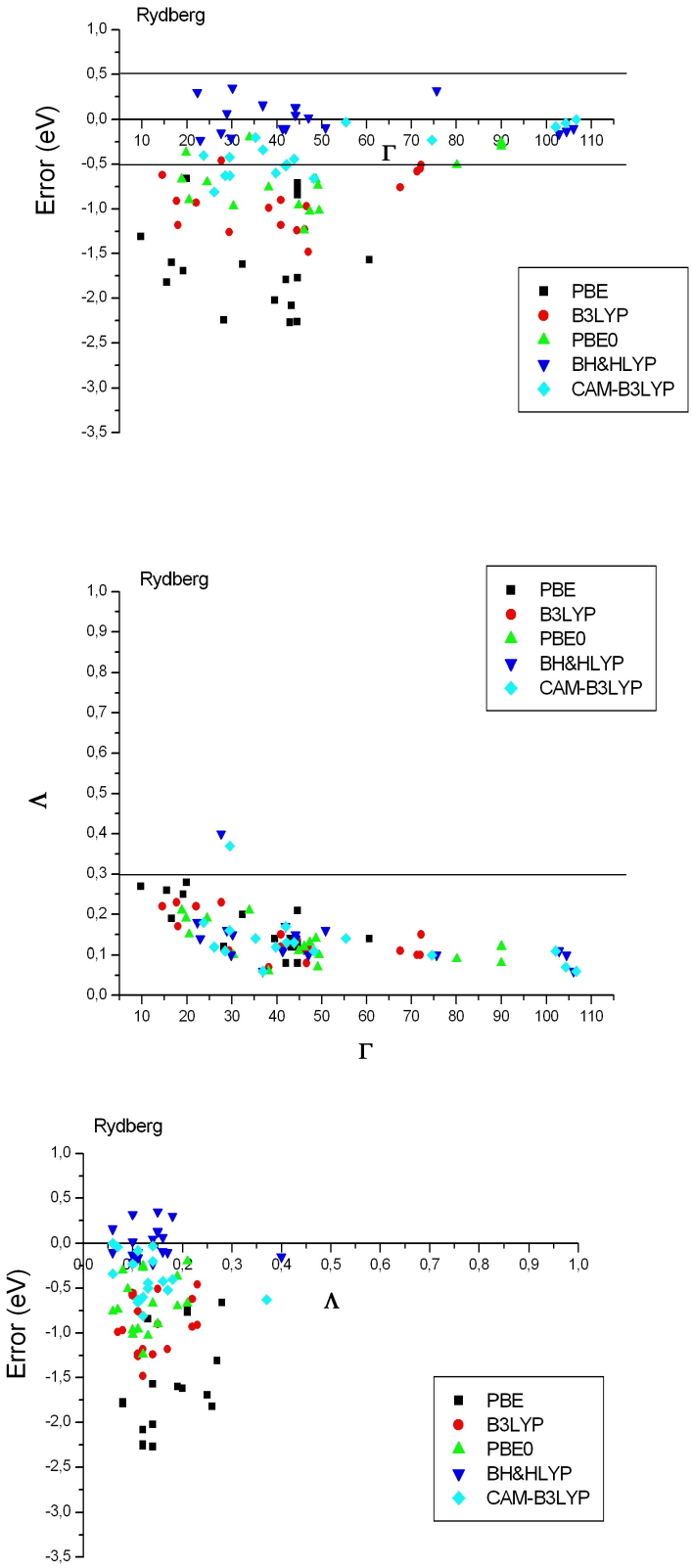

Figure 2.3: TD-DFT dispersion data for Rydberg excitation

selected functional.
PBE calculations of the Rydberg excitations here studied give $\Gamma < 60$ and absolute errors larger than 0.5 eV. B3LYP and PBE0 values are very similar to PBE ones, and errors decrease to the range of $\pm$ 0.5 eV for $\Gamma > 65$. BH&LYP and CAM-B3LYP functionals, that include a greater HF-X percentage, present lower Γ threshold. As a matter of fact, BH&LYP results are all in the error range of $\pm$ 0.5 eV, but this is not the case for the CAM-B3LYP ones applied to the diatomics systems (N_2 and CO). This indicate that for these small systems, the long range part of the functional is not fully exploited and therefore the effective HF-X percentage is lower than the long-range value (65%). However, for $\Gamma \geq 50$, CAM-B3LYP calculations became accurate.
It is worth noting that, as Casida et Al [82] pointed out, for high-lying bound states there is a collapse of the states above the TD-DFT ionization threshold, which is at $-\varepsilon_{HOMO}$. This is true not only in the case of LDA functional, but also for GGA and hybrids as it is possible to see comparing tables 2.1 and 2.2. If the excitation energy that one try to reproduce by mean of TD-DFT is greater than the ionization potential calculated by the functional used (i.e. the limit for bound excited states for that functional), the value of the excitation energy will be underestimated.

Moving to CT excitations, the corresponding plots are shown in figure 2.4. The classification of these excitations as CT is based on previous studies. However, the present analysis based on the two indexes seems to suggest that an extension of ths common classification of CT states is needed. In fact, for the excitations here investigated, Γ shows values lower than 5 (with the exception of the twisted DMABN), exactly as found for local excitations.
From the three plots reported in figure 2.4, it seems possible to distinguish at least two types of CT excitations. The first type, that we call *delocalized* CT, is characterized by $\Lambda \approx 0.7$ (planar DMABN, IDMN, JM and Prodan) and it involves a transition very similar to a local $\pi - \pi^*$ excitation delocalized on the molecule ($\Gamma \approx 1$ or 4).
The second type (DMABN twisted to 90^o, model dipeptide), that we call *localized* CT, is characterized by a more evident charge transfer from a well localized part of the molecule to another one. In this case, low overlaps ($0.2 < \Lambda < 0.5$) are found. The size difference can be more or less pronounced in function of the symmetry ($\Gamma \approx 2$ in the case $n_1 - \pi_2^*$ and $\pi_1 - \pi_2^*$ of model dipeptide, $\Gamma \approx 6$ in the case of twisted DMABN).

In the case of CT transitions, the analysis based on the size (Γ) and the absolute overlap (Λ) of the KS MOs does not seem to allow us to define a

N_2		PBE			B3LYP			PBE0			BH&HLYP			CAM-B3LYP		
Ref	Sym	ΔE	Λ	Γ	ΔE	Λ	Γ	ΔE	Λ	Γ	ΔE	Λ	Γ	ΔE	Λ	Γ
12.20	$^1\Sigma_g^+$	-1.82	0.26	15.60	-0.91	0.23	17.67	-0.67	0.21	18.85	0.30	0.18	22.31	-0.40	0.18	23.66
12.90	$^1\Pi_u$	-2.26	0.12	44.56	-1.23	0.11	46.29	-0.97	0.10	30.36	-0.23	0.14	22.97	-0.63	0.11	28.54
12.98	$^1\Sigma_u^+$	-2.24	0.12	28.18	-1.26	0.11	29.43	-1.02	0.10	49.45	0.02	0.10	47.11	-0.66	0.11	48.31
13.24	$^1\Pi_u$	-1.60	0.19	16.60	-1.18	0.17	18.01	-0.90	0.15	20.48	-0.21	0.10	29.88	-0.81	0.12	26.05

CO		PBE			B3LYP			PBE0			BH&HLYP			CAM-B3LYP		
Ref	Sym	ΔE	Λ	Γ	ΔE	Λ	Γ	ΔE	Λ	Γ	ΔE	Λ	Γ	ΔE	Λ	Γ
10.78	B $^1\Sigma^+$	-1.69	0.25	19.19	-0.93	0.22	22.06	-0.7	0.19	24.48	0.07	0.16	28.90	-0.42	0.16	29.50
11.40	C $^1\Sigma^+$	-2.02	0.14	39.55	-1.18	0.12	40.93	-0.96	0.11	44.91	-0.10	0.11	41.35	-0.60	0.12	39.79
11.53	E $^1\Pi$	-2.08	0.12	43.26	-1.24	0.14	44.51	-1.03	0.14	47.37	-0.15	0.40	27.62	-0.63	0.37	29.55
12.40	F $^1\Sigma^+$	-2.27	0.14	42.95	-1.48	0.12	47.01	-1.24	0.12	46.12	-0.23	0.11	41.97	-0.73	0.10	41.97

H_2CO		PBE			B3LYP			PBE0			BH&HLYP			CAM-B3LYP		
Ref	Sym	ΔE	Λ	Γ	ΔE	Λ	Γ	ΔE	Λ	Γ	ΔE	Λ	Γ	ΔE	Λ	Γ
7.09	$^1B_2$	-1.31	0.27	9.82	-0.62	0.22	14.62	-0.37	0.19	19.83	0.35	0.15	30.13	-0.20	0.14	35.25
7.97	$^1A_1$	-1.57	0.14	60.61	-0.76	0.11	67.56	-0.51	0.09	80.12	0.32	0.10	75.69	-0.23	0.10	74.61
8.12	$^1B_2$	-1.62	0.20	32.36	-0.90	0.15	40.93	-0.67	0.14	48.72	0.05	0.14	44.20	-0.50	0.13	42.22
8.38	$^1A_2$	-1.77	0.08	44.64	-0.97	0.08	46.65	-0.74	0.07	49.18	0.13	0.15	44.20	-0.44	0.13	43.88
9.22	$^1A_2$	-1.79	0.09	42.05	-0.99	0.07	38.26	-0.76	0.06	38.20	0.16	0.06	36.94	-0.34	0.06	36.88

Benzene		PBE			B3LYP			PBE0			BH&HLYP			CAM-B3LYP		
Ref	Sym	ΔE	Λ	Γ	ΔE	Λ	Γ	ΔE	Λ	Γ	ΔE	Λ	Γ	ΔE	Λ	Γ
6.45	$^1E_{1g}$	-0.66	0.28	19.91	-0.46	0.23	27.67	-0.20	0.21	33.90	-0.09	0.16	50.90	-0.03	0.14	55.40
6.98	$^1A_{2u}$	-0.71	0.21	44.63	-0.51	0.15	72.21	-0.25	0.12	90.04	-0.16	0.11	102.87	-0.08	0.11	102.10
7.04	$^1E_{2u}$	-0.77	0.21	44.63	-0.55	0.10	71.99	-0.27	0.12	90.11	-0.13	0.10	104.51	-0.04	0.07	104.26
7.12	$^1A_{1u}$	-0.84	0.13	44.65	-0.58	0.10	71.33	-0.30	0.08	90.04	-0.10	0.06	106.06	0.00	0.06	106.62

Table 2.1: TD-DFT/d-AUG-cc-pVTZ Excitation Energy(eV), Λ and Γ values for Rydberg excitation. N_2, CO and H_2CO: see reference values reported in table 1 of [72]. Benzene ref. [83]

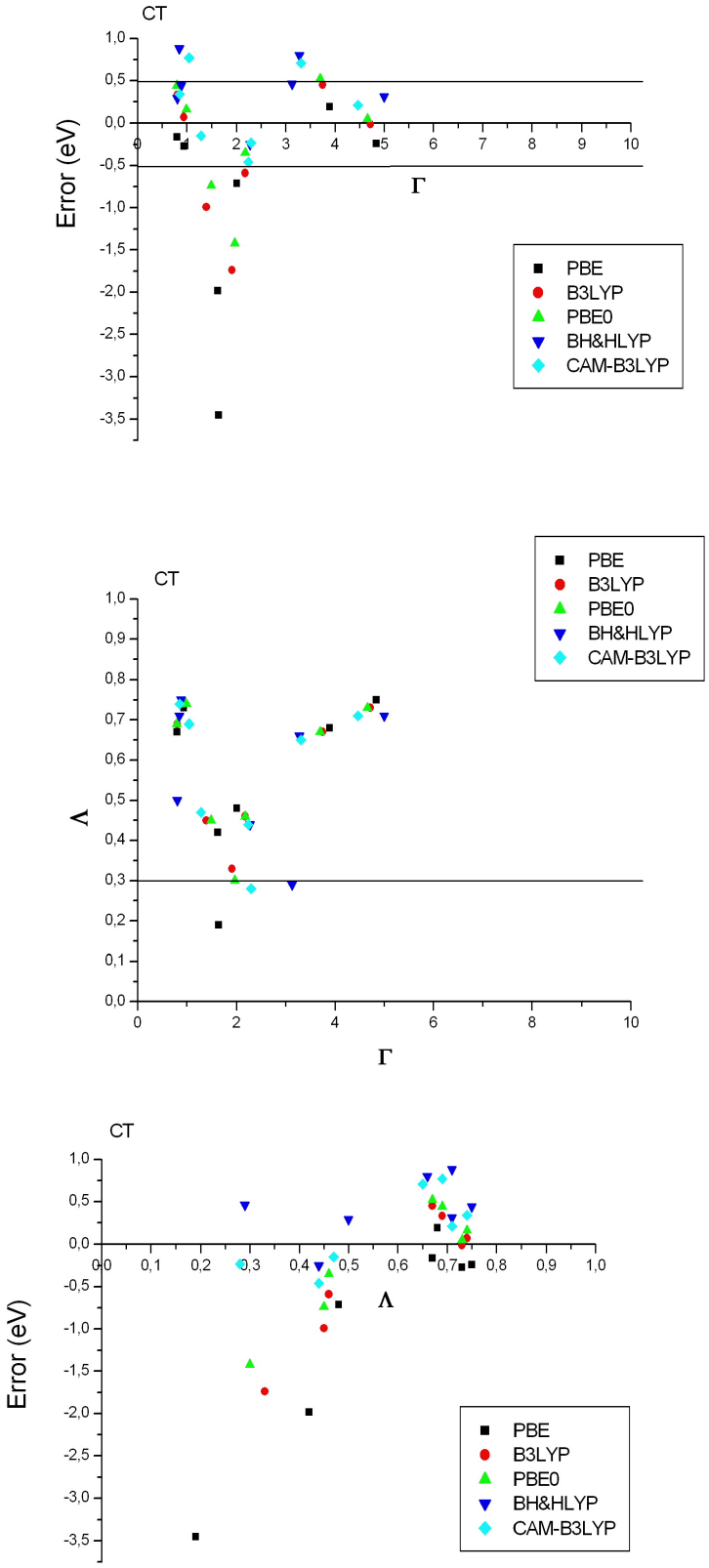

Figure 2.4: TD-DFT dispersion data for CT excitation

$-\varepsilon_{HOMO}$	PBE	B3LYP	PBE0	BH&HLYP	CAM-B3LYP
N_2	10.26	11.96	12.20	14.16	13.88
CO	9.04	10.53	10.74	12.45	12.38
H_2CO	6.27	7.70	7.91	9.55	9.41
Benzene	6.34	7.09	7.31	8.08	8.52
Tetracene	4.64	5.16	5.34	5.84	6.29
HCl	7.95	9.15	9.44	10.78	10.88
Dipeptide	5.39	6.82	7.09	8.52	8.58
DMABN	5.25	6.04	6.23	7.09	7.38
IDMN	5.27	5.93	6.11	6.83	7.15
JM	5.12	5.80	5.97	6.72	7.02
Prodan	4.78	5.49	5.66	6.41	6.74

Table 2.2: TD-DFT -ε_{HOMO} (eV) of studied systems

clear threshold of accuracy, as transitions with high Λ but errors greater than 0.5 eV are present. The reason is correlated to the fact that Λ calculates a weighted absolute overlap (a condition that comes from ortogonality of MOs), i.e. an absolute average of the MOs product of the hole-particle pairs and the phase sign can not be taken in account by definition.
However, the contribution of bielectronic terms in the TD-DFT matrices **A** and **B** (see eqs.2.82-2.83) comes from the value of the product $\phi_a(r)\phi_i(r)$ at each point r in the integration domain. A very small value of Λ implies $\phi_a(r)\phi_i(r) \rightarrow 0$, as the absolute overlap is a stronger condition but the opposite is not in general true, as the phase sign is neglected.

Since the bielectronic terms in the linear response Hessian depend on the inverse of the inter-electronic distance, one can try a different analysis in terms of the average distance between the hole particle components of the excitation by mean of the charge centroid difference:

$$\Delta r = \sum_{ia} K_{ia}^2 |\langle a|\overrightarrow{r}|a\rangle - \langle i|\overrightarrow{r}|i\rangle| \tag{2.102}$$

However, for the cases here studied, the informations that is possible to get are almost complementary to that of Λ index. The plot of the error on the CT transitions in function of Δr is shown in figure 2.5.

From the plot it appears that for PBE, B3LYP and PBE0, transitions that involve orbitals with centroid distance greater than 2 $\mathring{A}$ become less accurate. No clear trends appear for the other functionals.

Let us go back to the excitation energy expression in the linear response approach in order to assess the influence of the different XC functional on the

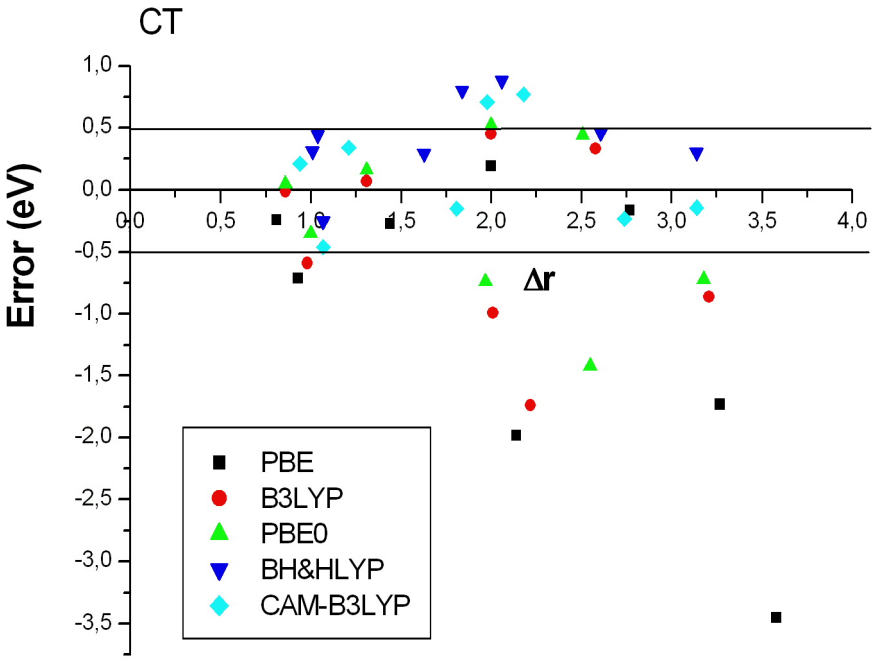

Figure 2.5: TD-DFT charge centroid diffences of the CT transitions studied

errors. We consider, for simplicity, the Tamm-Damcoff approximation to the TD-DFT, eq. (2.85). Therefore

$$\begin{aligned}\omega &= \sum_{ia} K_{ia}^2(\varepsilon_a - \varepsilon_i) + \sum_{ia,jb} K_{ai}^* K_{jb}[\langle ij|ab\rangle + \\ &\quad -C_{HF}\langle ia|jb\rangle + (1 - C_{HF})\langle ij|f_{xc}|ab\rangle] \end{aligned} \tag{2.103}$$

In equation (2.103), the first term is the zero order contribution to the excitation energy, and it depends on the ground state calculation. This term is not affected by the product of the hole and particle functions. The HF-X percentage of the functional however affects the energy gap between the orbitals. The terms in square brackets, the Hessian of the bi-eletronic component of the Fock operator, contain:

- the occupied-virtual, occupied-virtual Coulomb interaction,
- the occupied-occupied, virtual-virtual Coulomb interaction (due to the non-local HF-X potential),
- the local XC potential, that is once again of the type occupied-virtual, occupied-virtual.

The first and the third of these first order terms depend on the distance, the overlap and the different "size" and "shape" of the the orbitals involved in the transition. They correct the zero-order orbital-gap term with a positive contribution. The Hartree-Fock exchange is a negative term, and it depends on the inverse of the distance. To have a clearer picture, we analyse the correlation between the energy excitation errors and these terms.

The plot in figure 2.6 shows the errors in function of the MO's gaps term $\sum_{ia} K_{ia}^2(\varepsilon_a - \varepsilon_i)$ for each CT excitation here studied.

Also within this framework, the presence of the two different types of CT transition is evident. For the *localized* CT (twisted DMABN, $n_1 - \pi_2^*$ and $\pi_1 - \pi_2^*$ of model dipeptide), increasing the HF-X percentage increases the MO's gaps term and the errors decrease. This is true also for the diatomic HCl. On the contrary, for the "delocalized CT" in the extended systems (planar-DMABN, IDMN, JM and Prodan) errors increase when the zero order term increases.

Figure 2.7 shows the same plot for the first order term, obtained as the difference between the excitation energies and MOs gap term.

In the case of *localized* CT, errors increase with increasing this term, while an opposite behavior is found for the *delocalized* CT. This result shows that for the two types of intramolecular charge transfer excitations, the effect of the HF-X percentage in the functional is different.

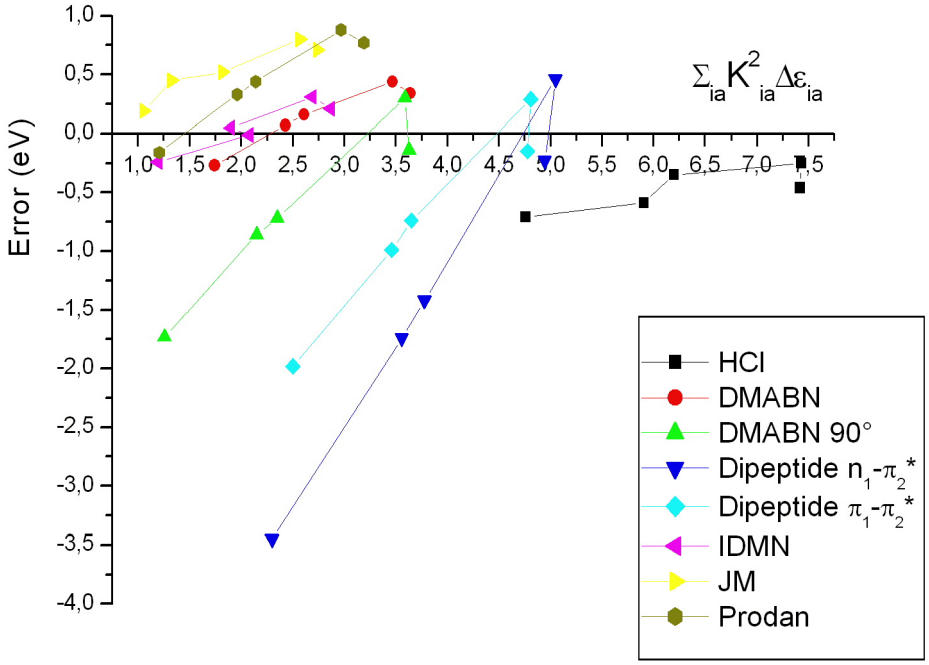

Figure 2.6: TD-DFT errors in function of the orbital gaps term of Linear Response

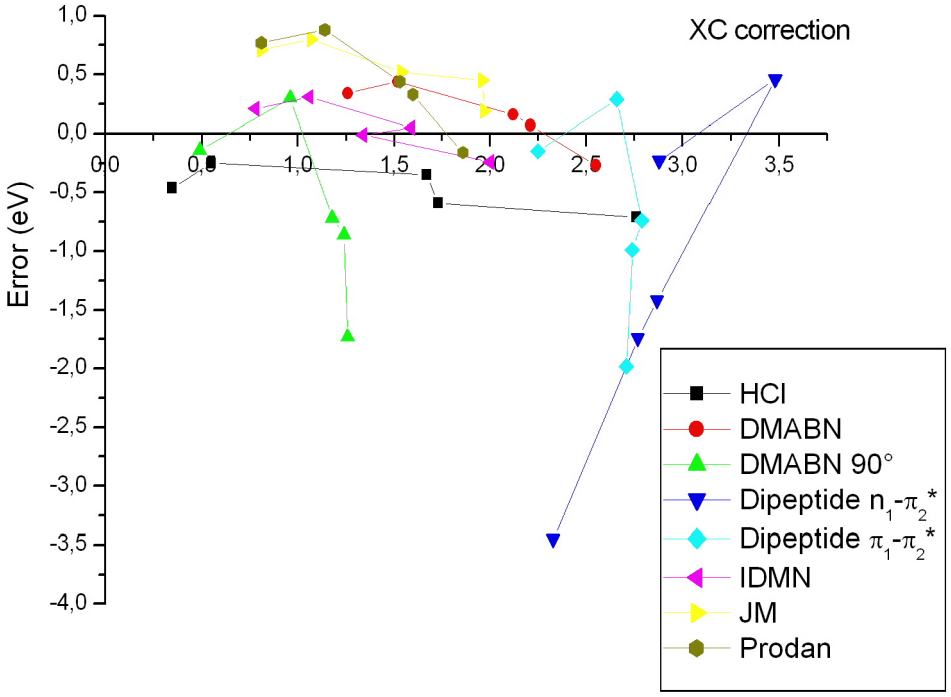

Figure 2.7: TD-DFT errors in function of the Coulomb-XC term of Linear Response

In the case of *localized* charge transfer, the main effect is on the SCF step, from which one obtains the orbital energies. This effect is quite similar as we observed for the Rydberg states, for which excitation energies are sensible to the ionization threshold.
On the contrary, for the *delocalized* CT transitions the main effect of the HF-X percentage is on the first order term in the electronic Hessian, that corrects back the orbital energy difference. This kind of intramolecular excitation is usually low in the energy spectrum, and therefore it cannot be affected by the ionization threshold (see the table 2.2).
Since for CT excitations in push-pull chromophores (where the ground and excited states are delocalized on the whole molecule) we cannot define separated regions for the charge transfer, the Coulombic interactions between the occupied and virtual orbitals (that are described by the nonlocal HF potential) need to be reduced.
If the local Coulomb and XC part of the functional is not able to do this, smaller errors are obtained with reduced HF-X percentage, i.e. hybrid functionals presenting low HF-X percentage. This is the case of DMABN with a planar structure, IDMN, JM and Prodan, where $\Lambda \approx 0.7$ and $\Gamma < 7$ (a small value if compared to those typical of Rydberg cases). One can also expect that, in the case of a push pull chromophore where the transition involves a larger spatial reorganization of charge, but still very delocalized on the molecule, the Coulomb and the local part of the first order terms become more important. Probably this can be assessed exploring the transition density matrix by localization techniques in terms of natural transition orbitals [84].
The increase of the zero-order term explains also the behavior of the various excitations in Triazene II, for which the analysis in terms of the absolute overlap is not sufficient to explain the bad performance of PBE and PBE0 also for absolute overlap values beyond the thresholds proposed [74].
In table 2.3 errors and index values are reported. There are no simple correlations between errors and Λ, Γ and Δr. However, the analysis of the MOs gap and of the first order terms explain the performance of the functional, also in the case with large overlap.
Figure 2.8 shows the results in function of the zero order term. For all excitations, errors reduce in increasing the MOs gap and in passing from PBE to PBE0 and CAM-B3LYP.

	PBE				PBE0				CAM-B3LYP			
Ref	ΔE	Λ	Γ	Δr	ΔE	Λ	Γ	Δr	ΔE	Λ	Γ	Δr
3.03	-1.02	0.49	19.39	2.86	-0.22	0.43	19.22	2.72	0.05	0.41	20.58	2.44
3.34	-0.72	0.64	7.23	3.10	-0.18	0.60	5.28	3.24	0.13	0.59	5.02	3.12
3.90	-0.75	0.40	24.56	3.42	-0.04	0.38	24.87	3.65	0.07	0.38	24.93	3.88
4.53	-1.15	0.65	13.79	2.21	-0.45	0.62	19.34	1.61	0.12	0.62	16.69	1.35
5.00	-2.09	0.49	31.06	1.58	-0.78	0.42	30.03	1.44	0.30	0.42	25.75	1.70
5.04	-1.60	0.57	6.30	5.21	-0.54	0.44	14.12	5.26	0.01	0.64	8.92	1.42
6.02	-2.33	0.30	6.95	4.02	-0.81	0.27	18.36	2.06	-0.09	0.28	6.21	3.09

Table 2.3: TD-DFT/6-311(2d,p) Excitation Energy (eV), Λ and Γ and charge centroid difference Δr values for Triazene II excitation. RI-CC2 reference values from ref [74]

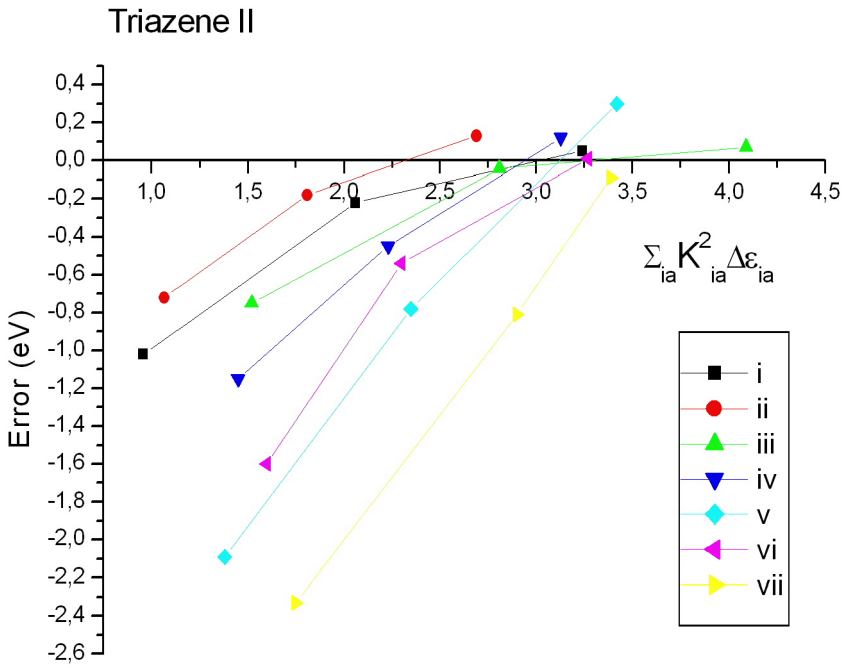

Figure 2.8: Triazene II: TD-DFT errors in function of the orbital gaps term of Linear Response. The i-vii nomenclature is referred to the order of RI-CC2 calculations in table 2.3

2.7 TD-DFT accuracy in determining Single and Double bonds in excited state structures

In literature, nowadays, there are extended studies that show the performances of TD-DFT in reproducing excitation energies and absorption spectra [26]-[30]. However, to the best of our knowledge, systematic investigations of the excited-state structures and fluorescent properties have yet to be carried out. In fact, some works, devoted to the implementation of TD-DFT analytical derivatives, have partially (limited number of molecules and functional) analysed this aspect (see for instance refs [20] and [21]).
The aim of this section is to contribute to fill this gap by unravelling specific behaviors of TD-DFT in comparison with the highly correlated CASPT2 method. To this end, we have considered different XC functionals, whose choice reflects the aim of analysing both the influence of HF-X percentage once the correlation functional was fixed (B3LYP [50], BH&HLYP [79], and CAMB3LYP [63]), and the influence of the description of correlation at almost the same HF-X (B3LYP, B3P86 [50],[85] , and PBE0 [54]). BMK [86] functional is also included to have an intermediate HF-X percentage and to test also a functional originally developed for kinetics and chemical reaction description.

2.7.1 Computational details

All DFT and TD-DFT calculations have been carried out with the G09 program [78], using six different exchange-correlation functionals characterized by a different HF-X contribution. The set includes five global hybrids (GH), B3LYP (20% of HFX), B3P86 (20% of HF-X), PBE0 (25% of HF-X), BMK (42% of HF-X), BHHLYP (50% of HF-X), and one RSH, CAM-B3LYP. Linear response TD-DFT calculations were carried out to obtain vertical excitation energies, and the development of analytical derivatives was used for the exploration of excited-state potential energy surface.
Generally, a medium size basis set (valence double or triple-zeta basis) already gives converged results for valence transitions when both polarization and diffuse functions are added. In particular, Pople's 6-311+G(2d,p) provides converged transition energies of low-lying states for the majority of investigated dyes, while the compact 6-31+G(d) basis represents a valuable compromise between accuracy and computational speed [26],[87].
It has been shown that larger basis sets, including very diffuse functions, are mandatory when higher energy states (e.g., Rydberg) are sought [88]. These

highly excited cases are not treated in this work; therefore, all the calculations (geometry optimization, absorption, and dipole moments) have been carried out with the 6-31+G(d) basis set. However, basis set effects have been tested by using seven small and medium-sized basis sets during TD-DFT optimizations, including Pople's 6-31G(d), 6-311G(d) and Dunning's cc-pVDZ, cc-pVTZ, aug-cc-pVDZ, and aug-cc-pVTZ basis sets [89] for all systems with all functionals used in this study.
The obtained results well underline that the convergence is already reached with the selected basis set, 6-31+G(d) [9].

We appraise the qualities of the selected XC functionals by comparing TD-DFT results to CASPT2/6-31G(d) reference values for which the active space was unambiguously selected, to include the valence molecular orbitals, together with lone pair orbitals where appropriate, as reported in ref [90], and CASPT2/cc-pVDZ as reported in ref [91]. The CASPT2 calculations we have used are carried out without any diffuse function, and thus are probably insufficient to accurately describe excited states that are spatially extended and have partial Rydberg character.
In the present study, however, the interest is in the low-lying valence excited states with a compact electron density. In these cases, we are confident that the selected basis is sufficient to have a correct picture as also shown in the study of Schreiber et al [80].

[9] They are reported and briefly discussed in Appendix A.

2.7.2 Results and Discussion

The core of molecules considered for the present study is constituted by the set of small organic chromophores originally selected by the reference CASPT2 study of Page and Olivucci [90] (see Figure 2.9).

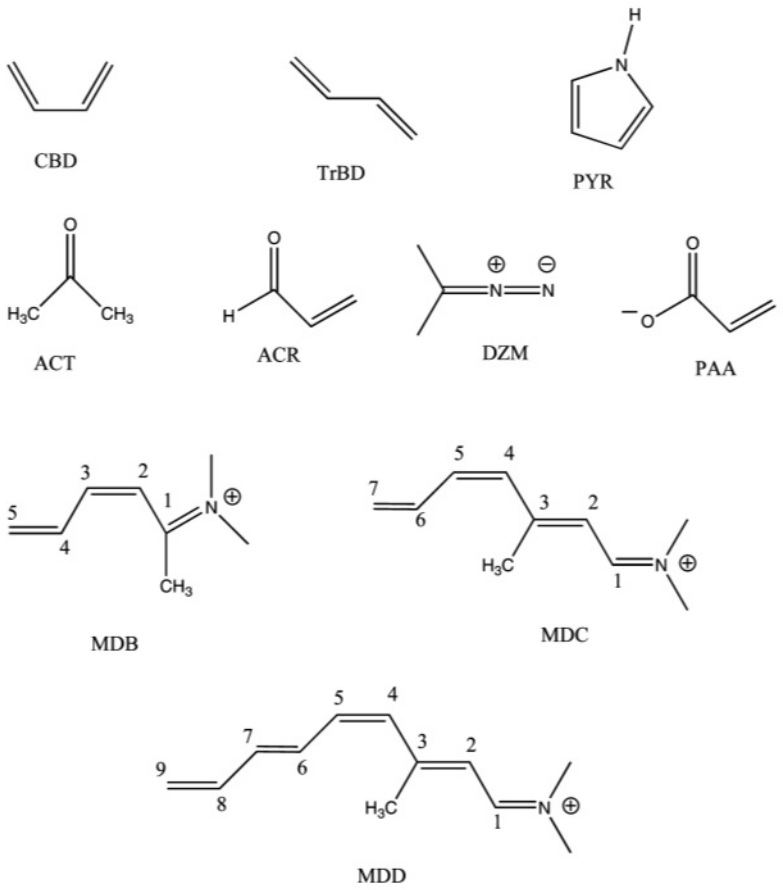

Figure 2.9: Molecular structures of systems considered in this study. From the top: *cis*-buta-1,3-diene (CBD), *trans*-buta-1,3-diene (TrBD), pyrrole (PYR), acrolein (ACR), acetone (ACT), diazomethane (DZM), propenoic acid anion (PAA), and the three protonated Schiff bases (MDB, MDC, and MDD).

Their excitations can be considered as prototypes of $n-\pi^*$ or $\pi-\pi^*$ transitions. As representative examples of $n-\pi^*$ systems, we studied acrolein (ACR), acetone (ACT), propenoic acid anion (PAA), and diazomethane (DZM), whereas *cis*-buta- 1,3-diene (CBD), *trans*-buta-1,3-diene (TrBD), and pyrrole (PYR) constitute the $\pi-\pi^*$ set.

ACR is an example of a conjugated hydrocarbon where the first excited state corresponds to a $n - \pi^*$ transition, and it can be compared to ACT and PAA to get more insights on the impact of the conjugation on $n - \pi^*$ excited-state structures. DZM is a model structure for studying $n - \pi^*$ excitation in diazo-compound.
CBD and TrBD are representative systems of the class of conjugated hydrocarbons, and they are used to study $\pi - \pi^*$ excitations. Finally, PYR is a cyclic nitrogen-bearing compound, allowing one to compare the C-N bond behavior in $\pi - \pi^*$ excitations.
As a further analysis, the original set of molecules has been supplemented with three chromophores belonging to the class of protonated Schiff bases (PSB) that present $\pi - \pi^*$ excitations (from now on they will be labeled as MDB, model B, MDC, model C, and MDD, model D; see Figure 2.9).

Recently, these chromophores have been used as model systems in an investigation of the structure relaxation in the excited state of 11-*cis*-retinal by means of CASSCF, CASPT2, CC, and QMC methods [91]. Note that the description of the excited states of medium and large PSB or related cyanine-like molecules remains challenging for TD-DFT that tends to overestimate the transition energies [92],[93]. It appears that RSH functional cannot cure the problem [66], although the incorrect TD-DFT predictions are probably not related to the multideterminantal nature of these compounds [94] .

Ground-State Structures: DFT versus CASPT2

Some of the considered functionals (e.g., B3LYP, B3P86, PBE0, BMK) have been accurately tested on a large number of molecular properties, including ground-state structures of organic molecules. In particular, errors of about 0.01 Å are expected for bond lengths with the considered GHs [50],[85],[54],[86],[79]. No general and extensive tests on geometries have been carried out (there are only on particular type of systems or selected properties), to the best of our knowledge, for the selected RSH. Therefore, before moving to the analysis of excited-state properties and structures, it is interesting to briefly investigate ground-state optimized structures.
Table 2.4 reports the variations of structural parameters for each molecule with respect to CASPT2 values. In this preliminary analysis on GS structures, only the set of molecules proposed by Page and Olivucci[90] will be considered.

As shown by the data reported in the table, in most cases DFT overestimates ground-state single bond lengths and underestimates double bond lengths with respect to CASPT2, and this holds for all tested molecular systems, with the

Table 2.4: **Computed Bond Length (Å) and Angle (deg) Differences for DFT/6-31+G(d) Ground-State Structures with Respect to CASPT2/6-31G(d)[90] (6-31+G(d) for PAA)**.

	B3LYP	B3P86	PBE0	BMK	BH&HLYP	CAM-B3LYP	CASPT2
				***cis*-Buta-1,3-diene**			
C-C	0.005	-0.001	0.000	0.015	0.000	0.005	1.468
C=C	-0.008	-0.011	-0.011	-0.008	-0.021	-0.016	1.351
C=$\hat{C}$-C	0.6	0.4	0.4	-0.1	0.3	0.2	126.7
				***trans*-Buta-1,3-diene**			
C-C	-0.004	-0.007	-0.008	-0.004	-0.017	-0.012	1.454
C=C	0.004	-0.001	0.000	0.014	0.002	0.006	1.348
C=$\hat{C}$-C	0.7	0.6	0.6	0.2	0.5	0.5	123.6
				Pyrrole			
C-N	0.002	-0.004	-0.006	-0.006	-0.010	-0.004	1.375
C=C	0.001	-0.002	-0.003	0.005	-0.012	-0.006	1.380
C-C	0.007	0.002	0.002	0.013	0.000	0.003	1.420
C-$\hat{N}$-C	-0.132	-0.026	0.024	0.262	-0.189	-0.222	110.0
C=$\hat{C}$-N	0.1	0.1	0.1	0.3	0.3	0.3	107.5
C-$\hat{C}$=C	-0.1	-0.1	-0.2	-0.4	-0.2	-0.1	107.5
				Acrolein			
C=O	-0.008	-0.012	-0.018	-0.026	-0.023	-0.014	1.226
C-C	0.006	0.001	0.006	0.017	0.000	0.010	1.469
C=C	-0.004	-0.007	-0.011	-0.011	-0.016	-0.011	1.345
O=$\hat{C}$-C	0.6	0.7	0.7	0.4	0.5	0.5	123.6
C-$\hat{C}$=C	-0.1	-0.4	0.2	-0.5	-0.2	-0.3	121.1
				Acetone			
C=O	-0.007	-0.010	-0.012	-0.015	-0.021	-0.012	1.226
C-C	0.008	0.001	0.000	0.016	-0.003	0.001	1.511
C-$\hat{C}$=O	-0.1	0.0	0.0	0.0	-0.1	-0.1	121.7
				Diazomethane			
N=N	-0.012	-0.015	-0.017	-0.008	-0.029	-0.019	1.158
C=N	-0.007	-0.011	-0.012	-0.014	-0.017	-0.011	1.302
				Propenoic Acid Anion			
C-O$_{trans}$	-0.007	-0.011	-0.013	-0.018	-0.024	-0.014	1.272
C-O$_{cis}$	-0.006	-0.010	-0.011	-0.016	-0.021	-0.012	1.266
C-C	0.012	0.005	0.006	0.024	0.002	0.007	1.526
C=C	-0.004	-0.007	-0.007	-0.003	-0.016	-0.010	1.343
O-$\hat{C}$-C	0.2	0.1	0.0	-0.1	0.0	0.1	116.8
C-$\hat{C}$=C	0.6	0.1	0.1	0.0	0.2	0.2	124.0
O-$\hat{C}$-O	0.0	0.1	0.2	0.4	0.2	0.0	129.0

exception of *trans*-buta-1,3-diene that shows an opposite behavior.
Percentage errors are around 1-2% for the underestimation of double bonds and around 1% for the overestimation of single ones. In more details, C-C single bonds are accurately estimated by PBE0 and BH&HLYP functionals, BMK yielding (> 1%) too long bonds (deviations between 0.013 and 0.024 $\mathring{A}$). For the other functionals, values are always smaller than 0.017 $\mathring{A}$. The sensitivity of the C=C double bonds to the selected functional is larger, with the best agreement reached by B3LYP calculations (between 0.001 and 0.008 $\mathring{A}$, corresponding to 0.1-0.3% deviations) and the worst one obtained with BHHLYP (from 0.012 and 0.021 Å, 0.9-1.5%).
This tendency to larger variations is observed also for other double bonds; for example, C=O double bonds present a behavior similar to C=C, the optimal description being obtained with B3LYP (0.006-0.008 Å, ca. 0.5%), whereas BMK and BHHLYP errors are close to 2%. The CN bond is described with deviations close to 1%, the best performances being again reached with B3LYP (0.002 Å for PYR and 0.007 Å for DZM) and the worst results still coming from BH&HLYP (0.010 Å for PYR and 0.017 Å for DZM). The DFT-CASPT2 differences for the NN bond of DZM range between 0.7% (BMK) and 2.5% (BHHLYP).
Angles are very well estimated by all functionals with deviations with respect to CASPT2 values systematically smaller than 1% (0.1-0.8°).

From this first analysis, we can conclude that there is a general behavior of DFT functionals to overestimate single bond lengths and underestimate their double counterparts, which means that DFT provides a slightly too localized picture. Let us highlight that this statement holds only for these small molecules. Indeed, in large conjugated systems, such as polyene oligomers, it is well-known that GHs like B3LYP tend to yield (much) too small bond length alternations, and that RSHs or GHs including a large share of HF-X are necessary to restore a more balanced description [95], [96].

In summary, for the systems under scrutiny, the deviations are very small in the GS case, with errors smaller than 0.03 $\mathring{A}$ for bonds and 1° for valence angles. Best (worst) accuracies, in average, are given by B3LYP (BHHLYP). CAM-B3LYP also shows good performances, in many cases close to B3LYP ones.

Vertical Excitation Energies: TD-DFT versus CASPT2

As mentioned in the Introduction, a large number of tests on TD-DFT performances in vertical excitation energies is available in literature. In particular, a

recent extensive benchmark on valence excitations shows that GH containing 20-25% of HF-X gives the best agreements with respect to post-HF results, for relatively small molecules [26].
Indeed, the MAEs for considered functionals range between 0.22 eV (B3LYP, PBE0) and 0.45 eV (BH&HLYP), CAM-B3LYP and BMK showing an intermediate behavior (0.35 eV). Of course, these are mean values, and the actual performance of a functional significantly changes with the considered chromophore[26]. As for the GS geometries, it is therefore interesting to shortly comment on the vertical absorption energies. In Table 2.5, we report the vertical excitation energies for all selected molecules, computed at the corresponding optimized geometries.

There is a general agreement between TD-DFT and CASPT2 results, almost all the functionals showing a MAE $\leq$ 0.3 eV, a deviation not too far from that obtained on a much larger set [26].
Here, however, the lowest difference is obtained by B3P86 and BMK functionals (MAE of 0.21 and 0.22, respectively). In more details, the differences are of the order of 0.2-0.4 eV for CAM-B3LYP and 0.1-0.3 eV BMK functionals in all molecular systems studied, and in the 0.2-0.6 eV range for the other four functionals.

In general, TD-DFT underestimates $n - \pi^*$ excitations and overestimes the $\pi - \pi^*$ ones. The most valuable performances are obtained by BHHLYP (BMK) for $\pi - \pi^*$ excitations and B3P86 for $n - \pi^*$ excitations.
We further note that in the case of our calculation on PSBs, B3LYP is the functional that better performs with respect to CASPT2 data of Valsson and Filippi. In this last case, however, CASPT2 vertical excitations have been calculated using B3LYP/ cc-pVDZ structures [91].

Table 2.5: **Calculated UV Vertical Excitation Energies (eV), Oscillator Strength (in Parentheses), and Symmetry (sym) of Singlet Excited States** [a]

system	sym	B3LYP	B3P86	PBE0	BMK	BH&HLYP	CAM-B3LYP	CASPT2	MV	RSD
cis-buta-1,3-diene	B_2	5.00	5.10	5.10	5.30	5.30	5.20	5.60	5.17	0.02
		(0.31)	(0.32)	(0.31)	(0.31)	(0.32)	(0.31)	(0.22)		
trans-buta-1,3-diene	B_u	5.60	5.70	5.70	5.90	5.90	5.90	6.20	5.78	0.02
		(0.65)	(0.67)	(0.67)	(0.71)	(0.74)	(0.70)	(0.69)		
pyrrole	B_2	6.00	6.30	6.20	6.50	6.30	6.20	6.30	6.25	0.02
		(0.18)	(0.19)	(0.19)	(0.29)	(0.19)	(0.19)	(n.a.)		
acrolein	A″	3.60	3.60	3.70	3.70	4.10	3.80	3.60	3.75	0.05
		(0.00)	(0.00)	(0.00)	(0.00)	(0.00)	(0.00)	(0.00)		
acetone	A_2	4.40	4.40	4.50	4.40	4.70	4.50	4.20	4.48	0.02
		(0.00)	(0.00)	(0.00)	(0.00)	(0.00)	(0.00)	(0.00)		
diazomethane	A_2	2.90	3.00	3.00	2.80	3.00	2.90	2.70	2.93	0.03
		(0.00)	(0.00)	(0.00)	(0.00)	(0.00)	(0.00)	(0.00)		
propenoic acid anion	A″	3.60	3.70	3.80	4.30	4.80	4.30	n.a.	4.08	0.10
		(0.00)	(0.00)	(0.00)	(0.00)	(0.00)	(0.00)			
model B	A′	4.21	4.25	4.29	4.36	4.52	4.31	4.18	4.32	0.02
		(0.64)	(0.64)	(0.65)	(0.67)	(0.74)	(0.70)	(n.a.)		
model C	A′	3.47	3.51	3.54	3.71	3.58	3.60	3.35	3.57	0.02
		(1.01)	(1.01)	(1.04)	(1.15)	(1.07)	(1.09)	(n.a.)		
model D	A′	3.00	3.04	3.06	3.15	3.16	3.12	2.87	3.09	0.02
		(1.35)	(1.36)	(1.38)	(1.43)	(1.49)	(1.44)	(n.a.)		
MAE		0.32	0.26	0.27	0.20	0.32	0.25			

[a] *CASPT2 values are taken from ref [80] for TrBD, PYR, and ACT, from ref [97] for CBD, from refs [98] and [99] for ACR, from ref [100] for DZM, and from ref [91] for PSBs. PAA CASPT2 data are not available (n.a.). Mean values (MV) and relative standard deviations (RSD) are also reported.*

Excited-State Structures and Properties

The most relevant geometrical parameters of the optimized geometries for each of the selected excited states are reported in Tables 2.6 and 2.7. Nomenclature of bonds is referred to ground-state structure. For each molecule, we have optimized the lowest singlet excited state with the exception of PYR, for which the first low-lying $^1B_2$ state has been selected, for the sake of consistency with the reference CASPT2 calculation [90].

Starting with $\pi - \pi^*$ systems, we note that the C-C single bonds in CBD and TrBD are overestimated with respect to the reference CASPT2 values, and this holds for all functionals but BH&HLYP and CAM-B3LYP, which underestimate the bond lengths. PBE0 provides the best agreement, with differences less than 0.002 $\mathring{A}$ ($< 0.2\%$). In general, differences for all functionals are less than 0.012 $\mathring{A}$.

In the case of PSBs, two types of C-C single bonds have to be defined. The first one forms the skeleton of π conjugation, and it is therefore directly involved in the $\pi - \pi^*$ excitation, whereas the second one connects the methyl group.

The two CC single bonds present different behavior: the length of the first is overestimated by low percentage HF-X functional and underestimated by BH&HLYP and CAM-B3LYP, while the second one is underestimated. It is worth noting the different behavior of the C-C single bond connected to the C=NH_2 group: in MDB as in the other previous systems, deviations from CASPT2 are positive for functionals with low HF-X percentage, but in MDC and MDD, such deviations are negative. This can be related to the position of the bond along the chain and the sigma-inductive effect of the methyl group, which is described in opposite manner by BH&HLYP and CAM-B3LYP. In this case, therefore, the oscillating behavior of low percentage HF-X functional (particularly B3LYP) could be linked to the description of excitation closer to an alternation of bonds after excitation where BH&HLYP and CAM-B3LYP describe a picture of this phenomenon closer to CASPT2 view, with a skeleton relaxation but of lower intensity. However, for all the systems, the differences with respect to CASPT2 are less than 0.04 Å for single bonds.

As in the ground state, C=C double bonds are generally underestimated with deviations of ca. 0.001-0.005 Å for both isomers of butadiene and ca. 0.01-0.02 Å for PYR. The only exceptions are the BMK and B3LYP functionals that overestimate the bond distance of TrBD. One can obtain smaller discrepancies by selecting B3LYP (0.001 and 0.003 Å for CBD and TrBD, respectively) or BMK for PYR.

Results for PSB systems are in line with this trend: in general, CC double

Table 2.6: **Computed Bond Length (Å) and Angle (deg) Differences for TD-DFT/6-31+G(d) Excited-State Structures with Respect to CASPT2/6-31G(d) (6-31+G(d) for PAA)[90]**

	B3LYP	B3P86	PBE0	BMK	BH&HLYP	CAM-B3LYP	CASPT2
				***cis*-Buta-1,3-diene**			
C-C	0.008	0.003	0.002	0.007	-0.008	-0.003	1.398
C=C	-0.001	-0.003	-0.004	0.005	-0.010	-0.005	1.421
C=$\hat{C}$-C	-0.2	-0.6	-0.5	-0.6	-0.5	-0.5	122.0
				***trans*-Buta-1,3-diene**			
C-C	0.005	0.002	0.000	0.006	-0.012	-0.006	1.399
C=C	0.003	0.001	0.000	0.010	-0.005	-0.001	1.421
C=$\hat{C}$-C	0.4	0.4	0.3	0.1	0.3	0.2	124.1
				Pyrrole			
C-N	-0.022	-0.019	-0.029	-0.014	-0.033	-0.025	1.416
C=C	-0.011	-0.012	-0.015	0.000	-0.019	-0.013	1.461
C-C	-0.001	-0.004	-0.005	0.001	-0.012	-0.008	1.370
C-$\hat{N}$-C	-1.4	-1.3	-1.3	-1.5	-5.8	-1.4	107.3
C=$\hat{C}$-N	0.4	0.1	0.3	0.1	0.4	0.4	108.1
C-$\hat{C}$=C	-0.2	-0.2	-0.3	-0.3	-0.2	-0.2	108.2
				Acrolein			
C=O	-0.052	-0.059	-0.061	-0.061	-0.065	-0.056	1.277
C-C	0.008	0.004	0.008	0.036	0.028	0.027	1.429
C=C	-0.005	-0.008	-0.013	-0.022	-0.040	-0.032	1.350
O=$\hat{C}$-C	5.3	6.0	5.5	2.5	1.8	2.6	125.4
C-$\hat{C}$=C	0.5	0.4	0.6	0.5	1.0	0.8	122.5
				Acetone			
C=O	-0.037	-0.043	-0.048	-0.064	-0.071	-0.053	1.368
C-C	0.008	0.001	0.002	0.027	0.010	0.010	1.489
C-$\hat{C}$=O	0.8	0.8	1.0	1.5	1.6	1.1	117.0
				Diazomethane			
N=N	-0.010	-0.013	-0.014	0.012	-0.012	-0.011	1.215
C=N	-0.022	-0.025	-0.030	-0.042	-0.053	-0.036	1.327
				Propenoic Acid Anion			
C-O$_{trans}$	0.021	0.014	0.014	0.016	0.015	0.016	1.272
C-O$_{cis}$	-0.099	-0.104	-0.106	-0.106	-0.111	-0.100	1.394
C-C	0.023	0.018	0.016	0.017	0.000	0.006	1.401
C=C	0.006	0.004	0.001	0.004	-0.018	-0.009	1.409
O-$\hat{C}$-C	8.9	9.1	9.0	8.8	9.0	8.0	117.3
C-$\hat{C}$=C	-1.6	-1.9	-1.8	-1.6	-0.8	-1.9	126.7
O-$\hat{C}$-O	-4.4	-4.7	-4.7	-4.6	-4.4v -4.3	111.8	

Table 2.7: **Computed Bond Length (Å) and Angle (deg) Differences for TD-DFT/6-31+G(d) Excited-State Structures of cis-Retinal Model with Respect to CASPT2/cc-pVDZ [91]**

	B3LYP	B3P86	PBE0	BMK	BH&HLYP	CAM-B3LYP	CASPT2
				Model B C_s			
N=C	-0.021	-0.026	-0.027	-0.025	-0.031	-0.024	1.367
C_1-C_2	0.037	0.029	0.022	0.017	-0.011	-0.001	1.447
C_2=C_3	-0.056	-0.057	-0.050	-0.026	-0.028	-0.027	1.432
C_3-C_4	0.030	0.024	0.016	0.012	-0.012	-0.003	1.430
C_4=C_5	-0.012	-0.015	-0.015	-0.006	-0.016	-0.015	1.396
C-methyl	-0.009	-0.016	-0.016	0.001	-0.012	-0.011	1.499
N-$\hat{C}_1$-CH_3	0.7	0.7	0.6	0.3	0.1	0.2	117.6
C_3-$\hat{C}_4$-C_5	2.4	2.3	2.1	1.2	1.4	1.4	121.1
				Model C C_s			
N=C	-0.016	-0.021	-0.019	-0.019	-0.025	-0.019	1.352
C_1-C_2	0.003	-0.003	-0.018	-0.003	-0.021	-0.018	1.422
C_2=C_3	-0.036	-0.037	-0.013	-0.012	-0.019	-0.013	1.419
C_3-C_4	0.041	0.031	-0.013	0.008	-0.021	-0.013	1.455
C_4=C_5	-0.033	-0.035	-0.011	-0.008	-0.013	-0.011	1.408
C_5-C_6	0.016	0.011	-0.006	0.008	-0.012	-0.006	1.432
C_6=C_7	-0.01	-0.01	-0.02	-0.01	-0.02	-0.02	1.382
C-methyl	-0.01	-0.01	-0.01	0.00	-0.01	-0.01	1.506
N-$\hat{C}_1$-C_2	0.4	0.5	1.0	0.6	1.2	1.0	121.9
C_5-$\hat{C}_6$-C_7	2.1	2.0	1.1	1.0	1.2	1.1	120.0
				Model D C_s			
N=C	-0.015	-0.020	-0.022	-0.018	-0.024	-0.018	1.352
C_1-C_2	0.001	-0.004	-0.006	-0.003	-0.021	-0.017	1.413
C_2=C_3	-0.027	-0.030	-0.026	-0.008	-0.016	-0.010	1.414
C_3-C_4	0.029	0.020	0.013	0.003	-0.023	-0.018	1.454
C_4=C_5	-0.041	-0.042	-0.036	-0.013	-0.016	-0.012	1.403
C_5-C_6	0.032	0.024	0.017	0.008	-0.015	-0.010	1.431
C_6=C_7	-0.026	-0.028	-0.024	-0.009	-0.017	-0.013	1.397
C_7-C_8	0.011	0.006	0.004	0.009	-0.008	-0.002	1.428
C_8=C_9	-0.008	-0.012	-0.012	-0.008	-0.021	-0.018	1.375
C-methyl	-0.005	-0.013	-0.013	0.003	-0.011	-0.008	1.507
N-$\hat{C}_1$-C_2	0.3	0.3	0.4	0.5	0.9	0.9	122.5
C_7-$\hat{C}_8$-C_9	2.0	1.8	1.6	1.0	1.1	1.0	121.8

bonds are underestimated, with deviations from CASPT2 around or lower than 0.04 Å, if we exclude the case of the $C_1$3=$C_1$4 bond in MDB where 20% of HF-X gives values around 0.05 Å. In all cases, increasing the HF-X percentage gives values closer to CASPT2; however, the performances are not improved by changing the correlation description. The best agreement is obtained using BMK functional (differences around 0.006-0.026 Å).
The CN bond length of PYR is underestimated with deviations presenting the same sign, but slightly larger amplitude than for the ground state. Once again, the best agreement is obtained with BMK (0.014 Å). In the case of PBS systems, however, values closer to CASPT2 are obtained at the B3LYP level for which errors less than 0.02 Å are found. All functionals underestimate the C=$\hat{C}$-C angle in CBD and PYR by values ranging between 0.2-0.6° and 0.2-0.3°, for CBD and PYR, respectively. Conversely, in the case of TrBD, the angle is overestimated by 0.1-0.4°. The overestimation is shown also in the case of the three PSB systems but with larger values, in function of the position of the bond along the chain.

Concerning the $\pi - \pi^*$ systems, as for the previous case, TD-DFT CC single bonds are systematically too long with respect to CASPT2, and two different trends that depend on the HF-X contribution can be outlined. Indeed, for ACR and ACT systems, increasing the HF-X contribution induces larger differences (between 0.001 and 0.036 Å) with respect to CASPT2, whereas the opposite behavior is found for PAA, for which the closest agreement is obtained with BH&HLYP. The length of the C=C double bond tends to be underestimated for all systems with the exception of PAA with the B3LYP, B3P86, PBE0, and BMK functionals, for which the overestimation is very small (values are very close to CASPT2). The C=O distance is underestimated by about 0.06 Å for both ACR and ACT. This behavior is also found for the CO_{cis} bond in PAA (0.1 Å underestimation) that presents an enhanced double bond character as compared to the ground state, especially in comparison with the trans analogue. In fact, this bond is shorter than the "*trans*" CO bond at the ground state and longer at the excited state. This interpretation in terms of changes in the double bond character is also supported by the comparison of the angles C-$\hat{C}$=O and C-$\hat{C}$-O_{cis} that have similar behavior (see below).
N=N and C=N bond lengths are both underestimated by all the six functionals, with differences larger than 0.010 Å for the former and between 0.02 and 0.05 Å for the latter, the most accurate estimate being obtained with B3LYP. The C-$\hat{C}$=C angle is overestimated in ACR (ca. 0.4°) and underestimated in PAA (ca. 2°), whereas the C-$\hat{C}$=O angle is overestimated for the three molecules (ca. 2-5°, 0.8-1°, and 9° for ACR, ACT, and PAA, respectively), including the PAA if we assume that the bond C-O_{cis} presents the double bond

character. Finally, The O-$\hat{C}$=O angle in PAA is understated by about 4°.

Table 2.8 collects the mean absolute differences (MADs) and relative standard deviations (RSD) of excited-state structural parameters, varying either the system or the functional studied. The first analysis provides insights regarding the general tendency of TD-DFT in reproducing CASPT2 data, whereas the second type of analysis indicates which type of functional shows a more reproducible behavior in estimating the bond type regardless of the selected systems.

Table 2.8: **Mean Absolute Differences (MAD) with Respect to CASPT2 Values and Corresponding Relative Standard Deviation (RSD) of Excited-State Bond Lengths (Å), Averaged on Systems Studied**

	B3LYP	B3P86	PBE0	BMK	BH&HLYP	CAM-B3LYP
				MAD		
C-C	0.015	0.013	0.010	0.009	0.014	0.010
C=C	0.020	0.021	0.017	0.010	0.018	0.014
C=O	0.063	0.069	0.072	0.077	0.082	0.070
C=N	0.032	0.034	0.033	0.032	0.038	0.031
				RSD		
C-C	0.84	0.77	0.61	0.97	0.47	0.68
C=C	0.83	0.78	0.78	0.68	0.43	0.55
C=O	0.42	0.38	0.35	0.27	0.25	0.31
C=N	0.15	0.13	0.18	0.41	0.31	0.27

From the RSD values reported in the table, we can argue that for CC single and double bonds there is a great dispersion of data in changing system, with the values between 0.97 and 0.47 for single bonds and between 0.43 and 0.83 for double bonds. In contrast, lower data dispersion and absolute differences are found for the C=O (in the range 0.25-0.42 for all functionals) and C=N bond lengths (0.13-0.27), which, therefore, represent a more reproducible geometrical parameter. However, it is worth noting that C=O bonds are presents only for $n - \pi^*$ systems.
In analysing MAD values, we can quantify the effects of changing HF-X percentage or correlation functional. CC single and double bonds are, in the average, better described increasing HF-X percentage, and also passing from LYP

to P86 and PBE correlation description. Smaller MAD values are obtained with CAM-B3LYP and BMK, which, however, gives higher RSD. For C=N bonds, the impacts of both HF-X percentage and correlation are negligible, as the MAD values are very similar for all functionals except for BH&HLYP, which undergoes a larger discrepancy. In the case of C=O, the best agreement is obtained with B3LYP, which, however, yields larger dispersion of data. Also, in this case, a good compromise between precision and accuracy is reached with the CAM-B3LYP functional. Finally, we can conclude that all functionals give, on average, reproducible results for excited-state geometries in comparison to CASPT2, with CAM-B3LYP showing the best performances.

More insights about the description of the entire excitation process by the different functionals could be obtained by comparing the mean bond length variations (BLV) upon excitation for four selected bonds, reported in Figure 2.10.

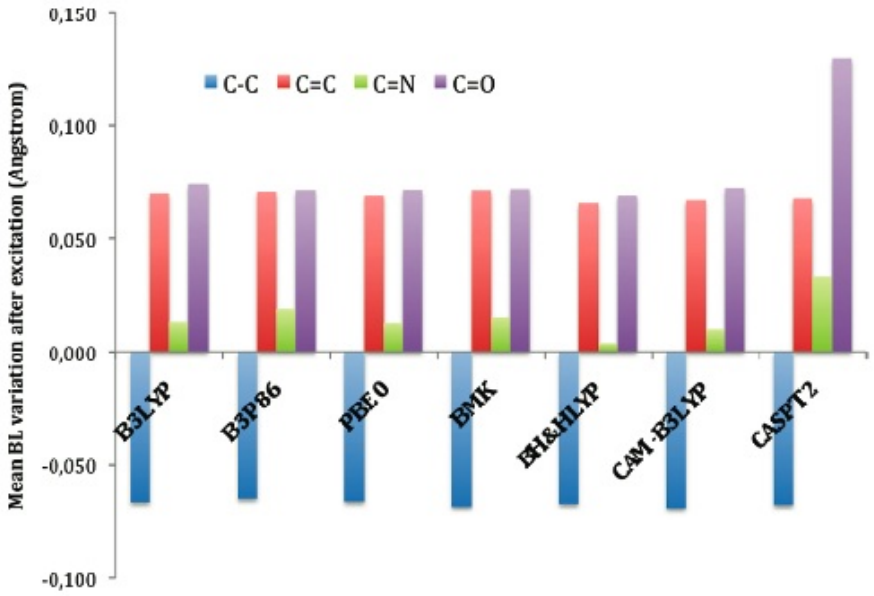

Figure 2.10: Computed TD-DFT and CASPT2 absolute bond length variations upon excitations.

As it clearly appears, CC single and double bond variations are well reproduced by all the functionals, the PBE0 approach providing the smallest deviations (< 0.005 Å) for both bonds. In contrast, the changes for the C=O bonds are significantly underestimated by all functionals, with errors about

0.06 Å. Here, B3LYP gives slightly smaller errors than PBE0. Finally, CN bond variations are also systematically underestimated at the TD-DFT level, but this effect remains trifling.

To conclude the analysis on excited-state geometries, we report a further comparison between DFT and CASPT2, but this time focused on the description of conjugation in extended $\pi - \pi^*$ systems here represented by the PBSs. Such an analysis is performed in terms of the bond length alternation (BLA) defined as the difference of the average of single and double carbon-carbon bonds along the $\pi - \pi^*$ chain. The results obtained with the different functionals and the reference CASPT2 description are reported in Figure 2.11.

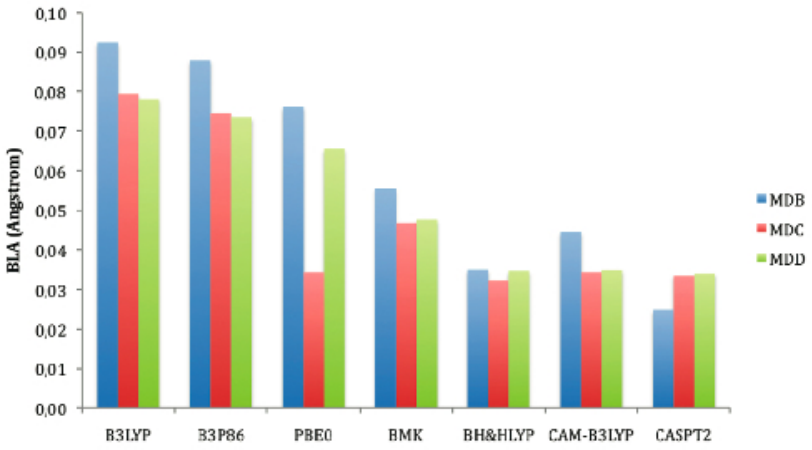

Figure 2.11: Bond length alternation (BLA) of excited-state structures of PBS systems.

As it is shown in Figure 2.11, the increase of HF-X percentage gives a description of the physics of the system closer to the CASPT2, with the long-range corrected scheme giving the best agreement for the longer systems. This is indeed an interesting result, as it shows that CAM-B3LYP is the most "robust" functional (among the ones investigated here) in consistently describing the changes in the conjugation with the spatial extent 46 and is compatible with the CASPT2 picture of relaxation pathways 40.

Finally, in Tables 2.9 and 2.10 we report a comparison of dipole moment variations, that is, the difference between excited- and ground-state dipole moments, and emission energies as obtained with the different functionals. As

CASPT2 data are not available for these quantities, the comparison is limited to TD-DFT data only.

As it can be seen from Table 2.9, all functionals describe dipole moment variations in a qualitatively good agreement with what is expected from the nature of the excitation. In fact, with all the functionals we obtain negative variations (i.e., decrease of the dipole) for $n - \pi^*$ systems (ACR and ACT) and positive variations (increase of the dipole) for $\pi - \pi^*$ (CBD). Of course, due to symmetry reasons, TrBD has null dipole in both electronic states. We note that even if pyrrole is a $\pi - \pi^*$ system, it is also an example of so-called five-membered six π-electron aromatic ring molecules in which the heteroatom (here nitrogen) donates two π electrons and each of the four carbon atoms supplies one π-electron. In this case, the excitation leads to a decrease of the dipole instead of an increase as in standard $\pi - \pi^*$ systems.
For a parallel reason, also $n-\pi^*$ diazomethane presents a specific behavior with a positive instead of a negative variation as for standard $n - \pi^*$ systems. Going into more details, some differences appear among the different functionals, with BMK and B3LYP giving the smallest and highest variations, respectively (only for ACT and DZM, CAM-B3LYP gives larger variations than B3LYP). It is worth noting that a general decrease of the module of dipole moment variation with increasing the percentage of HF-X is found even if the trend is not completely monotonic going from B3LYP to BH&HLYP.

Emission energies, reported in Table 2.10, show a large dispersion with functionals for $n - \pi^*$ systems (especially ACR and PAA), while for $\pi - \pi^*$ systems the differences are quite small. As for dipole moment variations, no clear proportionality or dependence with HF-X percentage can be found. It is interesting to note that dispersion on emission when compared to excitation (last columns in Tables 2.5 and 2.10) is almost unchanged, except in the case of ACR and PAA, where RSD values are double.

From the above analysis, one clear trend common to all molecular systems, types of excitation, and atoms involved emerges: TD-DFT has a tendency to underestimate the length of double bonds as compared to CASPT2 and therefore to exaggerate the double bond character of the relaxed excited state. Clearly, the extent of this trend depends on the character of excitation, with the CO bonds directly involved in the $n - \pi^*$ transition being largely affected. Indeed, TD-DFT gives a more localized description of this transition than do post-HF approaches.

Table 2.9: **Dipole Moment Variations (Debye) between Excited and Ground States**

system	B3LYP	B3P86	PBE0	BMK	BH&HLYP	CAM-B3LYP	MV	SD
cis-buta-1,3-diene	1.03	0.91	0.96	0.78	0.93	0.98	0.93	0.08
pyrrole	-1.47	-1.14	-1.39	-0.90	-1.37	-1.31	-1.26	0.19
acrolein	-2.40	-2.41	-2.35	-2.35	-2.37	-2.45	-2.39	0.04
acetone	-1.07	-1.08	-1.13	-1.11	-1.32	-1.13	-1.14	0.08
diazomethane	1.41	1.39	1.45	1.47	1.62	1.59	1.49	0.09

Table 2.10: **Emission Energies (eV) at Optimized Structures of Excited States Studied**

system	B3LYP	B3P86	PBE0	BMK	BH&HLYP	CAM-B3LYP	MV	RSD
cis-buta-1,3-diene	4.13	4.20	4.21	4.25	4.20	4.19	4.20	0.01
trans-buta-1,3-diene	4.93	5.02	5.03	5.09	5.06	5.04	5.03	0.01
pyrrole	5.54	5.68	5.69	6.16	5.69	5.64	5.73	0.04
acrolein	2.84	2.83	3.66	3.12	3.51	3.25	3.20	0.10
acetone	3.65	3.69	3.74	3.75	4.11	3.81	3.79	0.05
diazomethane	2.52	2.57	2.56	2.23	2.42	2.46	2.46	0.05
propenoic acid anion	1.49	1.46	1.59	1.98	2.49	2.09	1.85	0.20
MDB	3.91	3.97	4.02	4.08	4.20	4.08	4.04	0.02
MDC	3.27	3.32	3.37	3.54	3.43	3.43	3.39	0.03
MDD	2.79	2.84	2.90	3.08	2.98	2.99	2.93	0.03

Chapter 3

TD-DFT/PCM schemes for molecular excited states in solvent

3.1 Introduction

This chapter focuses on concepts and applications of theoretical and computational models for the calculation of excitation energies of molecules in solution. A new computational strategy is proposed after an analysis of the currently available methods.
The development of accurate but still computationally feasible strategies in modeling excited state of molecules in solution is a challenging task due to the complexity of the problem in which the processes of formation and relaxation of the electronic states have to be coupled with the dynamics of the solvent molecules [101],[102],[103]. As a consequence, the definition of the excited states of molecular solutes also requires the characterization of the solvent degrees of freedom that are composite in nature and very large in number.
A very well-known example of such a coupling is the distinction between "nonequilibrium" and "equilibrium" solvation regimes following an electronic transition in the solute. The differences in the characteristic response time of the various degrees of freedom of the solvent, in fact, may lead to a solvation regime in which the slow components (i.e., those arising from molecular translations and rotations) are not equilibrated with the excited-state electronic redistribution upon vertical excitation. The resulting nonequilibrium regime will then relax into a new equilibrium in which the solvent is allowed to completely equilibrate, i.e., to reorganize all its degrees of freedom including the slow ones. Especially for highly polar solvents, these two different regimes can

influence the properties of the solute excited states in very different ways.

Equilibrium versus nonequilibrium is just one of the specific issues that have to be properly accounted for in the complex task of the definition of realistic and accurate models for the description of structure and properties of excited states in solution[104][105]. In addition, the necessity of a proper description of different electronic states implies a quantum-mechanical (QM) description. These requirements, together with the generally medium-to-large dimensions of the molecular systems of real interest in this field, are difficult to satisfy when the effect of the environment is also to be included. As a result of this combination of complex aspects, the largest part of the models proposed in the literature introduces a focused approach, i.e., a more accurate description of the molecular system of interest (the chromophore, possibly including small portions of the environment) and a less accurate description of the remainder. There are different formulations of the focused approach; the most common ones are the hybrid QM/molecular mechanics (QM/MM) [106], [107] and the continuum solvation models [108], [109], [110] .
Both of them use a classical description for the environment but, whereas in the former the microscopic nature of the solvent molecules is maintained, in the latter a macroscopic dielectric is used. The different philosophy beyond the two classes of methods leads to important differences in both the physical and the computational aspects of their applications, as well as in their range of applicability. The methods based on explicit representations of the environment yield information on specific configurations of the environment around the chromophore, whereas the continuum models give only an averaged picture of it. On the other hand, QM/MM requires many more calculations than continuum models to obtain a correct statistical description. This much larger computational cost of QM/MM is particularly disadvantageous in the study of excited states, as the QM level required is generally quite expensive even for a single calculation on an isolated system; thus, the necessity to repeat the calculation many times makes the approach very expensive (or even not feasible). For this reason, most of the QM/MM calculations on excited states make use of semiempirical QM methods [111], [112], [113], [114], [115].
On the contrary, the level of the QM description can be any when continuum models are used, as the additional cost with respect to gas-phase calculations remains very limited. In addition, continuum solvation models include effects of mutual polarization between the solute and the environment (also those due to a possible nonequilibrium solvation), whereas standard QM/MM methods are based on nonpolarizable force fields. As a matter of fact, QM/MM approaches including environment polarization have been proposed and also

applied to the study of excited states of solvated systems [116], [117], [118], [119]. However, among the available approaches, the most popular for this kind of study is still represented by continuum solvation model [110].
In particular, the polarizable continuum model (PCM) [109] has been shown to give a reliable description of different phenomena involving electronically excited states. PCM is in fact a very general continuum model, which has been extended to many different QM levels as well as to QM methods to evaluate energy derivatives with respect to many different perturbations. These extensions have made PCM applicable to calculate geometries and properties of various electronic states as well as to study processes and spectroscopies involving both ground and excited states.
Here, after a short introduction to the PCM model and the quantum problem associated, different strategies to calculate excited states energies and properties of solvated systems are presented. The same strategies are applied to the study of solvent effects on push-pull chromophores [120] and to the analysis of the role played by intramolecular charge transfers [121]. In the last part of the chapter a new developed strategy to study vertical excitations in solution is presented and discussed togheter with some preliminary numerical applications.

3.2 Short review of the Polarizable Continuum Model (PCM)

The definition of the PCM model goes through two steps [109],[110]:

- treatment of the electrostatic problem [1].
- formalization of the problem in a quantum mechanical framework.

From a classical point of view, we can formulate the problem of a molecule in solution as a charge density ρ_M, due to both point charges and a continuous density, inside a cavity C of proper shape and dimension, within a continuous polarizable medium (the dielectric characterized by the electric permittivity ϵ). Such a system is described by the Poisson equation [122] :

$$-\vec{\nabla} \cdot [\epsilon(\mathbf{r})\vec{\nabla} \cdot \vec{V}(\mathbf{r})] = 4\pi\rho_M(\mathbf{r}) \tag{3.1}$$

[1] other terms, such as cavitation, repulsion and dispersion forces will not consider in this brief review of the method because not strictly necessary to introduce the quantities we need to follow next paragraphs.

Setting a boundary condition that the potential vanishes at infinity, the solution of 3.1 is unique as it is unique, with the same boundary conditions, the potential V_M generated in vacuum by ρ_M, namely the solution of

$$-\nabla^2 V_M(r) = 4\pi\rho_M(r)$$

We can therefore define a reaction potential as:

$$V_R = V - V_M$$

which can be interpreted as the electrostatic potential due to the polarization of the dielectric. Since

$$\epsilon(r) = \begin{cases} 0 & r \in C \\ \epsilon & r \notin C \end{cases}$$

the following differential equations are obtained for V, V_M and V_R :

$$\begin{cases} -\nabla^2 V = 4\pi\rho_M, & r \in C \\ -\nabla^2 V = 0, & r \notin C \\ \lim\limits_{r\to 0} V(r) = 0 \end{cases} \qquad \begin{cases} -\nabla^2 V_M = 4\pi\rho_M, & r \in C \\ -\nabla^2 V_M = 0, & r \notin C \\ \lim\limits_{r\to 0} V_M(r) = 0 \end{cases}$$

$$\begin{cases} -\nabla^2 V_R = 0 & r \in C \\ -\nabla^2 V_R = 0 & r \notin C \\ \lim\limits_{r\to 0} V_R(r) = 0 \end{cases} \tag{3.2}$$

Equations 3.2 are accompaniend by a set of boundary conditions on the cavity surface Γ:

$$\begin{cases} [V] = 0 & \text{on } \Gamma \\ [\partial V] = 0 & \text{on } \Gamma \end{cases} \tag{3.3}$$

The first jump condition 3.3 expresses the continuity of the potential across the surface, whereas the second one involves the continuity of the component of the field (expressed as the gradient of V) that is perpendicular to the cavity surface:

$$[\partial V] = \left(\frac{\partial V}{\partial \vec{n}}\right)_{in} - \epsilon \left(\frac{\partial V}{\partial \vec{n}}\right)_{out} = 0 \tag{3.4}$$

Where $\vec{n}$ is the outward-pointing vector perpendicular to the cavity surface.

Equations (3.2) and (3.3) are the basic elements to use in the elaboration of solvation methods according to standard electrostatics. Among the possible approaches to solve the electrostatic problem we use here the so called apparent surface charge (ASC) approach, where an apparent surface charge density $\sigma(\vec{s})$[2] spread on the cavity surface Γ [123]. The ASC defines a potential over the whole space:

$$V_\sigma(\vec{r}) = \int_\Gamma \frac{\sigma(\vec{s})}{|\vec{r} - \vec{s}|} d^2 s \tag{3.5}$$

This potential is exactly the reaction potential V_R of eq. (3.2). Despite the reduction of the source of the reaction potential to a charge distribution limited to a close surface, the integration of eq.(3.5) over a surface of complex shape is computationally challenging. The solutions are generally based on a discretization of the integral into a finite number of elements. This technique may be profitably linked to the boundary element method (BEM) [124], a numerical technique widely used in physics and engeneering to solve complex differential equations.
The cavity surface Γ is approximated in terms of a set of finite elements (called *tesserae*) small enough to consider $\sigma(\vec{s})$ almost constant within each tessera (with corresponding area A_k). Therefore:

$$V_\sigma(\vec{r}) \approx \sum_k^{Nts} \frac{\sigma(\vec{s}_k) A_k}{|\vec{r} - \vec{s}_k|} = \sum_k^{Nts} \frac{q_k}{|\vec{r} - \vec{s}_k|} \tag{3.6}$$

Where the q_ks are the point charges in terms of the local value of $\sigma(\vec{s}_k)$ on each tessera. The local value of the potential necessary to define q_k also depends on the whole set of the surface charges, and so the correct values of the surface charges, and the correct expression of the reaction potential, are to be obtained through an iterative procedure. In the years various definitions of $\sigma(\vec{s}_k)$, and consequently of q_k, have been proposed. These have led tho the different formulations of the method known as DPCM [123], IEFPCM [125],[126] and CPCM [127]. Here we do not present the details for each formulation of PCM, referring the interested reader to the large literature (see for instance ref. [109],[110] and references therein), but we focus only on the common features of all the methods.
Once the cavity surface has been partitioned in tesserae the electrostatic equation for $\sigma(\vec{s})$ within the various PCM formulation can be rewritten as a set of NTs (number of tesserae) coupled equations, wich can be recast in a matrix

[2] $\vec{s}$ is the position variable over the surface Γ of the cavity C.

Table 3.1: **Matrices of the various PCM versions of BEM equations (3.7)** [109]

PCM version	$\mathbf{Q}$	$\mathbf{f_M}$
DPCM	$\left(2\pi\frac{\epsilon+1}{\epsilon-1}\mathbf{A}^{-1}-\mathbf{D}^{*}\right)^{-1}$	$\mathbf{E}_M^{\perp}$
CPCM	$\mathbf{S}^{-1}$	$\mathbf{V}_M$
IEFPCM	$\left[\left(2\pi\frac{\epsilon+1}{\epsilon-1}\mathbf{A}^{-1}-\mathbf{D}^{*}\right)\mathbf{S}\right]^{-1}\left(2\pi\mathbf{A}^{-1}-\mathbf{D}\right)$	$\mathbf{V}_M$

form of the type [109]

$$\mathbf{q} = -\mathbf{Q}\mathbf{f_M} \tag{3.7}$$

where $\mathbf{Q}$ is a square matrix NTs $\times$ NTs collecting cavity geometrical factors (the tesserae representative points $\vec{s}_k$ and the corresponding areas) and the dielectric constant of the medium; $\mathbf{q}$ and $\mathbf{f_M}$ are column matrices, the first containing the unknown charges and the second the values of the proper electrostatic quantity, namely, the normal component of the solute electric field $E_M^{\perp}$ or the solute electrostatic potential V_M, calculated at the tesserae.
The expression of $\mathbf{Q}$ and $\mathbf{f}_M$ for the various versions of PCM are reported in Table 3.2. In the table, the matrix $\mathbf{A}$ is the diagonal matrix of tesserae areas, whereas the matrices $\mathbf{S}$ and $\mathbf{D}$ take the form:

$$\begin{cases} S_{ii} &= 1.0694\sqrt{\frac{4\pi}{a_i}} \\ S_{ij} &= \frac{1}{|\vec{s}_i-\vec{s}_j|} \end{cases} \tag{3.8}$$

$$\begin{cases} D_{ii} &= -\left(2\pi+\sum_{j\neq i} D_{ij}a_j\right)\frac{1}{a_i} \\ D_{ij} &= \frac{(\vec{s}_i-\vec{s}_j)\cdot\hat{\mathbf{n}}_j}{|\vec{s}_i-\vec{s}_j|^3} \end{cases} \tag{3.9}$$

where a_i is the area of tessera i.

QM approach to PCM

If now we want to translate the PCM equations in a quantum mechanical language, we have to introduce an effective Hamiltonian for the solute-solvent system [109]:

$$\hat{H}_{eff} = \hat{H}_M^0 + \hat{V}^{int} \tag{3.10}$$

where $\hat{H}_M^0$ is the Hamiltonian od the solute (i.e. the focused part M of the model) and $\hat{V}^{int}$ (i.e. the solvent reaction potential) is the solute-solvent interaction term. Assumed valid the Born-Oppenheimer (BO) approximation, The charge distribution is conveniently divided into electronic and nuclear components

$$\rho_M(r) = \rho_M^e(r) + \rho_M^N(r) \tag{3.11}$$

In the BO framework, the QM procedure does not affect the nuclear component. The operator $\hat{V}^{int}$ can be divided into four terms that are similar to the zero-,one- and two-electron type components of the solute Hamiltonian. By defining the solute-solvent interaction energy as [110]:

$$U^{int} = \int_C V_\sigma(r)\rho_M(r)dr^3 \tag{3.12}$$

and considering that the interaction potential has, as sources, the two components of ρ_M, and thus it is composed of two terms, one stemming from the electronic charge distribution of the solute M and one from its nuclear charge distribution, we obtain:

$$U^{int} = U^{e-e} + U^{N-e} + U^{e-N} + U^{N-N} \tag{3.13}$$

where U^{x-y} corresponds to the interaction energy between the component of the interaction potential having as source $\rho_M^x(r)$, namely $\hat{V}^{int,x}$ and the charge distribution $\rho_M^y(r)$. Some considerations:

- U^{e-N} is formally identical to U^{N-e}, and both correspond to one-electron operators.
- U^{N-N} not contribute to electronic part of $\hat{H}_{eff}$, and in the BO approximation, is a constant term.

- U^{e-e} describes the interaction between electronic charge distributions and therefore correspond to a bi-electronic term.

In a variational framework the resulting Schrödinger equation is

$$\hat{H}_{eff}|\Psi\rangle = E|\Psi\rangle \tag{3.14}$$

obtained by minimizing an appropriate functional.
The functional to minimize, for a PCM solvated system, is the free energy functional [109]:

$$\mathcal{G} = \langle\Psi|\hat{H}^0 + \hat{V}_\sigma|\Psi\rangle - \frac{1}{2}\langle\Psi|\hat{V}_\sigma|\Psi\rangle \tag{3.15}$$

the Eq. (3.15) takes in account the irreversible work done to polarize the dielectric [128]. If we now apply a self-consistent field (SCF) approach to solve eq.(3.14), such as Hartree-Fock (HF) or Kohn-Sham (KS), the minimization of $\mathcal{G}$ with respect to variation of $|\Psi\rangle$ gives the following Fock operator:

$$\hat{F} = \hat{F}_0 + \hat{V}_\sigma \tag{3.16}$$

where $\hat{F}_0$ is the Fock (or KS) operator of the isolated molecule, including one-electron Hamiltonian, Coulomb and (scaled) exchange terms, and possibly the exchange-correlation potential, namely, on the basis of molecular orbitals, it can be expressed as

$$F^0_{pq} = h_{pq} + \sum_{i\tau'} \delta_{\tau\tau'} \left[\langle pi\tau|qi\tau'\rangle - C_{HF}\langle pi\tau|iq\tau'\rangle\right] + V^{xc}_{pq\tau} \tag{3.17}$$

where C_{HF} is the coefficient of the HF-exchange in the hybrid functional scheme, and

$$\hat{V}_\sigma = \sum_{k=1}^{Nts} \hat{V}_k q_k \qquad \text{where} \qquad \hat{V}_k = -\frac{1}{|r - s_k|} \tag{3.18}$$

The point charges q_k are obtained by resolution of the iterative PCM problem. We will focus on the IEF version of the model, for which:

$$q_k = \sum_{l=1}^{Nts} Q_{kl} V_l \qquad k, l \to s_k, s_l \tag{3.19}$$

where V_l are the expectation values (including nuclear contributions) of the electrostatic potential operator computed on the surface element s_l:

$$V_l = V_l^e + V_l^{Nuc} = -\sum_i^{occ} \int \phi_i^*(r)\phi_i(r)\frac{1}{|r-s_l|}dr + \int \rho^{Nuc}(r)\frac{1}{|r-s_l|}dr \quad (3.20)$$

Once the formalism has been introduced, we can write down the Eq. 3.15 for the ground state (GS) wave function as:

$$\begin{aligned} \mathcal{G}_{GS} &= \langle \Psi_{GS}|\hat{H^0} + \hat{V_\sigma}|\Psi_{GS}\rangle - \frac{1}{2}\langle \Psi_{GS}|\hat{V_\sigma}|\Psi_{GS}\rangle \\ &= E^{GS} - \frac{1}{2}\sum_k V_k^{GS} q_k^{GS} \end{aligned} \quad (3.21)$$

3.3 Theory for solute excited states in solvent

Time dependent processes embrace a large variety of phenomena, which span an impressive range of time scales (from 10^{-15} s for linear and nonlinear spectroscopy to 10^{-2} s for diffusion-controlled reactions in diluite acqueous solutions). The responses of the microscopic particles (molecules, atoms, electrons) of the solvent required to reach a certain equilibrium value of the polarization have specific characteristic times (CT). When the solute charge distribution varies appreciably within a period of the same order as these characteristic times, the solvent response will not be sufficiently rapid to build up a new equilibrium polarization, and the actual value of the polarization will lag behind the changing charge distribution. The actual polarization $\vec{P}(t)$ is determined by the Maxwell field in the medium not only at time t but also at a previous time t', in a form expressed by the integral [129],[130]

$$\vec{P}(t) = \int_{-\infty}^{t} dt' G(t-t')\vec{E}(t') \quad (3.22)$$

where the kernel $G(t-t')$ is the solvent response function and $\vec{E}(t')$ the Maxwell field. Transforming the convolution integral to the Fourier frequency space we obtain [131]

$$\vec{P}(\omega) = \frac{\hat{\epsilon}(\omega-1)}{4\pi}\vec{E}(\omega) \quad (3.23)$$

where $\hat{\epsilon}(\omega)$ is the complex dielectric permettivity

$$\hat{\epsilon}(\omega) = \epsilon'(\omega) - i\epsilon''(\omega) \tag{3.24}$$

The real part $\epsilon'(\omega)$ is the frequency-dependent dielectric constant, describing the component of the polarization density in phase with the oscillating field while the complex part, or loss factor, $\epsilon''(\omega)$ determines the component of the polarization with a phase difference of $\pi/2$ with respect to the Maxwell field, giving rise to the loss of energy of the electric field in the medium.
The explanation of the correspondence in the behavior of all polar compounds in an electromagnetic field is found in the fact that the electric polarization is built up of three parts, the orientational, the nuclear, and the electronic polarization, each part corresponding to motions of a different kind of particle (molecules, atoms, electrons, respectively) with different CTs. As the frequency increases, the so-called nonequilibrium effects appear subsequently in the different contributions of the polarization. Orientational contributions (CT below 10^{-12} s) will first start to lag behind the variations of the electromagnetic field; next, nuclei (CT around 10^{-14} s) will not be able to follow the field, and finally, at very high frequencies, electrons (CT around 10^{-16} s) also will lag behind the electromagnetic field.

Historically, in continuum models large use has been made of the approximation according to which it is sufficient to decompose the polarization into two terms. Within this approximation, the polarization vector $\vec{P}(t)$ becomes:

$$\vec{P}(t) \approx \vec{P}^{fast}(t) + \vec{P}^{slow}(t) \tag{3.25}$$

where fast indicates the part of the solvent response that always follows the dynamics of the process and slow refers to the remaining inertial term. Such partition in the medium response gives rise to the so called "nonequilibrium" regime. Obviously, what is fast and what is slow depends on the specific dynamic phenomenon under study. In a very fast process such as the vertical transition leading to a change of the solute electronic state via photon absorption or emission, $\vec{P}^{fast}$ can be reduced to the term related to the response of the solvent electrons, whereas $\vec{P}^{slow}$ collects all of the other terms related to the various nuclear degrees of freedom of the solvent molecule. The operative partition of the total polarization can be performed using two alternative, but equivalent, schemes. In the Marcus scheme [132] (partition I)

$$\vec{P}^A = \vec{P}^E_{or} + \vec{P}^A_{el} \tag{3.26}$$

where superscripts E and A refer to the "early" (or initial) and the "actual" time in relation to the chronological order of the transition process. In this partition, the previous slow and fast indices are replaced by the subscripts *or* and *el* referring to "orientational" and "electronic" polarization response of the solvent, respectively.

In the Pekar scheme [133], which we shall indicate as partition II, eq. (3.3) has to be rewritten as

$$\vec{P}^A = \vec{P}^E_{in} + \vec{P}^A_{dyn} \tag{3.27}$$

where the subscripts *in* and *dyn* refer now to an "inertial" and a "dynamic" polarization response of the solvent, respectively. The differences between the two schemes are related to the fact that, in partition I, the division into slow and fast contributions is done in terms of physical degrees of freedom (namely, those of the solvent nuclei and those of the solvent electrons), whereas in partition II, the concept of dynamic and inertial response is exploited. This formal difference is reflected in the operative equations determining the two contributions to $\vec{P}$ as, in II, the slow term ($\vec{P}_{in}$) includes not only the contributions due to the slow degrees of freedom but also the part of the fast component that is in equilibrium with the slow polarization, whereas, in I, the latter component is contained in the fast term $\vec{P}_{el}$.
It is important to stress that the two schemes I and II differ in the form of the slow and fast components of the polarization, but they are practically and physically equivalent (in the limit of a linear response regime) in the sense that they give the same value of the total reaction potential and, thus, the same effects on the solute as well as the same interaction energies [134]. The use of one partition instead of the other is dictated only by the requirements of the specific computational code in which the model is implemented.

3.3.1 PCM-Linear Response and State Specific approach in solvent

The free energy expression given in Eq. (3.21) for a ground state can be generalized to both an equilibrium and a non-equilibrium excited state K [135]. In the first case we assume that the solvent reaction field has had time to completely relax from the initial ground state value determining $\hat{V}_\sigma(GS)$ to the final value representing a new solute-solvent equilibrium and determining

$\hat{V}_\sigma(K)$. By contrast, in the nonequilibrium regime, the solvent reaction field is represented by a Franck-Condon type term, sum of an electronic (or dynamic) contribution $\hat{V}_\sigma^{\,dyn}(K)$ in equilibrium with the excited state K and an orientational (or inertial) part still frozen in the initial ground state value, $\hat{V}_\sigma^{\,in}(GS)$. The expressions of the free energies corresponding to each regime are described here below.

Equilibrium

We are looking for an expression of the free energy that is as more similar as possible in both equilibrium and non equilibrium cases. For this reason we define an *excited state energy in equilibrium with a ground-state solvent reaction field* $E_{GS}^{K,eq}$:

$$\begin{aligned} E_{GS}^{K,eq} &= \langle\Psi_{eq}^K|\hat{H}^0 + \hat{V}_\sigma^{\,GS}|\Psi_{eq}^K\rangle = \\ &= \langle\Psi_{eq}^K|\hat{H}^0|\Psi_{eq}^K\rangle + \sum_l^{Nts}\langle\Psi_{eq}^K|\hat{V}_l q_l^{GS}|\Psi_{eq}^K\rangle \\ &= \langle\Psi_{eq}^K|\hat{H}^0|\Psi_{eq}^K\rangle + \sum_l^{Nts} V_l^K q_l^{GS} \end{aligned} \tag{3.28}$$

In Eq.(3.28) we use the definition in Eq.(3.18) of the PCM reaction field operator and the charges q_l^{GS} are calculated by Eq.(3.19):

$$q_l^{GS} = \sum_{m=1}^{Nts} Q_{lm} V_m^{GS} = \sum_{m=1}^{Nts} Q_{lm}\langle\Psi^{GS}|\hat{V}_m|\Psi^{GS}\rangle \tag{3.29}$$

We can use the expression for $E_{GS}^{K,eq}$ to calculate the excited state equilibrium free energy:

$$\begin{aligned} \mathcal{G}_K^{eq} &= \langle\Psi_{eq}^K|\hat{H}^0 + \frac{1}{2}\hat{V}_\sigma^{\,K}|\Psi_{eq}^K\rangle = \\ &= \langle\Psi_{eq}^K|\hat{H}^0|\Psi_{eq}^K\rangle + \langle\Psi_{eq}^K|\hat{V}_\sigma^{\,GS}|\Psi_{eq}^K\rangle - \langle\Psi_{eq}^K|\hat{V}_\sigma^{\,GS}|\Psi_{eq}^K\rangle + \frac{1}{2}\langle\Psi_{eq}^K|\hat{V}_\sigma^{\,K}|\Psi_{eq}^K\rangle \\ &= E_{GS}^{K,eq} - \sum_l^{Nts} V_l^K q_l^{GS} + \frac{1}{2}\sum_l^{Nts} V_l^K q_l^K \end{aligned} \tag{3.30}$$

If we now introduce a partition of the excited state density matrix as:

$$\mathbf{P}^K = \mathbf{P}^{GS} + \mathbf{P}^{\Delta} \tag{3.31}$$

We can also partition V_l^K and q_l^K:

$$\begin{cases} V_l^K = V_l^{GS} + V_l^{\Delta} \\ q_l^K = q_l^{GS} + q_l^{\Delta} \end{cases} \tag{3.32}$$

The Eq.(3.30) can now be written down as:

$$\begin{aligned} \mathcal{G}_K^{eq} &= E_{GS}^{K,eq} - \frac{1}{2}\sum_l^{Nts}\left[V_l^{GS} + V_l^{\Delta}\right] q_l^{GS} + \frac{1}{2}\sum_l^{Nts} V_l^{GS} q_l^{\Delta} + \frac{1}{2}\sum_l^{Nts} V_l^{\Delta} q_l^{\Delta} \\ &= E_{GS}^{K,eq} - \frac{1}{2}\sum_l^{Nts} V_l^{GS} q_l^{GS} + \frac{1}{2}\sum_l^{Nts} V_l^{\Delta} q_l^{\Delta} \end{aligned} \tag{3.33}$$

The last line of Eq.(3.33) is our work equation, where we make the approximation[3]

$$V_l^{GS} q_l^{\Delta} = V_l^{\Delta} q_l^{GS} \tag{3.34}$$

Nonequilibrium

As in the equilibrium case, we define a nonequilibrium excited state energy in the presence of the ground state reaction field, $E_{GS}^{K,neq}$:

$$\begin{aligned} E_{GS}^{K,neq} &= \langle \Psi_{neq}^K | \hat{H}^0 + \hat{V}_\sigma^{\,GS} | \Psi_{neq}^K \rangle \\ &= \langle \Psi_{neq}^K | \hat{H}^0 | \Psi_{neq}^K \rangle + \sum_l^{Nts} V_l^{K,neq} \left[q_l^{GS,in} + q_l^{GS,dyn} \right] \end{aligned} \tag{3.35}$$

In Eq.(3.35) we have introduced the partition of GS charges q_l^{GS} in dynamic and inertial parts. For a generic state M:

$$\begin{aligned} q_l^M &= \sum_f^{Nts} Q_{fl}(\epsilon) V_f^M \\ q_l^{M,dyn} &= \sum_f^{Nts} Q_{fl}(\epsilon_\infty) V_f^M \\ q_l^{M,in} &= q_l^M - q_l^{M,dyn} \end{aligned} \tag{3.36}$$

[3]This approximation is introduced here as it allows a more compact notation; we note, however, that in the computational code both formulations have been implemented and that numerical tests have shown an almost exact equivalence. We also remark that in the limit of an exact solution of the electrostatic problem, Eq.(3.34) is exactly fulfilled.

where ϵ_∞ represent the optical dielectric constant of the solvent. For the Ψ^K_{neq} state, eq. (3.36) becomes:

$$\begin{aligned} q_l^{K,in} = \qquad q_l^{GS,in} = \qquad & \textstyle\sum_f Q_{fl}(\epsilon) V_l^{GS} - \sum_f Q_{fl}(\epsilon_\infty) V_l^{GS} \\ q_l^{K,dyn} = \textstyle\sum_f Q_{fl}(\epsilon_\infty) V_l^{K} = \quad & \textstyle\sum_f Q_{fl}(\epsilon_\infty) V_l^{GS} + \sum_f Q_{fl}(\epsilon_\infty) V_l^{\Delta neq,e} \end{aligned} \tag{3.37}$$

In Eq.(3.37) the term $V_l^{\Delta neq,e}$ is associated to the partition of the density matrix given in Eq.(3.31).

The free energy for the Ψ^K_{neq} state therefore becomes:

$$\begin{aligned} \mathcal{G}_K^{neq} &= \langle \Psi_K^{neq} | \hat{H}_0 + \hat{V}_\sigma^{\,GS,in} + \hat{V}_\sigma^{\,K,dyn} | \Psi_K^{neq} \rangle \\ &\quad -\tfrac{1}{2} \langle \Psi_{GS} | \hat{V}_\sigma^{\,GS,in} | \Psi_{GS} \rangle - \tfrac{1}{2} \langle \Psi_K^{neq} | \hat{V}_\sigma^{\,K,dyn} | \Psi_K^{neq} \rangle \\ &= E_{GS}^{K,neq} + \textstyle\sum_l^{Nts} V_l^{K,neq} q_l^{\Delta,dyn} \\ &\quad -\tfrac{1}{2} \textstyle\sum_l^{Nts} V_l^{GS} q_l^{GS,in} - \tfrac{1}{2} \sum_l^{Nts} V_l^{K,neq} q_l^{K,dyn} \\ &= E_{GS}^{K,neq} \\ &\quad -\tfrac{1}{2} \textstyle\sum_l^{Nts} \left[V_l^{GS} q_l^{GS,dyn} + V_l^{\Delta,neq} q_l^{\Delta neq,dyn} \right] \\ &\quad + \textstyle\sum_l^{Nts} V_l^{\Delta,neq} q_l^{GS,dyn} - \tfrac{1}{2} V_l^{GS} q_l^{GS,in} \end{aligned} \tag{3.38}$$

where we have made use of Eq.(3.37).
The expression for $\mathcal{G}_K^{neq}$ can be simplified if once again we assume that

$$V_l^{GS} q_l^{\Delta neq,dyn} = V_l^{\Delta,neq} q_l^{GS,dyn}$$

and therefore

$$\mathcal{G}_K^{neq} = E_{GS}^{K,neq} - \frac{1}{2} \sum_l^{Nts} V_l^{GS} q_l^{GS} + \frac{1}{2} \sum_l^{Nts} V_l^{\Delta,neq} q_l^{\Delta neq,dyn} \tag{3.39}$$

The vertical transition energy to the excited state K is obtained by subtracting the ground state free energy $\mathcal{G}_{GS}$ of Eq(3.21) from $\mathcal{G}_K^{eq}$ and $\mathcal{G}_K^{neq}$ of Eq.(3.33) and Eq.(3.39):

$$\omega_K^{eq} = \mathcal{G}_K^{eq} - \mathcal{G}_{GS} = \Delta E_{GS}^{K0,eq} + \frac{1}{2} \sum_l^{Nts} V_l^{\Delta} q_l^{\Delta,dyn} \tag{3.40}$$

$$\omega_K^{neq} = \mathcal{G}_K^{neq} - \mathcal{G}_{GS} = \Delta E_{GS}^{K0,neq} + \frac{1}{2} \sum_l^{Nts} V_l^{\Delta,neq} q_l^{\Delta neq,dyn} \tag{3.41}$$

These equations show that vertical excitations in solvated systems are obtained as a sum of two terms, the difference between excited- and ground-state energies in the presence of a frozen ground-state solvent ($\Delta E_{GS}^{K0,neq}$) and a relaxation term, which is determined by the mutual polarization of the solute and the solvent after excitation. The latter term is obtained by taking into account the dynamic and inertial partition of the solvent response.

The requirement needed to incorporate the solvent effects into a state-specific method is fulfilled by using the effective Hamiltonian $\hat{H}_{eff}$ defined in eq. 3.10. The only specificity to take into account is that, to calculate $\hat{V}_\sigma$, the density matrix of the electronic state of interest has to be known. Such a nonlinear character of $\hat{V}_\sigma$ is generally solved through an iterative procedure: at each iteration the solvent-induced component of the effective Hamiltonian is computed by exploiting eq. (3.5), with the apparent charges determined from the standard ASC equation with the first-order density matrix of the preceding step. At each iteration n, the free energy of the state K is obtained as

$$\mathcal{G}_K^n = \langle \Psi_K^n | \hat{H}_M^0 | \Psi_K^n \rangle + \frac{1}{2} \sum_i \langle \Psi_K^n | \hat{V}_\sigma [\Psi_K^{n-1}] | \Psi_K^n \rangle \tag{3.42}$$

where the solvent operator $\hat{V}_\sigma[\Psi_K^{n-1}]$ has been obtained using the solute electronic density calculated with the wave function of the previous iteration. At convergence Ψ_K^{n-1} and Ψ_K^n must be the same and eq.(3.42) gives the correct free energy of the state K. We note that this procedure is valid only for states fully equilibrated with the solvent. A nonequilibrium formulation requires a two-step calculation:

1 An equilibrium calculation for the initial electronic state (either ground or excited), from which the slow (or inertial) apparent charges, q_{in}, are obtained and stored for the successive calculation on the final state.

2 A nonequilibrium calculation performed with the interaction potential $\hat{V}_\sigma$ composed of two components, $\hat{V}_\sigma = \hat{V}_{fixed} + \hat{V}_{change}$, where $\hat{V}_{fixed}$ is constant due to the fixed q_{in} of the previous calculation, and $\hat{V}_{change}$ changes during the iteration procedure[4].

In contrast, the alternative LR approach is solved in a single step calculation for the whole spectrum of the excited states of interest, similarly to what

[4]It is defined in terms of the fast (or dynamic) charges q_{dyn} as obtained from the charge distribution of the solute final state.

done for isolated systems, as show in chapter 2. The form of the LR-PCM problem [136],[137] is the same of LR-KS:

$$\begin{bmatrix} \mathbf{A} & \mathbf{B} \\ \mathbf{B}^* & \mathbf{A}^* \end{bmatrix} \begin{bmatrix} \mathbf{X} \\ \mathbf{Y} \end{bmatrix} = \omega \begin{bmatrix} \mathbf{1} & \mathbf{0} \\ \mathbf{0} & -\mathbf{1} \end{bmatrix} \begin{bmatrix} \mathbf{X} \\ \mathbf{Y} \end{bmatrix} \tag{3.43}$$

Within this formalism, $\mathbf{A}$ and $\mathbf{B}$ collect the Hessian components of the free energy functional $\mathcal{G}$ with respect to the wave function variational parameters [5]:

$$\begin{aligned} A_{ia\sigma,jb\tau} &= \delta_{ij}\delta_{ab}\delta_{\sigma\tau}(\epsilon_a - \epsilon_b) + \langle i_\sigma j_\tau | a_\sigma b_\tau \rangle - C_{HF}\delta_{\sigma\tau}\langle i_\sigma a_\sigma | j_\tau b_\tau \rangle \\ &\quad + (1 - C_{HF})\langle i_\sigma j_\tau | f_{xc} | a_\sigma b_\tau \rangle + \mathcal{V}^{PCM}_{ai,bj} \end{aligned} \tag{3.44}$$

$$\begin{aligned} B_{ia\sigma,jb\tau} &= \langle i_\sigma b_\tau | a_\sigma j_\tau \rangle - C_{HF}\delta_{\sigma\tau}\langle i_\sigma a_\sigma | b_\tau j_\tau \rangle \\ &\quad + (1 - C_{HF})\langle i_\sigma b_\tau | f_{xc} | a_\sigma j_\tau \rangle + \mathcal{V}^{PCM}_{ai,jb} \end{aligned} \tag{3.45}$$

In the definitions (3.44) and (3.45) the effect of the solvent acts in two ways: indirectly, by modifying the molecular orbitals and the corresponding orbital energies (they are in fact solutions of the Fock equations including solvent reaction terms); explicitly, through the perturbation term $\mathcal{V}^{PCM}_{ai,jb}$.
This term can be described as the electrostatic interaction between the charge distribution $\phi^*_a\phi_i$ and the dynamic contribution to the solvent reaction potential induced by the charge distribution $\phi^*_b\phi_j$, and it can be written in terms of the vector product between the electrostatic potential and the induced apparent fast charges, determined by the corresponding transition density charge, namely

$$\mathcal{V}^{PCM}_{ai,bj} = \sum_k V_{ai}(\vec{s}_k) q^{dyn}_{bj} \tag{3.46}$$

It is now possible to meaningfully compare the excitation energies obtained with the explicit determination of the excited state wave functions and those given by the LR theory. By comparing the PCM term reported in eq. (3.41) with the one reported in eq. (3.46), we note that they are formally and physically different; the former depends on the electrostatic potential and PCM

[5] the same notation of chapter 2 relating to TD-DFT methods is adopted.

charges calculated using the change of the density matrix $\mathbf{P}^{\Delta}$ of the excited state, whereas in the latter the same quantities have been obtained by using transition matrix elements.
The difference between the two approaches can be clarified by interpreting the excitation in solution as a two-step process: in the first step, the molecule that was in its ground state in equilibrium with the solvent is excited to the state K in the presence of a solvent polarization frozen to the value proper for the solute ground state. The energy change related to this process, ($\Delta E_{GS}^{K0,neq}$), is equally described by the two theories. In the second step of the excitation process, the fast degrees of freedom of the solvent rearrange to equilibrate with the charge density of the solute excited state; in this step the two theories diverge because the energy variation accompanying this relaxation is not explicitly accounted for in the LR framework. On the contrary, the LR accounts for a correction which, being originated by the dynamic solute-solvent interactions, might be classified as a part of dispersion [135],[138].

3.3.2 The corrected-Linear Response (cLR)

In eq. (3.33) (or equivalently in eq. 3.41 for the nonequilibrium regime) we have shown that excited-state free energies can be obtained by calculating the frozen-PCM energy E_{GS}^{K} and the relaxation term of the density matrix, $\mathbf{P}^{\Delta}$ (or $\mathbf{P}_{neq}^{\Delta}$), where the calculation of the relaxed density matrices requires the solution of a nonlinear problem being the solvent reaction field dependent on such densities.
If we introduce a perturbative scheme and we limit ourselves to the first order, an approximate but effective way to obtain such quantities is represented by the LR scheme as shown in the following equations. Using a LR scheme, in fact, we can obtain an estimate of $\Delta E_{GS}^{K0,neq}$, which represents the difference between the excited- and ground-state energies in the presence of a frozen ground-state solvent as the eigenvalue (ω_K^0) of a non-Hermitian eigensystem of type (3.43), where $\mathcal{V}_{ai\sigma,bj\sigma'}^{PCM} = 0$ but the orbitals and the corresponding orbital energies used to build the $\mathbf{A}$ and $\mathbf{B}$ matrices have been obtained by solving the SCF equation in the presence of a ground-state solvent.

$$\begin{cases} \mathcal{V}^{PCM}_{ai\sigma,bj\sigma'} = 0 \\ \varepsilon_{p\sigma} \longrightarrow \varepsilon^{PCM}_{p\sigma} \\ |\Psi_{GS}\rangle \longrightarrow |\Psi^{PCM}_{GS}\rangle \\ \phi_i \longrightarrow \phi^{PCM}_i \\ \omega_K \longrightarrow \omega^0_K \end{cases} \tag{3.47}$$

By using this approximation, the equilibrium and nonequilibrium free energies for the excited state K become:

$$\mathcal{G}^{eq}_K = \mathcal{G}_{GS} + \omega^0_K + \frac{1}{2}\sum_l^{Nts} V_l(\mathbf{P}^{\Delta}) q_l^{\Delta,dyn} \tag{3.48}$$

$$\mathcal{G}^{neq}_K = \mathcal{G}_{GS} + \omega^0_K + \frac{1}{2}\sum_l^{Nts} V_l(\mathbf{P}^{\Delta,neq}) q_l^{\Delta neq,dyn} \tag{3.49}$$

The only unknown term of eqs (3.48) and (3.49) is the relaxation part of the density matrix, $\mathbf{P}^{\Delta}$ (or $\mathbf{P}^{\Delta,neq}$) (and the corresponding apparent charges). These quantities can be obtained through the extension of LR approaches to analytical energy gradients (see next section). In these extensions the so-called Z-vector [27] (or relaxed-density) approach is used; as shown in the next section, this approach allows a computationally efficient implementation of the post-HF and TD-DFT analytical gradients. The solution of the Z-vector equation as well as the knowledge of eigenvectors $|X_K, Y_K\rangle$ of the TD-DFT linear system allow one to calculate $\mathbf{P}^{\Delta}$ for each state K (as in eq. (2.88). Once $\mathbf{P}^{\Delta}$ is known we can calculate the corresponding apparent charges as

$$q_l^{\Delta,x} = \sum_m^{Nts} Q_{ml}(\epsilon_x) V_m^{\Delta_x} \tag{3.50}$$

$$\begin{cases} \epsilon_x = \epsilon \\ \mathbf{P}^{\Delta,x} = \mathbf{P}^{\Delta} \\ q_l^{\Delta,x} = q_l^{\Delta} \end{cases} \quad \text{equilibrium regime} \tag{3.51}$$

$$\begin{cases} \epsilon_x = \epsilon_\infty \\ \mathbf{P}^{\Delta,x} = \mathbf{P}^{\Delta neq} \\ q_l^{\Delta,x} = q_l^{\Delta dyn} \end{cases} \quad \text{non-equilibrium regime} \tag{3.52}$$

By introducing the TD-DFT relaxed density and the corresponding charges (3.50) into Eqs. (3.48) and (3.49) we obtain the first-order approximation to the exact free energy of the excited state by using a linear response scheme. This is the current *corrected linear response* (cLR) approach [139], implemented by solving twice the TD-DFT equations:

a) First, the explicit solvent contribution is left out from such equations and thus the ω_K^0 excitation energies are computed.

b) Then these solutions are used as a guess to solve the TD-DFT equations again, but this time the explicit solvent contribution is included and the corresponding relaxed density is computed and used as detailed above.

To have a qualitative estimate of the changes in excitation energies one obtains moving from LR to cLR approach, we can adopt the simple diagnostic index formulated in ref. [139] using a first-order perturbation theory for a simplified system (a dipole at the center of a spherical cavity). Such an index correlates the correction of the SS and LR approaches with respect to the frozen-solvent transition energy ω_K^0 with state and transition dipoles, namely

$$\delta = \frac{\omega_K^0 - \omega_K^{LR}}{\omega_K^0 - \omega_K^{SS}} = \frac{2\mu_{0K}^2}{\Delta\mu_{0K}^2} \tag{3.53}$$

where $\Delta\mu_{0K}$ is the difference between the ground- and excited state K dipole moment and μ_{0K} is the corresponding transition dipole.
Obviously, we cannot expect that such a relation based on a spherical cavity and a dipolar coupling between the solute and the reaction field is exactly fulfilled by the PCM values but it is reasonable to suppose that the correlation with $\Delta\mu_{0K}$ and μ_{0K} is maintained. By doing that, we can predict the differences between LR and cLR transition energies for some typical excitations (namely $n \rightarrow \pi^*$, $\pi \rightarrow \pi^*$ and charge transfer) from the graph reported in Figure 3.1.

As it can be seen from the graph, the largest differences are found for transitions in which the difference between the dipole change and the transition dipole is large; in particular, ω_K^{cLR} will be significantly smaller (larger) than ω_K^{LR} if $\Delta\mu_{0K}^2$ is much larger (smaller) than $2\mu_{0K}^2$. These two extreme situations typically apply to $n \rightarrow \pi^*$ and charge-transfer transitions, respectively.

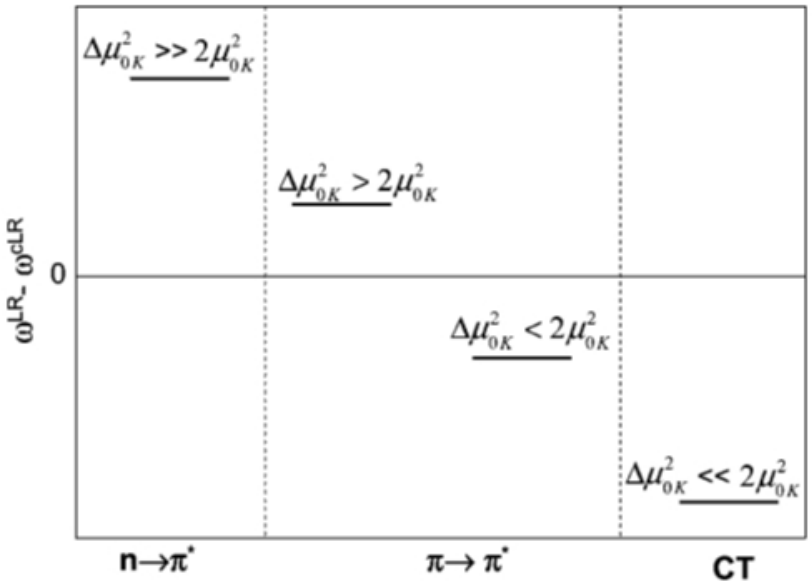

Figure 3.1: Graphical representation of a qualitative comparison between LR and cLR for some common excitations.

Finally, it is worth to note that, even if here it is interesting to emphasize possible differences between the two approaches, it is also important to note that the solvatochromic contribution related to the inertial response of the solvent (i.e., that determining ω_K^0) is described in the same way. With such a contribution being the main part of relative solvatochromic shifts, we can expect that in all cases cLR and the LR approaches will give very similar descriptions of the solvent effect and, in particular, of the relative shift passing from one solvent to the other.

Concluding this section, it is worth noticing that a different procedure of *state specific* type, based on a different philosophy, was presented by Improta et al [140]. They propose an alternative effective approach to the solution of the nonlinear problem of determining the polarization charges corresponding to excited state density based on a self-consistent procedure, which iterates on the total density: i.e. both $\mathbf{P}^{GS}$ and $\mathbf{P}^{\Delta}$ are modified.

3.3.3 Analytical Gradients of the Excited State Energy.

Once we have described the extension of PCM to LR approaches to evaluate excitation energies, the natural following step is to generalize it to the analyt-

ical derivatives with respect to specific perturbations. In this way, in fact, we can extend the study of excited states to their relaxed geometries and properties. The evaluation of analytical derivatives of the PCM-TD-DFT excitation energy ω_K with respect to a generic parameter (e.g., a nuclear coordinate) has been proposed by Scalmani et al. [141], as a generalization of the analogous derivative for the PCM-CIS excitation energies [142]. The starting point is the definition of the gradient of the excitation energies ω, wich are solution of eq. (3.43); this gradient does not require any derivative of the excitation amplitudes (i.e., the eigenvectors) because ω has been variationally determined, but it requires the changes in the elements of the Fock matrix. These, in turn, require the knowledge of the MO coefficients derivatives, which are the solution of the couple perturbed Kohn-Sham equations (CPKS).
It has been shown that there is no need to solve the CPKS equations for each perturbation, but rather only for one degree of freedom, which represents the orbital relaxation contribution to the one-particle density matrices (1PDM) involved in all post-SCF gradient expressions (see section 2.5). In the resulting equation, the occupied-occupied and virtual-virtual blocks of the $\mathbf{P}^{\Delta}$ matrix are already available from the diagonalization of (3.43), whereas the occupied-virtual block is the unknown (as in eq. 3.31). The final form of the gradient of the excitation energy is conveniently expressed in the AO basis as

$$\omega^{\xi} = \sum_{\mu\nu} h^{\xi}_{\mu\nu} P^{\Delta}_{\mu\nu} + \sum_{\mu\nu} S^{\xi}_{\mu\nu} W_{\mu\nu} + \sum_{\mu\nu\kappa\lambda} \langle \mu\kappa|\nu\lambda\rangle^{\xi} \Gamma_{\mu\nu,\kappa\lambda} + \omega^{XC,\xi} + \omega^{PCM,\xi} \quad (3.54)$$

where we have used $\mu, \nu...$ to indicate atomic basis functions, $\Gamma_{\mu\nu,\kappa\lambda}$ to indicate the two-particle density matrix (2PDM), which collects all the contributions that multiply the integral first derivatives $\langle \mu\kappa|\nu\lambda\rangle^{\xi}$, and $W_{\mu\nu}$ to indicate the energy weighted density matrix.
Here $h^{\xi}_{\mu\nu}$ and $S^{\xi}_{\mu\nu}$ are the derivatives of the one electron Hamiltonian and the overlap matrix, respectively, and $\omega^{XC,\xi}$, is a derivative of exchange-correlation contributions.
All the details of the derivation of this expression can be found in the reference paper, here it is useful to focus on the PCM parts only. Equation 3.54 includes two explicit PCM contributions:

$$\omega^{PCM,\xi} = \sum_{\mu\nu} V^{PCM(\xi)}_{\mu\nu} P^{\Delta}_{\mu\nu} + \sum_{\mu\nu\kappa\lambda} \mathcal{V}^{PCM(\xi)}_{\mu\nu,\kappa\lambda} (X+Y)_{\mu\nu} (X+Y)_{\kappa\lambda} \quad (3.55)$$

even if the solvent reaction field also implicitly affects eq. (3.54) through $\mathbf{P}^{\Delta}$ and $\mathbf{W}$. The first explicit PCM contribution is common to all post-SCF gradients and it involves the change in the 1PDM made by the post-SCF procedure:

$$\sum_{\mu\nu} V_{\mu\nu}^{PCM(\xi)} P_{\mu\nu}^{\Delta} = \sum_{\mu\nu} P_{\mu\nu}^{\Delta} \left[\sum_{k} V_{\mu\nu,k}^{E} q_k^w \right] \tag{3.56}$$

Equation 3.54 can be finally summed to the standard DFT contribution to give the expression for the total free energy gradient of each state in the presence of the solvent,

$$\mathcal{G}^{TD-DFT,\xi} = \mathcal{G}_{GS}^{DFT,\xi} + \omega^{\xi} \tag{3.57}$$

where $\mathcal{G}_{GS}^{DFT,\xi}$, is the ground-state DFT gradient contribution (see ref 29). This procedure can be used to obtaine excited-state relaxed geometries and emission energies by applying the nonequilibrium description, but this time in a reversed order (i.e., an equilibrated excited state and a nonequilibrium, or vertical, ground state).

3.4 Applications of PCM-LR and PCM-cLR schemes to push-pull chromophores

In this section we report a TD-DFT/PCM study of the structure and properties of the low-lying, intramolecular charge-transfer singlet electronic state of two push-pull chromophores that possess an electron-donating group and an electron-accepting group connected by a conjugated π system, namely julolidinemalononitrile (JM) and indolinedimethine-malononitrile (IDMN). Both JM and IDMN have been deeply studied by Myers-Kelley and co-workers using UV and resonance Raman (RR) spectroscopies [143], [144], [145]. JM has been further analysed with computational studies by our group [146] and by Guthmuller and Champagne [147]; in both studies a PCM description was introduced to include solvent effects. Here, a comparative analysis of the two systems is presented; such an analysis will start from the suggestions of the two previous papers [146], [147] (namely the need of including solvent effects and the importance of a correct QM description), but it will proceed further by applying the PCM tools described in the previous sections of this chapter. In such a way, the nature of the excited state of interest will be deeply analysed in terms of both structural and electronic aspects.

3.4.1 Computational Details.

The calculations were performed at the DFT level by using the 6-311G(d,p) basis set. As suggested by a previous paper on JM [147], the effect of HF exchange has been addressed by considering B3LYP, B3LYP-35, and BH&HLYP hybrid functionals. Although both B3LYP and BH&HLYP are commonly used functionals [50],[47] this is not the case for B3LYP-35, which is a Becke three parameter hybrid type functional constructed by the following expression:

$$0.65E_X^{Slater} + (1 - 0.65)E_X^{HF} + 0.585E_X^{Becke} + E_C^{VWN} + 0.81E_C^{LYP} \qquad (3.58)$$

In comparison, for the B3LYP functional the values are 0.8, 0.72, and 0.81, respectively (see section 2.2). The use of these functionals has been motivated by the expected significant dependence of the excited state geometries and properties on the amount of Hartree-Fock exchange in the functional (B3LYP, BH&HLYP, and B3LYP- 35 contain 20%, 50%, and 35% of Hartree-Fock exchange, respectively). In addition, the CAM-B3LYP functional [63] (19% exact exchange at short-range, like a conventional hybrid, but 65% at long-range) has been used to test the reliability of DFT hybrid functionals against a proper description of charge-transfer electronic transitions. Solvent effects were

described by exploiting the IEF-PCM with a molecule-shaped cavity made of interlocking spheres centered on heavy atoms: the default set of sphere radii (UA0) implemented in the Gaussian code [78] was exploited. Vertical excitation energies were obtained in the nonequilibrium solvation regime, by exploiting both the linear response (LR) and the corrected LR (cLR) schemes as described before. Excited-state geometries and properties were obtained applying the TD-DFT gradients implementation to all four functionals (see section 3.3.3). Resonance Raman spectra in solution were obtained by exploiting the extension of IEFPCM to STD approach [146]. All QM calculations were performed using a development version of the Gaussian package [78] whereas the vibronic structure of absorption spectra was simulated by exploiting the FCfast code [148],[149].

3.4.2 Results and Discussion

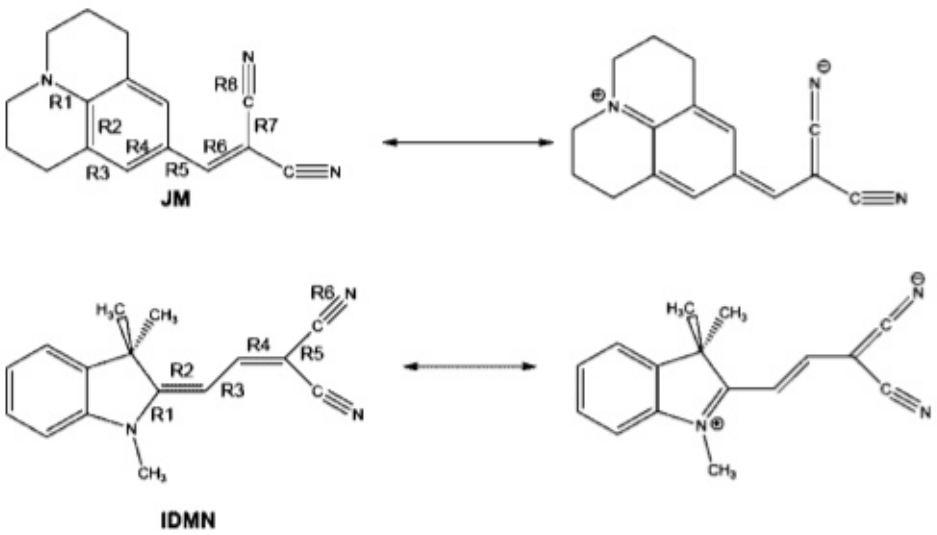

Figure 3.2: Structure of julolidine-malononitrile (JM) and indolinedimethine-malononitrile (IDMN) in terms of the two resonance forms. The indication of selected bond distances is also given

Before moving to the study of excitation and excited-state geometries and properties, let us focus on ground-state geometry and electronic charge distribution. A key geometrical parameter useful to rationalize the behavior of push-pull systems is the bond length alternation (BLA) index [150]; such an index, which is defined as the difference between the average length of the carbon-carbon single and double bonds, has been widely used in the literature

focusing on the structure and properties of push-pull systems (see, e.g., ref. [151],[152] and [153]). By definition, a positive BLA value is associated to the neutral form, a negative value to the zwitterionic form and a zero value to a delocalized system (see Figure 3.2): In Figure 3.3 the variations of BLA for IDMN and JM moving from cyclohexane to acetonitrile are reported, as obtained by using the four DFT functionals. The values reported are qualitatively consistent with a two state model, pictorially represented in Figure 3.2. More specifically, as the solvent polarity increases, the ground state displays a more zwitterion-like structure: with increasing solvent polarity and increasing zwitterionic character, we observe alternate positive and negative variations of the single and of the double bond lengths along the whole skeleton going from the amino to the cyano nitrogen. The expected solvent dependence of the conjugated bond lengths is easily deduced by inspection of the resonance forms in Figure 3.2. This behavior is almost identical at each DFT level of description.

In more detail, as can be seen from the inspection of Figure 3.3, an increase in the BLA index is noticed by increasing the HF exchange percentage in the DFT functional, i.e., going from B3LYP to B3LYP-35, BHandHLYP, and CAM-B3LYP. Such a behavior is common both to cyclohexane and to acetonitrile. A greater HF exchange percentage yields more localized single and double bonds. Despite this common behavior of BLA, the two chromophores show a different response to the solvent. IDMN is described as a neutral structure in the ground state in both solvents with an increasing delocalization of charge in the polar solvent, as expected. This is not the case of JM that is described as more delocalized than IDMN as shown by the small BLA values (for B3LYP and B3LYP-35 a slightly zwitterion character appears in acetonitrile). It has to be noted that for IDMN the presence of an aromatic ring probably makes the two-state picture not appropriate to rationalize the behavior of this molecule, because the zwitterionic form breaks the aromaticity. In Table 3.4.2, molecular dipole moments and isotropic (electronic) static polarizabilities are reported, as a function of the DFT functional both in cyclohexane and in acetonitrile. For both molecules, the molecular dipole moment and the polarizability increases going from apolar to polar solvent, as expected, and decreases by increasing the HF exchange percentage in the functional. Once again, some differences appear in the two molecules. For IDMN the effects on the dipole moment due to the change in the functional are less evident than for the previously analysed geometrical parameters (the largest variation of μ is only of about 2%). IDMN isotropic polarizabilities are slightly more sensitive yielding 4% largest variation going from B3LYP to CAM-B3LYP. For JM, the molecular dipole moment decreases of about 11% moving from B3LYP to

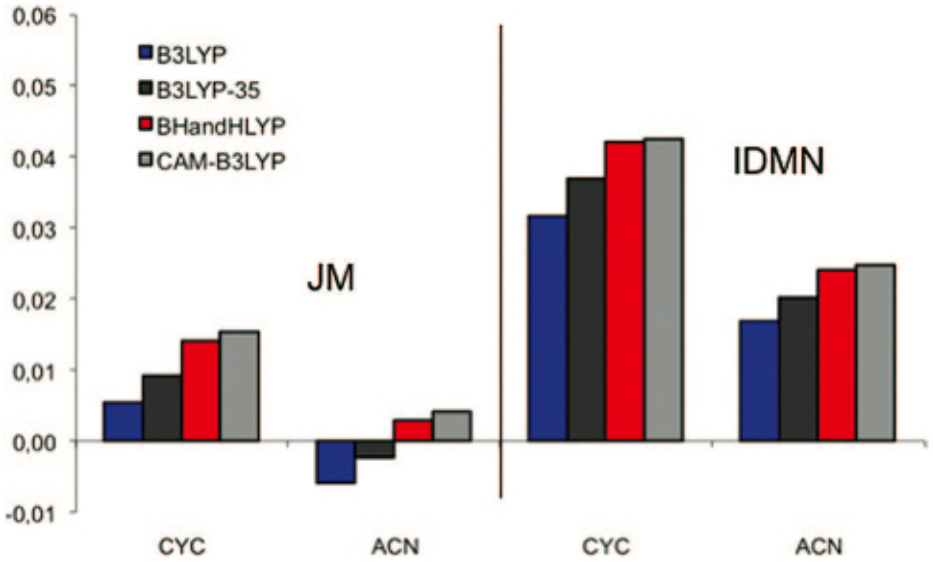

Figure 3.3: Variations of the BLA index for IDMN and JM moving from cyclohexane (CYC) to acetonitrile (ACN), as obtained by using the four selected DFT functionals.

CAM-B3LYP, while the static polarizability decreases of about 6%. In both cases, these data are in agreement with the structural changes reported in the previous section: both dipole moments and polarizabilities increase as the BLA index decreases, i.e., as a more delocalized structure is present.

Vertical Transition Energies.

Before analysing excited state structure and properties, let us start the discussion on the transition properties. As said before, we will focus on the first charge-transfer singlet transition, which has a $\pi - \pi*$ character and is described as HOMO-LUMO for all functionals and both systems (see Figure 3.4).

Table 3.2: **Dipole Moment (Debye) and Isotropic Static Polarizability ($Å^3$) for the Two Molecules in the Two Solvents As Obtained with Different Functionals**

	μ		α	
	CYC	ACN	CYC	ACN
		JM		
B3LYP	13.7	17.3	39.3	50.3
B3LYP-35	13.4	16.7	37.6	47.8
BH&HLYP	13.0	16.1	36.2	45.7
CAM-B3LYP	12.2	15.9	37.1	47.1
		IDMN		
B3LYP	12.3	15.4	39.2	48.5
B3LYP-35	12.3	15.3	37.6	46.2
BH&HLYP	12.3	15.2	36.3	44.3
CAM-B3LYP	12.0	15.1	37.3	45.8

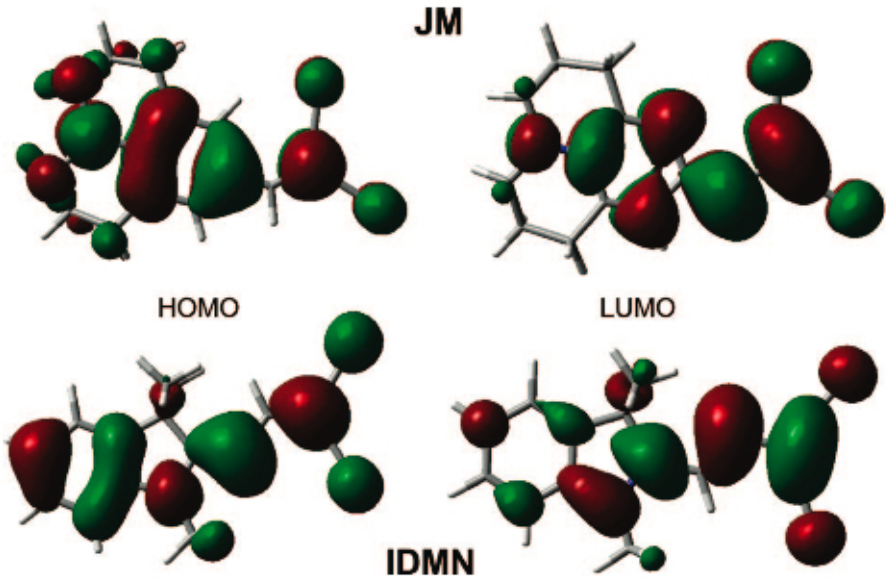

Figure 3.4: Pictorial view of the HOMO and LUMO orbitals of JM and IDMN.

In Table 3.3 vertical excitation energies in the two solvents as obtained within both the LR and the cLR frameworks are reported. To have a better

appreciation of the LR and cLR differences, the common starting energy ($\Delta E_{GS}^{K0,neq}$) obtained in a frozen ground-state solvation is also reported (see section 3.3.2 for details). In general, for both molecules, a decrease in the transition energy value is observed with increasing solvent polarity and such a behavior is common to both LR and cLR. Absolute energies always increase upon passing from LR to cLR. This can be explained using the simple but still effective diagnostic index introduced in eq. 3.53 in terms of differences of dipoles and transition dipoles. As we shall show in the next section, both JM and IDMN present an increase of the dipole moment in the excited state of the order of 3-4 Debye; by using these values and the transition dipoles reported in Table 3.3, we see that the parameter is much larger than one for both systems: this means that $\Delta E_{LR} < \Delta E_{cLR}$. As this increase is similar in both solvents, the solvatochromic shifts remain almost the same passing from LR to cLR. Moving to the comparison with experiments, the absolute energies are always overestimated, whereas solvatochromic shifts are reproduced pretty well by all functionals, especially by CAM-B3LYP. The overestimation of the absolute energies is surely due to a combination of different effects, including those related to the use of a continuum electrostatic only solvation model and more important to the use of a TD-DFT description. To have an idea of the effect of the QM level, we have compared gas-phase TD-DFT results with that obtained at SAC-CI level [12], which is an accurate method to predict transition energies. For IDMN, all functionals overestimate the SAC-CI value of about 0.3, 0.5, 0.7 and 0.6 eV for B3LYP, B3LYP-35, BH&HLYP, and CAM-B3LYP, respectively. If we assume that the intrinsic error due to TD-DFT is not dependent on the solvent, we can subtract the TD-DFT - SAC-CI differences from the energies reported in Table 3.3 to obtain effective energies; with that, a good agreement with experiments is recovered, especially for CAM-B3LYP/cLR.

Excited-State Structure and Properties.

Let us analyse structural changes of the charge-transfer state following the vertical excitation by using, once more, the BLA index (see Figure 3.5). For both molecules, the BLA index for the excited state shows an inverse behavior with respect to the ground state. In both solvents the JM excited state is described as a zwitterion by all functionals (BLA < 0) with the exception of B3LYP in cyclohexane, which gives a small positive BLA. Also, for IDMN a negative BLA is found in both solvents with BHandHLYP and CAM-B3LYP, whereas B3LYP35 in cyclohexane and B3LYP in both solvents give positive and not negligible BLA. From this analysis, it is evident that B3LYP fails at describing structural changes upon excitation, whereas the correct picture is recovered either by increasing the percentage of exact exchange (as in BHandHLYP) or by

Table 3.3: **Excitation Energies (eV) for the Two Molecules in the Two Solvents As Obtained with Different Functionals**[a].

	$\Delta E_{GS}^{K0,neq}$		LR			cLR		
	CYC	ACN	CYC	ACN	shift	CYC	ACN	shift
				JM				
B3LYP	3.27	3.21	3.09 (9.20)	3.04 (9.23)	-0.05	3.22	3.17	-0.05
B3LYP-35	3.43	3.35	3.28 (9.04)	3.21 (9.23)	-0.07	3.42	3.34	-0.08
BH&HLYP	3.62	3.51	3.46 (8.96)	3.37 (9.18)	-0.09	3.59	3.50	-0.09
CAM-B3LYP	3.50	3.40	3.35 (8.96)	3.25 (9.19)	-0.10	3.48	3.38	-0.10
exp			2.84	2.72	-0.12			
				IDMN				
B3LYP	3.37	3.32	3.22 (9.25)	3.19 (9.17)	-0.03	3.36	3.32	-0.04
B3LYP-35	3.57	3.52	3.41 (9.29)	3.39 (9.24)	-0.02	3.56	3.52	-0.04
BH&HLYP	3.76	3.71	3.60 (9.28)	3.56 (9.24)	-0.04	3.75	3.70	-0.05
CAM-B3LYP	3.63	3.58	3.47 (9.32)	3.43 (9.30)	-0.04	3.62	3.57	-0.05
exp			2.90	2.85	-0.05			

[a] *In parentheses, transition dipoles are also reported (Debye). Where available, experimental values [143],[145] are reported.*

separating out the short and long-range contributions (as in CAM-B3LYP). Also, B3LYP-35 introduces significant improvement in the description of the excited-state geometry with respect to B3LYP; however, such an improvement is not sufficient to get the correct picture for IDMN. To characterize the ex-

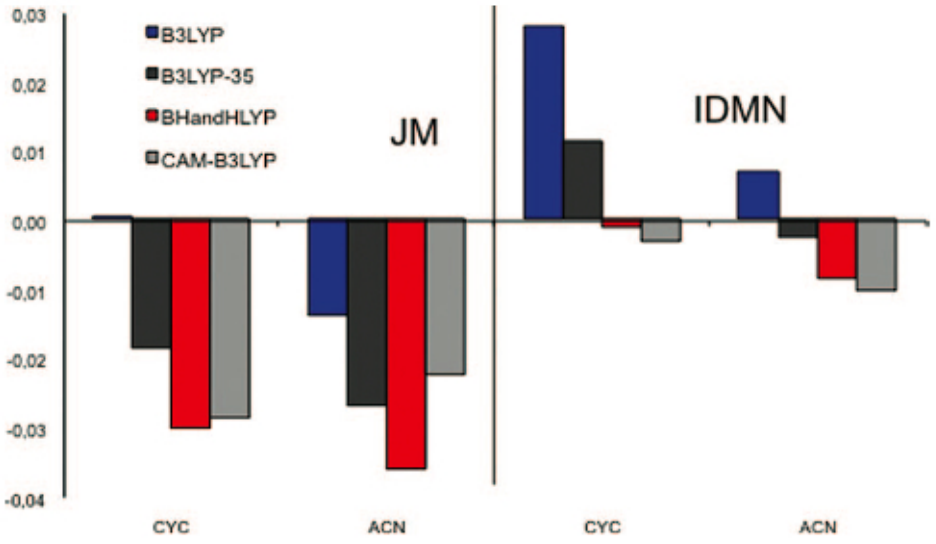

Figure 3.5: Variation of the BLA index following the excitation for JM and IDMN in cyclohexane (CYC) and acetonitrile (ACN). The four selected DFT functionals are considered.

cited states also from the electronic point of view, in Table 3.4 excited-state dipole moments obtained at GS minimum geometry (vertical) and at relaxed geometry for both molecules are reported. This allows us to obtain information on the role played by structural and electronic changes resulting from the electronic excitation. The inspection of the table shows that the major contribution to the change in the dipole moment passing from ground to excited state results from the vertical excitation: the excited-state nuclear relaxation causes only a further slight increase in the dipole moment. This is particularly true for JM in cyclohexane, where the "vertical" dipole is almost equal to that at the excited-state geometry. We recall that in acetonitrile, in addition to the different geometry, the "relaxed" values distinguish from the vertical ones in the solvation regime used, namely nonequilibrium in the vertical and equilibrium in the relaxed.

The effect of the different functional is quite small especially for JM, but some trends can be observed. Looking first to vertical values, we see that in both molecules the increase of exact exchange (passing from B3LYP to

Table 3.4: **Vertical and Relaxed Excited-State Dipoles (Debye) for the Two Molecules in the Two Solvents As Obtained with Different Functionals**

	vertical		relaxed	
	CYC	ACN	CYC	ACN
		JM		
B3LYP	17.56	20.08	17.59	21.46
B3LYP-35	17.08	19.61	17.42	21.51
BH&HLYP	17.07	19.48	17.28	21.42
CAM-B3LYP	17.14	19.45	17.38	21.60
		IDMN		
B3LYP	15.66	18.63	16.7	20.06
B3LYP-35	14.93	17.68	16.17	19.37
BH&HLYP	14.74	17.27	15.45	18.54
CAM-B3LYP	14.86	17.20	15.02	18.05

B3LYP-35 and BH&HLYP) leads to smaller dipole moments. This decrease is counterbalanced by the separation between short- and longrange exchange introduced in CAM-B3LYP. If the effect of the functional on the geometry is also considered using the relaxed dipole moments, we see a different behavior for the two molecules. For JM, all functionals are quite similar, whereas for IDMN, B3LYP gives much larger dipole moments than the other functionals. This unique behavior of B3LYP is a direct consequence of what already commented for BLA reported in Figure 3.5. A final analysis of the change in the state character upon excitation can be obtained in terms of a population analysis. Here the Merz-Kollman (MK) model [154] is adopted by using both the vertical and the relaxed excited-state geometries. To have a more direct analysis, it is convenient to define a CT parameter as

$$f_{CT} = \Delta_D^{EXC-GS} - \Delta_A^{EXC-GS} \tag{3.59}$$

where Δ_X^{EXC-GS} is the difference of charge in the donor or acceptor unit upon excitation. If the excitation really corresponds to a CT from donor to acceptor, then Δ_D^{EXC-GS} is large and positive and Δ_A^{EXC-GS} is still large in absolute value but negative. As a result, f_{CT} will be large and positive. To calculate f_{CT}, we have to define the donor and acceptor units; in both molecules we have

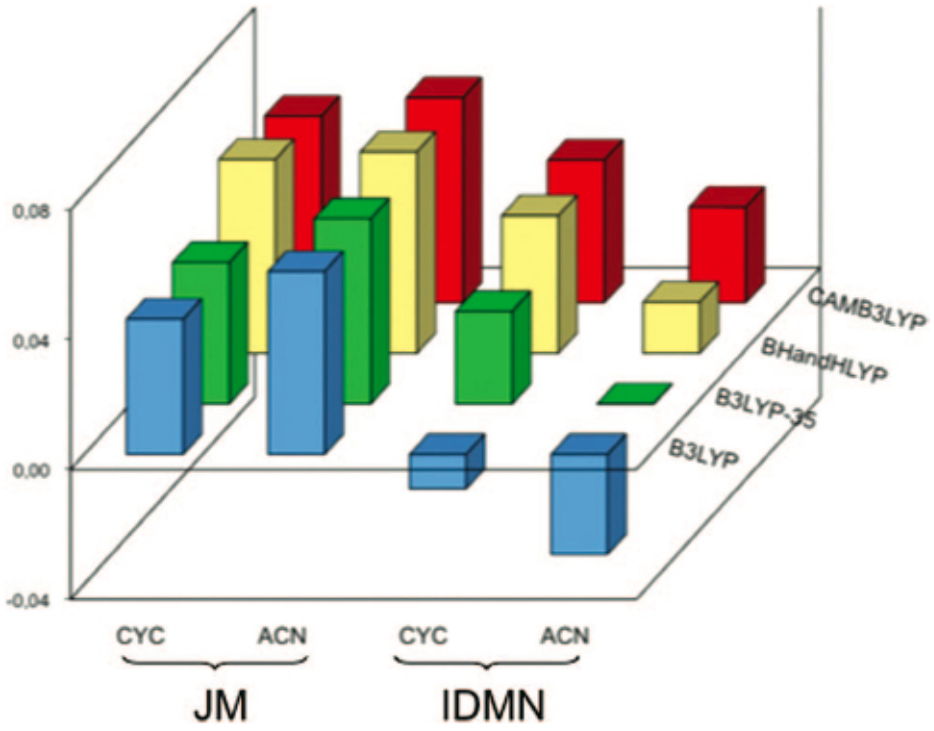

Figure 3.6: f_{CT} parameter (see text) for JM and IDMN in cyclohexane (CYC) and acetonitrile (ACN) with the four selected DFT functionals.

assumed the ring nitrogen atom as the donor and the $C(CN)_2$ as the acceptor. The results obtained are reported in Figure 3.6 for all the functionals and the two solvents. Once again JM and IDMN present quite different behavior: for JM f_{CT} is always positive and increases with the solvent (by increasing the percentage of HF exchange we observe only a small increase). In contrast, for IDMN the effect of the functional is more dramatic as f_{CT} changes sign by increasing the HF exchange. From this graph it is evident that the excitation in JM presents a much more pronounced CT character than IDMN; in IDMN the excited-state character strongly depends on the functional used and in particular on the percentage of HF exchange but also on the separation into short and longrange terms. Note that B3LYP always predicts a reversed flow of charge from the expected acceptor to the donor (i.e., $f_{CT} < 0$).
To conclude the analysis, we will combine the results obtained so far for JM and IDMN ground- and excited-state structures/ properties and use them to simulate UV and Resonance Raman (RR) spectra. In Figure 3.7 the simulated absorption spectra are reported; these are obtained by calculating the Franck-Condon integrals of vibrational wave functions belonging to two different electronic states as implemented into the program FCFAST. Experimental findings taken from refs [143] and [145] are also shown as insets. The simulation of the band shapes was done by using CAM-B3LYP ground- and excited-state geometries and ground state harmonic frequencies (which are assumed to be valid also for the excited state), and a bandwidth of 500 cm^{-1}. This value was taken to reproduce the experimental broadening of the spectrum. So to have a more direct comparison with experimental graphs, spectra are reported in cm^{-1} for JM and in nm for IDMN. For both molecules the agreement between calculated and experimental findings is satisfactory, the relative intensities of the secondary peak (actually a shoulder) correctly decreases by increasing the solvent polarity exactly as in the experimental spectra. Notice, however, that, because simulated spectra are normalized with respect to the absorption maximum, nothing can be said about the main peak intensity passing from one solvent to the other.

Moving now to RR spectra, the main effects of the solvent (position of the peaks and their intensities) can be ascribed to two different origins: one due to the solvent-induced changes in the geometry of both ground and excited states and the other due to the variations induced in the electronic distribution of both states.
As far as concerns the theoretical aspects related to the implementation of PCM-RR, the interested reader can find all the details in ref. [146],[155]; here we shall only recall that the application of PCM to the two computational

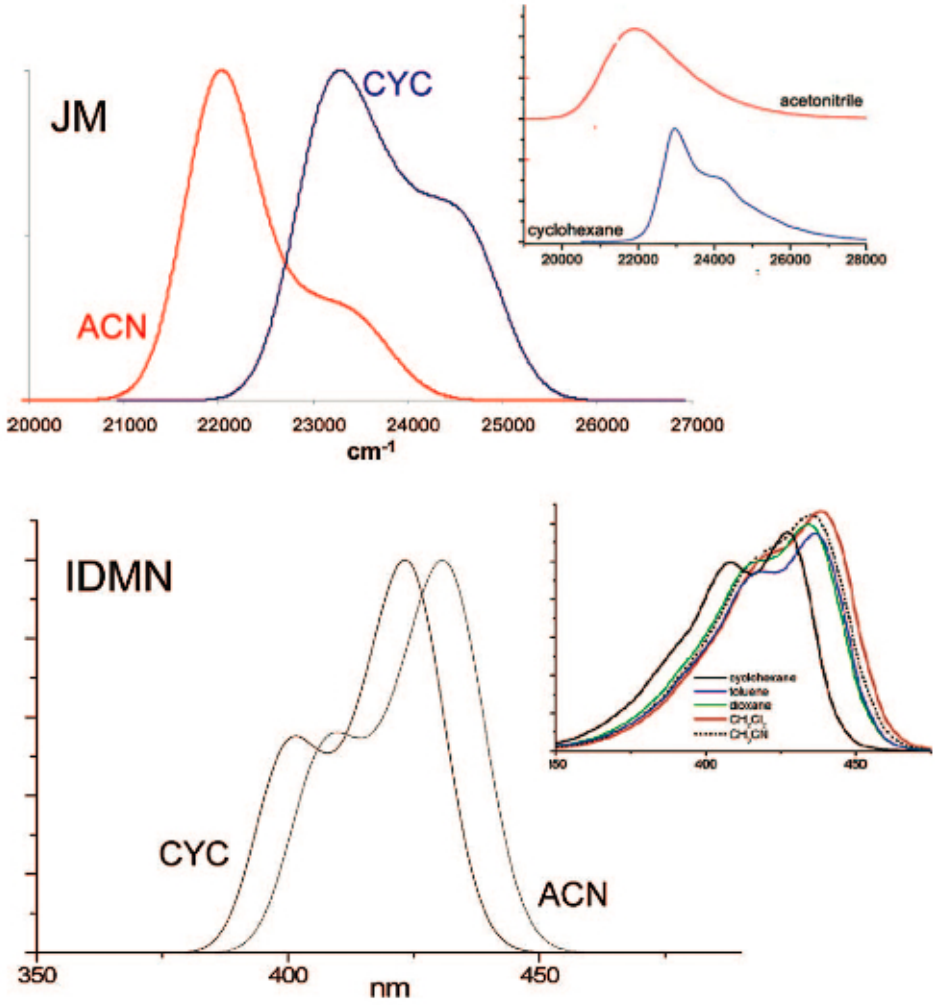

Figure 3.7: CAM-B3LYP simulated absorption spectra for JM and IDMN as obtained by combining calculated excitation energies with Franck-Condon integrals. Experimental findings taken from ref [143].

strategies commonly used to simulate resonance Raman spectra (the transform theory, TT, approach by Peticolas and Rush [156] and the short time dynamics, STD, theory [157],[158]) involves the determination of a different portion of the potential energy surface (PES) for the solvated excited state together with a different solvation regime.
Namely, in TT an equilibrium solvation and a completely relaxed geometry is used to describe the excited state, whereas in STD the vertical (or Franck-Condon) portion of the excited state PES is used together with a nonequilibrium solvation. These differences in the treatment of the solvent effect suggests that the STD approach is more suited than TT to describe the sequence of fast events occurring in the Resonance Raman experiments of solvated systems. An analysis of the effects of these different solvation regimes determining TT and STD spectra of JM can be found in the cited paper. The same molecular system has bee further analysed in a successive paper by Guthmuller and Champagne,[147] where a detailed analysis of the effects of different DFT functionals is reported. Starting from the results of these studies on JM, here it is of interest to focus on IDMN. As said above, the STD better represents the solvation effects on RR spectra; therefore, in the present study the analysis will be limited to STD intensities, which are defined as [157],[158]:

$$I_{0\to 1_m}(\omega_m) \propto \omega_m^2 \Delta_m^2; \qquad \Delta_m = \sqrt{\frac{\omega_m}{\hbar}} \Delta Q_m \tag{3.60}$$

where Δ_m and ΔQ_m are the dimensionless displacement and the displacement along the mass-weighted normal coordinate for mode m (whose vibrational frequency in the ground state is ω_m m), respectively. In the STD framework, ΔQ_m is calculated from the partial derivative of the excited-state electronic energy (E_K) along the normal mode Q_m at the ground-state equilibrium position

$$\Delta Q_m = -\frac{1}{\omega_m^2} \frac{\partial G_k}{\partial Q_m} \tag{3.61}$$

G_k is the free energy of the K state, obtained through eq (riferimento a teoria) within the corrected linear response approach in the nonequilibrium solvation regime.

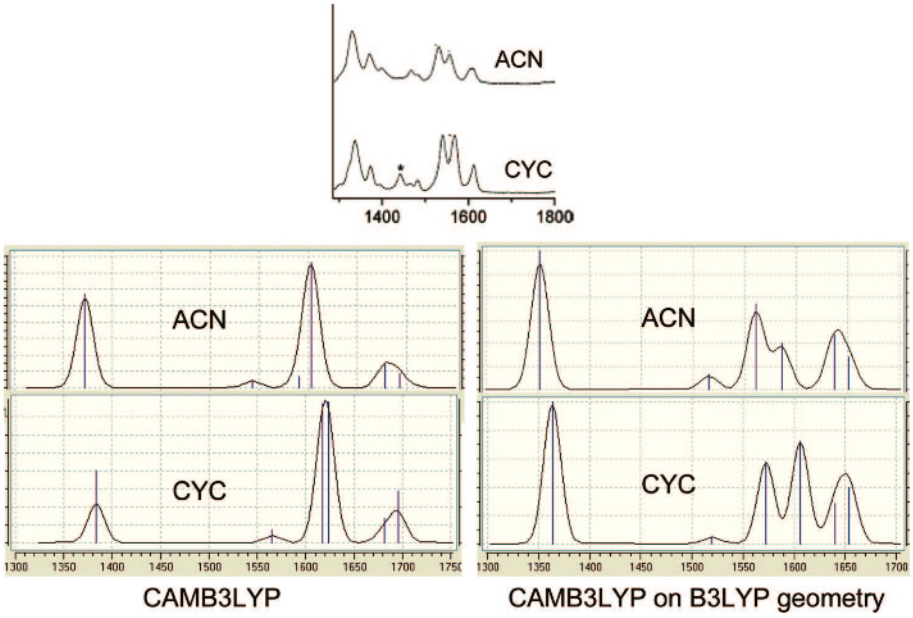

Figure 3.8: Calculated IDMN RRS spectra in the 1300-1800 cm^{-1} range obtained in the STD-cLR approach in cyclohexane (CYC) and acetonitrile(ACN). Experimental spectra taken from ref [145] are also shown as insets.

For the ground-state geometry and frequencies we have used two different functionals, namely CAM-B3LYP and B3LYP, whereas for excited-state gradients only CAM-B3LYP has been used: this functional in fact has shown to be the most reliable method to describe IDMN excited state. Notice that only six normal modes were selected, the ones showing the largest variations upon solvation. The corresponding 1300-1800 cm$^-$1 window of the STD-cLR RR spectra is reported in Figure 3.8 for both solvents (in the inset the experimental spectra are also shown). The mode at about 1360 cm$^-$1 mainly involves the R1 and R4 bond stretching; the peak at about 1520 cm$^-$1 is due to the asymmetric stretching mode of the rings. The normal modes yielding peaks at 1570 and 1606 cm$^-$1 have similar vibrational components, and in particular the first normal mode involves the in-phase R1 and R4 stretching with out-of-phase R2 and R3 stretching; the second mode is composed of the in-phase R2 and R4 and out-of-phase R3 stretching. The other two normal modes (at about 1640 and 1650 cm$^-$1) both involve the benzene ring stretching, and the one at 1650 cm$^-$1 also accounts for the out-of-phase R2 and R3 stretching.
Moving to the comparison with experiments, the main experimental features passing from one solvent to the other are correctly reproduced only by the CAM-B3LYP description using the B3LYP ground-state geometry (and vi-

brational frequencies). Only at this level of description we reproduce the experimentally observed change in the relative intensities of the peaks in the 1500-1600 region of the spectra. These two peaks are assigned to modes having dominant contributions from the R2 and R4 stretches. These are double bonds in the neutral structure but single bonds in the zwitterion, which should make a larger contribution to the structure in polar solvents.
The better agreement obtained with mixed description seems to indicate that CAM-B3LYP gives a less accurate description of the peak position and thus of the ground-state geometry with respect to B3LYP whereas it well describes the nature of the excited state. Such an agreement is not unexpected in light of what has previously been discussed about structural and electronic parameters of the ground and excited states. In fact, although B3LYP gives a good description of the ground state (see, e.g., the discussion on BLA index and vibrational frequencies), CAM-B3LYP is instead more reliable in describing the excited state. In fact, only CAM-B3LYP (and BH&HLYP) give the correct BLA index behavior in the excited state and the corresponding description in terms of charge-transfer character, as evaluated by means of the Merz-Kollman population analysis. These results show that the correct description of RR spectra, which requires the accurate description of the ground- and excited-state PES, is particularly challenging for TD-DFT, so that the use of different functionals and/or basis sets, specifically tailored to the states under examination may be required.

3.5 Application of PCM-LR and PCM-cLR schemes to Nile Red system: The TICT problem

Nile Red (diethylamino-5H-benzo[a]phenoxazin-5-one, NR) is a lipophilic and fluorescent dye, which is used in a large number of technical applications, ranging from solvent mixtures [159] to dye-based lasers [160]. In particular, this molecule undergoes a large solvatochromic shift in the UV-visible absorption spectrum, so that it may be used as a polarity probe in a variety of chemical and biochemical environments [161]. The large solvent sensitivity of NR originates in the significant increase of dipole moment occurring when going from the ground to the lowest excited state, that indicates a large electronic reorganization upon excitation. Accurate experimental determinations of dipole moment variations have been attempted in the past years, but the obtained values exhibit considerable discrepancies, ranging between 5 and 12 D [162],[163],[164],[165],[166],[167],[168]. In contrast, more recent experiments, based on a systematic analysis of absorption and fluorescence spectra of NR in several solvents, suggest a much smaller modification of about 1.8 D [169]. Spectroscopic properties of NR are even more interesting. Indeed NR presents a fluorescence spectrum with two peaks (often interpreted as dual fluorescence) centred at ca. 530 and ca. 570 nm in apolar solvents (more specifically values of 525 and 570 nm, and 538 and 568 nm have been measured in n-hexane4 and in n-heptane [170], respectively). Though modulated, this behaviour is retained in non-protic media [163] but also in more complex chemical environment such as binary solvent mixtures with a high water ratio [162] or reverse micelles [170].
These experimental studies suggest that this peculiar spectroscopic fingerprint could be related to a twisted intramolecular charge transfer (TICT) process [171],[172], the same mechanism used to explain the anomalous dual fluorescence of 4,40-dimethylaminobenzonitrile (DMABN) [173].

From an electronic point of view, TICT states are accessible in multichromophoric systems possessing a weakly coupled electron donor (D) and electron acceptor (A). Two stable conformations are then obtained in the lowest excited state by twisting the D and A moieties, one with respect to the other. In NR, the acceptor and donor parts are the ketone and the diethylamino groups, respectively, whereas the twisting angle (θ) corresponds to a rotation around the C–N bond (see Fig. 3.9).

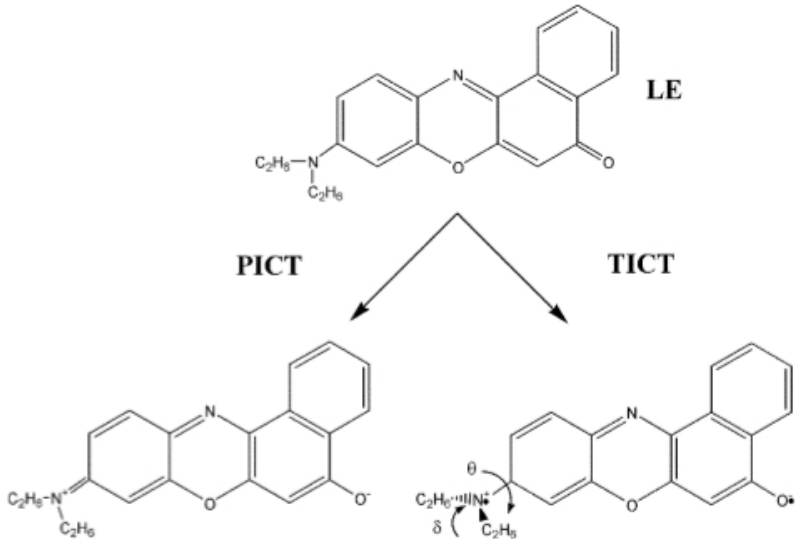

Figure 3.9: Sketch of the locally excited (LE), the planar and twisted intramolecular charge (PICT and TICT) forms of NR

The formation of the TICT state can be viewed as an adiabatic photoreaction proceeding on the S1 potential energy surface (PES). Indeed the originally reached locally excited (LE) state with planar conformation has only a weak CT character (large mesomeric interaction between D and A results in an incomplete charge separation) whereas in the twisted TICT conformation, a significantly larger electronic charge is transferred from D to A, since the mesomeric interaction is blocked (see Fig. 3.9).
In alternative to the TICT process, another interpretation of experimental data, based on the so-called planar ICT (PICT) model, rejects the necessity of a large-amplitude motion for the formation of a highly polar ICT state [174]. Such hypothesis is based on the equilibration dynamics between the LE and ICT state which takes place on a picosecond scale, with rates increasing when larger alkyl groups substitute the amino moiety [175].
The PICT model postulates an ICT structure with an increased double bond character between the D and A moieties (C–N bond in NR), resulting in a partial positive charge on the amino group and a quinoidal resonance structure. In a more general interpretation of the model, it is claimed that the vibronic coupling could play a non-negligible role and that a large (nearly perpendicular) twist is unnecessary to form the highly polar ICT state [176]. The controversy on the TICT vs. PICT process in DMABN and derivatives is for many aspects still open at both experimental and theoretical levels [173],[177],[178],[179],[180]. More generally, these mechanisms are antagonist

in many photoinduced CT processes, as, for instance, those present in metallic complexes mimicking photosynthesis [181]. Few theoretical papers have attempted to obtain some hints on the nature of NR optical properties. Previous semi-empirical (ZINDO/S) calculations showed the existence of two stable conformers in the lowest (S_1) excited state, characterized by very different dipole moments, thus supporting the TICT proposal [166]. However, ab initio calculations, based on the configuration interaction with single excitations (CIS) approach, indicate that the LE state is planar and has a larger dipole moment than the corresponding twisted structure, contradicting the TICT proposal [182]. More recently an extensive study, based on TD-DFT and CIS calculations, suggested that the LE state exhibits a red shift in the emission spectra, and no evidence of a twisted intramolecular charge transfer state was found [183]. However, the authors of this latter work called for a more systematic analysis based upon more reliable TD-DFT structures for excited states.

We present here a detailed theoretical analysis of the lowest excited state (S_1) features of NR. The main goal is to determine the structural and electronic features of NR in its S_1 state and, from them, to gain insights on the nature of the apparent dual fluorescence observed in the experiments. To this end, TD-DFT studies of the absorption and fluorescence spectra, both in gas phase and in heptane solution, have been carried out. A particular attention has been devoted to the conformational effects tuning the emission behaviour. From a more computational point of view, the performances of several exchange–correlation functionals have been analysed. Indeed the existence of a TICT implies a charge transfer transition, which, as above mentioned, could be poorly described at TD-DFT level if conventional functionals are selected (see section 2.6 and refs [26],[72],[184],[73]). At the same time, it is interesting to assess the behaviour of the selected functionals and of TD-DFT approach itself in reproducing PES characteristics relatively far from energy minima and the IEFPCM/LR and cLR perfomances in investigating TICT or PICT excitations in solution.

3.5.1 Computational Details

All DFT and TD-DFT calculations have been carried out with a development version of the Gaussian suite [78], using five hybrid functionals including an increasing fraction of Hartree–Fock exchange (HF-X) and two range-separated hybrids (RSHs): B3LYP, (20% of HF-X), B3P86 (20% of HF-X), PBE0 (25% of HF-X),43 BMK (42% of HF-X), BH&HLYP (50% of HF-X), CAM-B3LYP (19% short range and 65% long range of HF-X) and the LC-ωPBE (0% short range and 100% long range of HF-X). In this last functional, a larger damping

parameter (0.40 a.u. instead of 0.33 a.u. for CAM-B3LYP, see section 2.2) is selected, so that a relatively larger HF-X is included at intermediate interelectronic separation.
All the calculations (geometry optimization, absorption and emission) have been carried out with the 6-311G(d,p) basis set. To verify the convergence on the transition energies, some tests have been carried out with the 6-31+G(d,p): differences smaller than 0.04 eV have been found for the first transition.
A series of SAC-CI [12] calculations with 6-31G basis set have been performed to obtain qualitative wave function benchmarks for rigid scan of excited state PES. Test calculations have shown that the (computationally prohibitive) consideration of diffuse functions in the SAC-CI calculations does not alter the shape of the PES. The SAC-CI calculations have been performed in the frozen-core approximation, using tight (L3) thresholds and neglecting the R2S2 integrals.
Solvent effects have been introduced by exploiting the IEF-PCM approach and the default set of sphere radii (UA0) implemented in the Gaussian code [78] has been used. Vertical absorption and emission energies have been obtained, by exploiting both the linear response (LR) and the corrected LR (cLR) schemes (sections 3.3.1 and 3.3.2).
Vibrationally resolved spectra within the harmonic approximation have been computed using the FC classes program [185]. The simulated spectra (at 298 K) have been convoluted using Gaussian functions with a full width at half maximum (FWHM) of 0.07 eV. All initial states with a Boltzmann population $> 30\%$ of that of the ground state were considered for a total of 40 initial vibrational states. A maximal number of 24 overtones for each mode and 19 combination bands on each pair of modes were accounted for.

3.5.2 Results and Discussion

A limited number of computational studies of the ground state properties and electronic spectra of NR can be found [164],[182],[183]. In particular, it is worth highlighting a very recent and detailed conformational analysis of NR in the ground electronic state which has demonstrated that all the conformers present wavelength of maximal absorption differing only by 3nm for the lowest state [183]. Amongst all conformers, the most stable is characterized by an almost planar rearrangement with only the two ethyl groups of the amino moiety lying outside the molecular plane (on opposite sides). This conformer has been considered in the present study and constitute the starting point of the results reported herein.

Absorption Spectrum

The absorption spectrum of NR in the range 400–600 nm range is characterized by two band maxima at 488 (2.54 eV) and 508 nm (2.44 eV) in n-hexane4 and 490 nm (2.53) and 510 (2.43 eV) in n-heptane [170]. Additionally, spectroscopic studies revealed significant variations in the absorption (and emission) bands positions and intensities as functions of the solvent polarity [162].

Table 3.5 lists the three lowest electronic transitions calculated with different functionals. Of these three transitions the first one is the only with an oscillator strength different from zero, for all the considered theoretical approaches. It mainly corresponds to a $\pi - \pi^*$ transition from HOMO to LUMO (see Fig. 3.10).

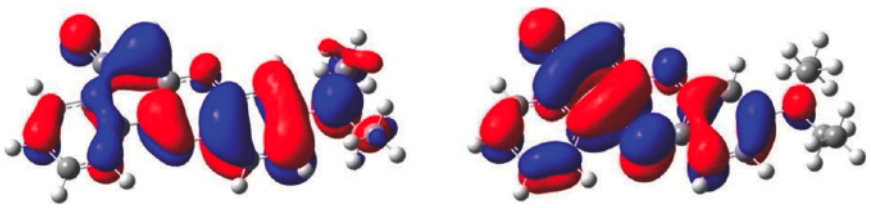

Figure 3.10: NR HOMO (left) and LUMO (right) obtained with the CAM-B3LYP functional

An analysis of the orbital shapes suggests that the traditional assignment of this band to an electronic CT from the amino donor to the carbonyl acceptor is only partially fulfilled. Indeed, only a small decrease of the donor group in the LUMO orbital is observed with a parallel increase of the acceptor contribution. The map of the electron density variation from S_0 to S_1 reported in Fig. 3.11 also supports this picture, with a small negative variation around nitrogen atom and positive values on the C=O side. However it is not possible to clearly evidencing a net charge transfer.

It is interesting to note that, as expected, [26] increasing the HF-X ratio in the GH functionals yields larger transition energies, that ranges from 2.7 (B3LYP and B3P86) to 3.2 eV (BH&HLYP). Even higher energy transitions are found with the LC-ωPBE (3.5 eV), while the CAM-B3LYP approach shows an intermediate behaviour between BMK and BH&HLYP. In fact, all selected functionals provide larger transitions larger than the SAC-CI reference (2.5 eV, obtained with a smaller basis set), B3LYP being the closest (+0.2 eV). The inclusion of solvent effects (n-heptane) shifts all the transitions to lower energies by an almost constant quantity (ca. 0.2 and ca. 0.1 eV within the LR

Table 3.5: **Computed absorption energies (in eV) and oscillator strengths (in parenthesis) for the three lowest excited states. For the S_1 state we also report values calculated in n-heptane solution with both the LR and cLR schemes**

	S_1			S2	S3
Model	Gas-phase	n-Heptane (LR)	n-Heptane (cLR)	Gas phase	Gas phase
B3P86	2.75 (0.73)	2.58 (0.90)	2.68 (0.90)	2.91 (0.0)	3.30 (0.0)
B3LYP	2.74 (0.73)	2.58 (0.90)	2.67 (0.90)	2.93 (0.0)	3.29 (0.0)
PBE0	2.83 (0.76)	2.65 (0.93)	2.75 (0.93)	3.06 (0.0)	3.43 (0.0)
BMK	3.05 (0.84)	2.87 (1.02)	2.97 (1.02)	3.45 (0.0)	3.83 (0.0)
BH&HLYP	3.23 (0.90)	3.04 (1.07)	3.13 (1.07)	3.86 (0.0)	4.10 (0.0)
CAM-B3LYP	3.13 (0.84)	2.95 (1.01)	3.05 (1.01)	3.56 (0.0)	3.95 (0.0)
LC-ωPBE	3.47 (0.91)	2.28 (1.08)		3.80 (0.0)	4.36 (0.0)
SAC-CI	3.05 (0.85)			3.73 (0.0)	4.36 (0.0)

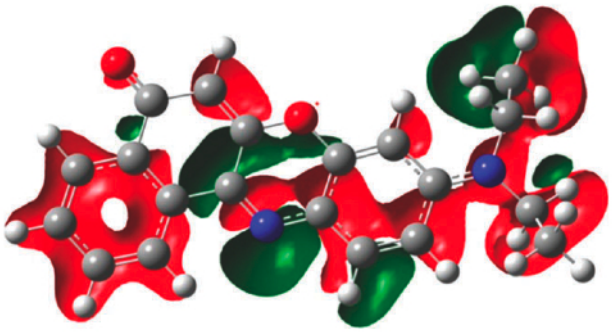

Figure 3.11: Electron density difference between S_1 and S_0 (green positive, red negative).

and the cLR scheme, respectively). From the data reported in Table 3.5, it is quite apparent that a relatively good agreement between the lowest experimental transition energy (2.43 eV) and the TD-DFT values is reached, with errors ranging between +0.15 (B3LYP, B3P86) and +0.61 eV (BH&HLYP). The minimal deviations, obtained with B3LYP, B3P86 and PBE0, are within the typical error bar foreseen for the selected level of theory [26]. However, none of the considered methods reveals a second strong absorption, all the other transitions (up to 4 eV) being characterized by null oscillator strengths (see Table 3.5). These results seem to indicate that the second peak observed in the experiments is not due to a second electronic state.

Table 3.6: **Computed dipole moments (D) for the ground state, as well as for the vertical and adiabatic S_1 state**

	S_0		S_1 vertical		S_1 adiabatic	
Functional	Gas phase	n-Heptane	Gas phase	n-Heptane	Gas-phase	n-heptane
B3P86	8.9	10.6	12.7	14.3	11.5	14.1
B3LYP	8.7	10.4	12.6	14.2	11.4	13.9
PBE0	8.7	10.3	13.1	14.3	11.4	13.9
BMK	7.8	9.9	12.6	14.6	11.3	14.1
BH&HLYP	8.4	9.2	13.0	14.2	11.6	13.7
CAM-B3LYP	7.8	9.1	12.7	14.2	11.4	13.8
LC-ωPBE	7.3	8.4				

Additional information on the nature of the excited states can be obtained by the analysis of dipole moment variations from ground to excited states. In

particular, as stated in the Introduction, early experimental data suggested a dipole variation as large as 5.0 and 6.9 D, whereas more recent studies point towards a significantly lower change of about 1.8 D [169],[186]. In Table 3.6, all the computed ground, vertical (i.e. at S0 geometry) and adiabatic (i.e. at S_1 geometry) dipole moments are reported. Ground state dipole moments range between 10.6 D (B3P86) and 8.4 D (LC-ωPBE), this last value being in very good agreement with measurements (8.4 D/8.7 D) [162],[170]. In contrast, all the computed dipoles for vertical S_1 state are around 14 D, so that variations are between 3 and 5 D, the upper limit being obtained with CAM-B3LYP and BH&HLYP.

Emission Spectrum

As reported in the introduction to this section, NR presents a fluorescence spectrum with two peaks (often interpreted as dual fluorescence) centred at 2.18 eV (570 nm) and 2.36 eV (525 nm) in n-hexane,4 and 2.18 eV (568 nm) and 2.30 eV (538 nm) in n-heptane [170]. The significant redshift observed between absorption and emission bands is an indication of a structural change in the excited state.

Table 3.7: **Computed emission maxima (eV) in the gas phase and in solution**

	Gas-phase	n-Heptane (LR)	n-Heptane (cLR)
B3P86	2.55	2.40	2.52
B3LYP	2.54	2.39	2.50
PBE0	2.59	2.44	2.56
BMK	2.70	2.53	2.66
BH&HLYP	2.77	2.59	2.73
CAM-B3LYP	2.69	2.51	2.64
LC-ωPBE[a]	2.81	2.60	
SAC-CI	2.67		

[a] *Computed using CAM-B3LYP S_1 structure.*

In Table 3.7 the emission energies, computed for the isolated and the solvated molecule, using the optimized S_1 geometries are reported. These transition energies range between 2.5 (B3LYP) and 2.8 (BH&HLYP). As for the absorption, the largest values are obtained by increasing HF exchange. The inclusion of solvent effects leads to a small red-shift which further reduces when the cLR scheme is used. As mentioned above, the Stokes shift is generally

explained in terms of a structural variation in going from the ground to the excited state. Some key structural parameters, obtained upon TD-DFT optimization of the S_1 structure, are reported in Table 3.8f and Fig. 3.12. In particular, Table 3.8 collects the values obtained for the twisting (θ) and pyramidalization (δ) angles. The twisting angle is defined as the average of the two dihedrals C2–C1–N28–C36 and C5–C1–N28–C29, while pyramidalization angle (δ) is defined as the deviation from planarity of the three atoms attached to the nitrogen (180^o - —C1–N28–C29–C36—), see Fig. 3.9 for labelling. As it clearly appears from these data, NR is only slightly twisted in the ground state ($5 \leqslant \theta \leqslant 7$), while the angle d is always very close to 01. Both angles are slightly affected by electronic excitations and by solvent effects. Going from the ground to excited state, B3LYP, B3P86 and BMK calculations predict a small increase of twisting angles whereas BH&HLYP and CAM-B3LYP yield a small decrease.

Table 3.8: **Computed values (degrees) for the twisting (θ) and pyramidalization (δ) angles**

	S_0				S_1			
	Isolated		Solvent		Isolated		Solvent	
	θ	δ	θ	δ	θ	δ	θ	δ
B3P86	5.5	0.3	5.5	0.4	6.1	0.3	6.1	0.3
B3LYP	5.8	0.3	5.7	0.4	6.3	0.3	6.3	0.3
PBE0	5.5	0.4	5.6	0.4	6.0	0.3	6.0	0.3
BMK	7.1	0.3	6.9	0.4	7.2	0.6	7.0	0.3
BH&HLYP	6.2	0.3	6.1	0.4	5.9	0.4	5.7	0.4
CAM-B3LYP	5.9	0.4	5.2	0.6	5.8	0.5	5.8	0.5

More significant variations are instead found for two bond lengths in the D and A units, namely C–N and C=O bonds, shown in Fig. 3.12. In particular, B3LYP and B3P86 calculations predict an increase of both bonds upon S0–S_1 transition, whereas BMK, BH&HLYP and CAM-B3LYP describe a decrease of the C–N bond and a parallel increase of C=O bond. In other words, functionals with a small HF-X fraction (B3LYP, B3P86) suggest that the CN bond has a larger "single bond" character (lengthening) in the excited state than in the ground state, whereas RSH and GH functionals including a larger HF-X fraction indicate that the CN bond gains more 'double-bond' character (shortening) in the excited state. The first description suggests a TICT state, whereas the second is consistent with a PICT process.

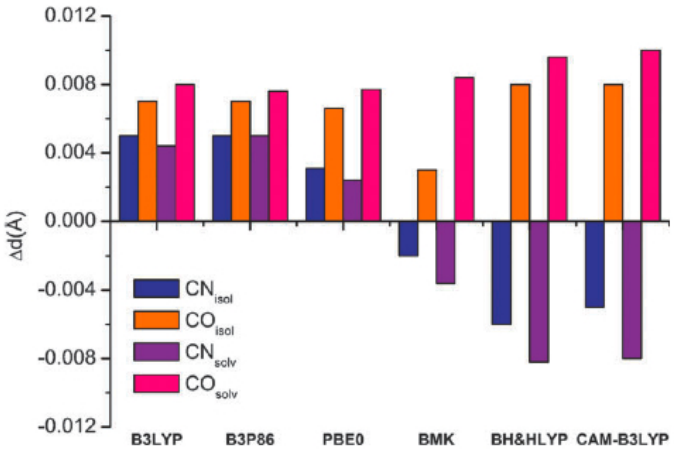

Figure 3.12: Variation ($\AA$) of the C–N and C=O bonds going from S_0 to S_1 state, computed both in gas phase and solution (n-heptane).

Finally it is worth noting that the dipole moment in the excited state only slightly changes upon structural relaxation as shown by the values reported in Table 3.6. This result is in clear contrast with a typical TICT behavior, e.g. in DMABN a variation of ca. 10 D was found [180].

Analysis of TICT process

According to the TICT model, upon electronic excitation, the molecule initially forms a moderately non-polar state presenting geometry features similar to that of the ground state. Next, an electron is transferred from the donor to the acceptor, subsequently leading to a twisted molecular configuration, in which D and A moieties are nearly perpendicular with respect to each other. As mentioned above, the active molecular degree of freedom for Nile Red is the rotation of the amino group around the CN bond connecting the $N(C_2H_5)_2$ unit to the rigid aromatic withdrawing system. Still according to the TICT models, the TS connecting the nearly nonpolar state to the highly polar product, is more polar than the reactant. As a result, the preferential solvation of the more polar TS compared to the reactant causes a decrease in the activation barrier of the TICT process with increasing the polarity of the medium. Therefore, the highest barriers should be expected in nonpolar or low-polar solvents, such as n-heptane.

Previous theoretical studies, carried out at semiempirical [166] and CIS level [183] (see section 3.5), have shown that NR is quasiplanar in the ground

state and presents a large rotation barrier for the diethylamino group. This large barrier is not significantly altered for the first excited states.
In order to gain further insights on the TICT hypothesis and to possibly localize a second fluorescent stable structure on the excited electronic surface, a TD-DFT rigid scan of the twisting angle θ has been carried out using selected functionals (B3LYP, BH&HLYP, CAM-B3LYP). The obtained energy profiles are collected in Fig. 3.13 together with SAC-CI results.
As it can be noted, the B3LYP curve is the only one showing a second minimum at 90^o, whose depth increases in presence of the solvent (B3LYP/solv data in Fig. 3.13). Upon complete relaxation this twisted structure becomes more stable than the planar one by -0.19 eV. In contrast, all the other functionals do not detect a twisted stable structure. It is note worthy that BH&HLYP and CAM-B3LYP provide qualitatively similar profiles to SAC-CI plot. This is consistent with previous findings demonstrating that RSH hybrids provide results closer to highly correlated wave function schemes for longrange CT excitations [187],[184].
The difference found here in the absolute energies could be partially ascribed to the smaller basis set used in the SAC-CI calculations. Furthermore, the CAM-B3LYP profile is not shifted by solvent, thus indicating a small variation of the charge transfer between D and A units as a function of the twisting angle.

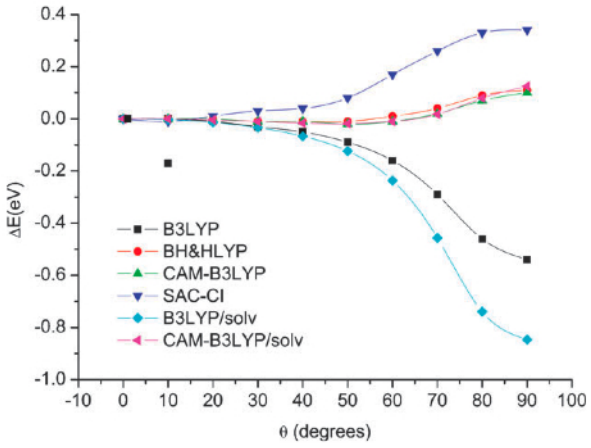

Figure 3.13: Relative energy profiles (in eV) of the S_1 state with respect to the planar structure obtained in a rigid scan of the twisting angle.

A similar behaviour is revealed also by the Merz–Kollman (MK) charges [154]. As in the case of Push-pull systems study,the charge transfer parameter as f_CT is the charge difference in the donor or acceptor unit between ground

and excited state. The donor and acceptor groups are the $N(CH_3)_2$ and the C=O moieties, respectively. The results obtained for the selected functional, reported in Fig. 3.14, refer to the 0 and 90 degrees values of twisting angle of the excited state geometry.
For the planar structure, all functionals give the same picture and they indicate that there is not a significant CT, whereas different behaviors are found for the twisted structure. Indeed, B3LYP results suggest a significant CT at $\theta = 90^o$, thus supporting the hypothesis of a TICT process while all the other functionals indicate a PICT process. In addition, it must be pointed out that, assuming valid the TICT structure found at B3LYP level, the corresponding emission would be found at about 1.7 eV (after complete optimization), a value in clear disagreement with the experimental data. To summarize, from

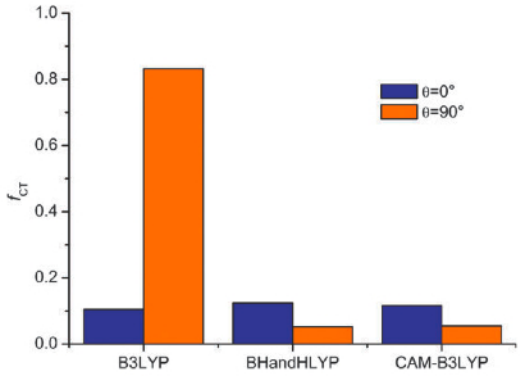

Figure 3.14: Gas-phase values of the charge transfer parameter (f_{CT}, see text for definition) for two different values of the y dihedral angle in the excited state of Nile Red.

the present analysis it comes out that NR presents important differences with respect to typical TICT systems such as DMABN.
In TICT systems, LE and CT states are usually very close to each other in the S_0 structure and their relative stability strongly depends on the θ angle: a planar ($\theta = 0^o$) rearrangement correspond to a more stable LE configuration, whereas the CT state is lower in energy at the twisted conformation ($\theta \approx 90^o$). In contrast, NR is characterized by only one electronic state along the twisting coordinate; this behavior better fits with the PICT picture.

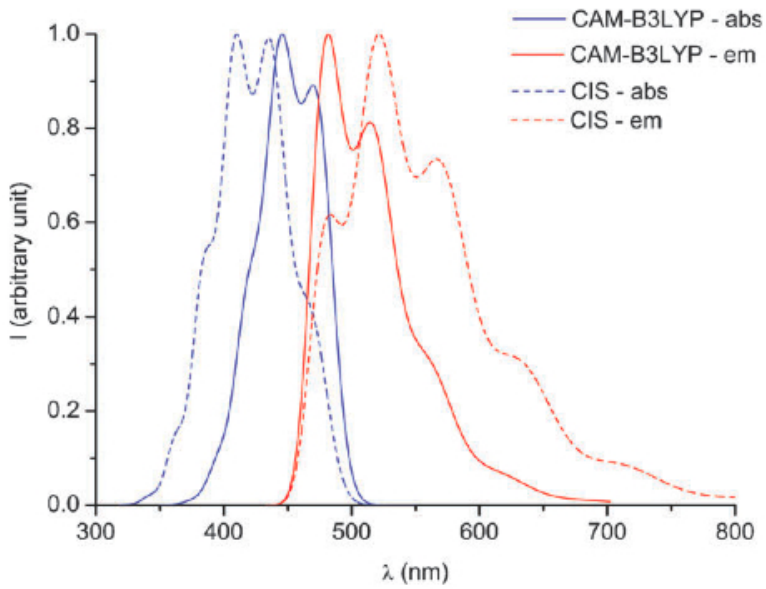

Figure 3.15: Gas-phase CAM-B3LYP absorption and emission vibronic spectra. The spectra have been obtained by fitting with gaussian functions having a full width at half maximum of 0.07 eV and by renormalizing to the maxima.

Therefore, the origin of the double band in the absorption and fluorescence spectra should have another origin and some insights can be given by vibronic couplings. Indeed, in Fig. 3.15 are reported the vibronic spectra for both absorption and emission, computed at CIS and CAM-B3LYP level. These spectra have been obtained by using gas-phase harmonic frequencies (HF/CIS and CAM-B3LYP) and the CAM-B3LYP adiabatic energy difference computed in solution. As it can be seen from the graph, the CAM-B3LYP absorption spectrum shows two absorption maxima separated of 0.14 eV, in excellent agreement with the experimental split (0.10 eV).
Furthermore, the relative intensities are in good agreement with the experimental data so that the overall shape of the spectrum is well reproduced by this theoretical level. The same trends hold for the CAM-B3LYP emission spectrum: also in this case a double band shape is found with a calculated splitting (of 0.16 eV) close to the measured value (of 0.12 eV) and with the relative intensities in good agreement with experiments. A more detailed analysis of the vibronic contributions indicates four main normal modes. The one giving the most intense contribution corresponds to a mode at 1613 $cm^{-}1$ which can be described as a combination of aromatic ring deformation and of C–N double bond stretching. This mode well represents the global electronic

rearrangement induced by the PICT process (see Fig. 3.9).
The band maxima, computed with the inclusion of the vibronic couplings, are at 446 and 469 nm for the absorption and at 480 and 514 nm for the emission, very close to the experimental values (490/510 and 538/568 nm for the absorption and emission, respectively). As matter of fact, the CAM-B3LYP error is of about 0.24 eV for the four bands, in line with previous reported benchmarks,26 and, very interestingly, the accuracy is similar for S_0 - S_1 and S_1 - S_0 transitions. Finally, CIS spectra have a shape globally similar to those of CAM-B3LYP spectra but the relative intensities are different and, more important, absorption is blue-shifted whereas emission is red-shifted. This last result suggests that the CIS frequencies cannot be used for vibronic coupling evaluation on the top of TD-DFT transition energies.

3.6 A new Self Consistent Linear Response scheme

In the previous sections the theoretical formulation and some applications of PCM-LR and PCM-cLR approaches for excited states were presented. Here we present a new approach wich improves the cLR strategy toward a self-consistent state specific description iteratively. We call this approach *Self Consistent Linear Response* (SCLR)

As described in section 3.3.2, a correction to the LR approach is obtained by calculating the relaxed density through the Z-vector approach, applied to the case of linear response in the presence of solvent. In such a formulation however, the $\mathbf{P}^{\Delta}$ obtained is used to calculate the new charges $\mathbf{q}^{\Delta}$ without a self consistent procedure between $\mathbf{P}^{\Delta}$ and $\mathbf{q}^{\Delta}$. The strategy here proposed, is to recover this self consistency by an iterative procedure. To have a clear description of the theoretical and computational aspects of the new strategy we adopt a CIS formulation but all the results are validalso for a TD-DFT formulation.
Let us start with the definition of some quantities needed later. For a generic excited state K, we expand the wave function in terms of single excitation determinants

$$|\tilde{\Psi}^K\rangle = \sum_{ia} M_{ia}^K |\tilde{\Phi}_i^a\rangle \tag{3.62}$$

where

$$\tilde{\Phi}^L = \tilde{\Phi}_i^a = \tilde{\Phi}^{GS}(i \rightarrow a) \tag{3.63}$$

The superscript "$\sim$" indicates solvated quantities. We set the ortogonality of wave functions:

$$\langle\tilde{\Psi}^K|\tilde{\Psi}^J\rangle = \delta_{KJ} \tag{3.64}$$

Therefore, for the ortogonality of Slater Determinats involved:

$$\sum_{ia}(M_{ia}^K)^2 = 1 \tag{3.65}$$

Finally, we write the rules for matrix elements of PCM Slater determinants,

considering that in our scheme, in which the charges have already been determined and stored, the operators $\hat{V}^{PCM}$ are one-electron operators:

$$\langle\tilde{\Phi}_i^a|\hat{H}_{GS}^{eff}|\tilde{\Phi}_j^b\rangle = [\tilde{E}^{GS} + (\tilde{\varepsilon_a} - \tilde{\varepsilon_i})]\delta_{ij}\delta_{ab} - \langle\tilde{a}\tilde{i}||\tilde{b}\tilde{j}\rangle \tag{3.66}$$

$$\langle\tilde{\Phi}_i^a|\hat{V}_{PCM}^x|\tilde{\Phi}_j^b\rangle = \left[\tilde{V}^{GS}q^x + \left(\langle\tilde{a}|\hat{V}_\sigma|\tilde{a}\rangle - \langle\tilde{i}|\hat{V}_\sigma|\tilde{i}\rangle\right)q^x\right]\delta_{ij}\delta_{ab} \tag{3.67}$$

The free energy for a generic excited state K is:

$$\begin{aligned}
\mathcal{G}_{CIS}^K &= \langle\tilde{\Psi}^K|\hat{H}_{vac} + \frac{1}{2}\hat{V}_{PCM}^K|\tilde{\Psi}^K\rangle \\
&= \langle\tilde{\Psi}^K|\hat{H}_{vac} + \frac{1}{2}\hat{V}_{PCM}^{GS} + \frac{1}{2}\hat{V}_{PCM}^{\Delta}|\tilde{\Psi}^K\rangle \\
&= \langle\tilde{\Psi}^K|\hat{H}_{vac} + \frac{1}{2}\hat{V}_{PCM}^{GS}|\tilde{\Psi}^K\rangle + \langle\tilde{\Psi}^K|\frac{1}{2}\hat{V}_{PCM}^{\Delta}|\tilde{\Psi}^K\rangle \\
&= \sum_{ia}\sum_{jb} M_{ia}^{K*}M_{jb}^K\langle\tilde{\Phi}_i^a|\hat{H}_{vac} + \frac{1}{2}\hat{V}_{PCM}^{GS}|\tilde{\Phi}_j^b\rangle \\
&\quad + \frac{1}{2}\sum_{ia}\sum_{jb} M_{ia}^{K*}M_{jb}^K\langle\tilde{\Phi}_i^a|\hat{V}_{PCM}^{\Delta}|\tilde{\Phi}_j^b\rangle
\end{aligned} \tag{3.68}$$

the first term can be derived from the definition of energy eq. (3.21) adding and subtracting $\frac{1}{2}\hat{V}_{PCM}^{GS}$:

$$\begin{aligned}
&\sum_{ia}\sum_{jb} M_{ia}^{K*}M_{jb}^K\langle\tilde{\Phi}_i^a|\hat{H}_{vac} + \frac{1}{2}\hat{V}_{PCM}^{GS}|\tilde{\Phi}_j^b\rangle = \\
&= \sum_{ia}\sum_{jb} M_{ia}^{K*}M_{jb}^K\langle\tilde{\Phi}_i^a|\hat{H}_{GS}^{eff}|\tilde{\Phi}_j^b\rangle + \\
&- \frac{1}{2}\sum_{ia}\sum_{jb} M_{ia}^{K*}M_{jb}^K\langle\tilde{\Phi}_i^a|\hat{V}_{PCM}^{GS}|\tilde{\Phi}_j^b\rangle
\end{aligned} \tag{3.69}$$

Using the Slater-PCM rule (3.66):

$$\sum_{ia}\sum_{jb} M_{ia}^{K*} M_{jb}^{K} \langle \tilde{\Phi}_i^a | \hat{H}_{GS}^{eff} | \tilde{\Phi}_j^b \rangle = \\ = \tilde{E}^{GS} + \sum_{ia} (M_{ia}^{K})^2 \left[\tilde{\varepsilon}_a - \tilde{\varepsilon}_i \right] - \sum_{ia}\sum_{jb} M_{ia}^{K*} M_{jb}^{K} \langle \tilde{a}\tilde{i} || \tilde{b}\tilde{j} \rangle \tag{3.70}$$

The second term in (3.69) can be reduced by mean of eq. (3.67) to:

$$\frac{1}{2}\sum_{ia}\sum_{jb} M_{ia}^{K*} M_{jb}^{K} \langle \tilde{\Phi}_i^a | \hat{V}_{PCM}^{GS} | \tilde{\Phi}_j^b \rangle = \\ = \frac{1}{2}\tilde{V}^{GS} q^{GS} + \frac{1}{2}\sum_{ia} (M_{ia}^{K})^2 \left[\langle \tilde{a} | \hat{V}_\sigma | \tilde{a} \rangle - \langle \tilde{i} | \hat{V}_\sigma | \tilde{i} \rangle \right] q^{GS} \tag{3.71}$$

The last term in eq. (3.68), is the analogous to eq.(3.71) for $\hat{V}_{PCM}^{\Delta}$:

$$\frac{1}{2}\sum_{ia}\sum_{jb} M_{ia}^{K*} M_{jb}^{K} \langle \tilde{\Phi}_i^a | \hat{V}_{PCM}^{\Delta} | \tilde{\Phi}_j^b \rangle = \\ = \frac{1}{2}\tilde{V}^{GS} q^{\Delta} + \frac{1}{2}\sum_{ia} (M_{ia}^{K})^2 \left[\langle \tilde{a} | \hat{V}_\sigma | \tilde{a} \rangle - \langle \tilde{i} | \hat{V}_\sigma | \tilde{i} \rangle \right] q^{\Delta} \tag{3.72}$$

Therefore, substituting eqs.(3.70), (3.71) and (3.72) in (3.68) we obtain:

$$\begin{aligned} \mathcal{G}_{CIS}^{K} &= \mathcal{G}^{GS} + \frac{1}{2}\tilde{V}^{GS} q^{\Delta} + \sum_{ia} (M_{ia}^{K})^2 (\tilde{\varepsilon}_a - \tilde{\varepsilon}_i) - \sum_{ia}\sum_{jb} M_{ia}^{K*} M_{jb}^{K} \langle \tilde{a}\tilde{i} || \tilde{b}\tilde{j} \rangle \\ &\quad + \frac{1}{2}\sum_{ia} (M_{ia}^{K})^2 \left[\langle \tilde{a} | \hat{V}_\sigma | \tilde{a} \rangle - \langle \tilde{i} | \hat{V}_\sigma | \tilde{i} \rangle \right] (q^{\Delta} - q^{GS}) \end{aligned} \tag{3.73}$$

$$\begin{aligned} \Delta\mathcal{G}_{CIS}^{K0} &= \sum_{ia} (M_{ia}^{K})^2 (\tilde{\varepsilon}_a - \tilde{\varepsilon}_i) - \sum_{ia}\sum_{jb} M_{ia}^{K*} M_{jb}^{K} \langle \tilde{a}\tilde{i} || \tilde{b}\tilde{j} \rangle \\ &\quad + \frac{1}{2}\sum_{ia} (M_{ia}^{K})^2 \left[\langle \tilde{a} | \hat{V}_\sigma | \tilde{a} \rangle - \langle \tilde{i} | \hat{V}_\sigma | \tilde{i} \rangle \right] q^{\Delta} \end{aligned} \tag{3.74}$$

If we now apply a LR formulation of the CIS method, we can write

$$\Delta\mathcal{G}_{CIS}^{K0} \approx \tilde{\omega}_K^{SCLR} \tag{3.75}$$

where

$$\begin{aligned}\tilde{\omega}_K^{SCLR} &= \sum_{ia}(K_{ia}^K)^2(\tilde{\varepsilon}_a - \tilde{\varepsilon}_i) + \frac{1}{2}\sum_{ia}(K_{ia}^K)^2\left[\langle\tilde{a}|\hat{V}_\sigma|\tilde{a}\rangle - \langle\tilde{i}|\hat{V}_\sigma|\tilde{i}\rangle\right]q^\Delta \\ &\quad -\sum_{ia}\sum_{jb}K_{ia}^{K*}K_{jb}^K\langle\tilde{a}\tilde{i}||\tilde{b}\tilde{j}\rangle \end{aligned} \tag{3.76}$$

and $K = X + Y$ are the eigenvectors of the linear response problem.

We also define in this case:

$$V^\Delta = \sum_{ia}(K_{ia})^2\left[\langle\tilde{a}|\hat{V}_\sigma|\tilde{a}\rangle - \langle\tilde{i}|\hat{V}_\sigma|\tilde{i}\rangle\right] \tag{3.77}$$

The expression in eq. (3.76) can be solved iteratively in a LR fashion, by updating the q^Δ charges, calculated by $\mathbf{P}^\Delta$, and therefore recover the self consistency between V^Δ and q^Δ. The discussion outlined here allows us to identify the term V^Δ to operate an the iteration also for $\mathbf{P}^\Delta$ calculated from the equation of the Z-vector. We implement the iterative procedure in a development version of Gaussian09 [78] suite:

- In the first step the quantity $\tilde{\omega}_K^{SCLR}$ is obtained from the equation of LR-PCM where $\mathcal{V}^{PCM} = 0$ (as described for the cLR scheme). The term $\mathcal{V}^{PCM}$ is not considered later.

- The equations CPKS (through the approach of the Z-Vector) are solved and then we get the "relaxed density matrix" $\mathbf{P}^\Delta$.

- The $\mathbf{P}^\Delta$ is used to calculate q^Δ charges that are stored.

- In the next step, the subroutine that calculate LR-PCM is called, and the diagonal form of V^Δ (see eq. 3.77) is used to achieve an iteration to calculate the new $\tilde{\omega}_K^{SCLR}$ and eigenvectors of Linear Response. These constitue the occ-virt, virt-occ blocks of the new $\mathbf{P}^\Delta$, i.e. $\mathbf{T}^K$.

- The new $\mathbf{P}^\Delta$ is calculated once again by mean of Z-vector equation (where the diagonal term V^Δ is also considered), and used as before to obtain the charges q^Δ.

- The iterative procedure ends when $\tilde{\omega}_K^{SCLR[n]} = \tilde{\omega}_K^{SCLR[n-1]}$

With respect to cLR scheme, eqs. (3.48) or (3.49), our SCLR formulation eq.(3.76) not only permits to achieve the self consistency between charges q^{Δ} and density $\mathbf{P}^{\Delta}$, but it is also possible to take in account the equilibrium or non-equilibrium regime during iteration.
Finally, the expression of V^{Δ}, eq. (3.77) is of the same type of a state specific expression (cfr. eq. (27) and (53) in the analysis of Cammi et al. [188]) and not indirectly recovered as in cLR scheme.

3.6.1 Numerical applications: compairing LR, cLR and SCLR

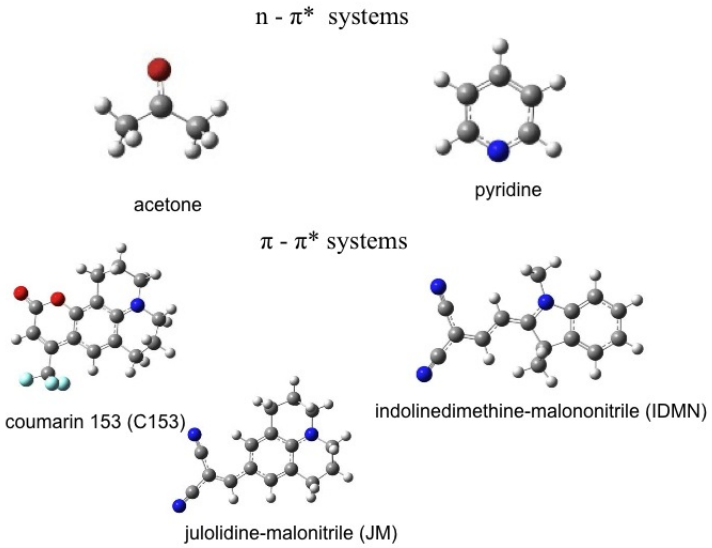

Figure 3.16: Structures of molecular systems studied.

In this section, a preliminary application of the SCLR scheme is reported together with a comparison with respect to cLR and LR calculations. The systems studied are reported in figure 3.16.
Molecular geometries were optimized using the hybrid (27% of HF-X) meta-GGA[6] functional M06 [189] and 6-311+G(2df,2p) basis set in the case of acetone and pyridine, and using the 6-311G(d,p) basis set in the case of coumarin

[6]The meta-GGA it is essentially an extension of the GGA (see section 2.2) in which the non-interacting kinetic energy density is used as input to the functional as well as the electron density and its gradient.

Table 3.9: $n-\pi^*$ **transitions (eV) to the first excited state of acetone and pyridine in n-hexane and solvatochromic shift $\Delta\omega$ (eV) in passing to water. "+ n w" refers to the inclusion of n explicit molecules of water in the calculation.**

	Acetone		
	n-hexane	$\Delta\omega$ wat-hex	$\Delta\omega$ wat+2w-hex
LR	4.51	0.15	0.37
cLR	4.49	0.13	0.36
SCLR	4.47	0.13	0.37
exp[a]		0.23	
	Pyridine		
	n-hexane	$\Delta\omega$ wat-hex	$\Delta\omega$ wat+1w-hex
LR	4.75	0.14	0.31
cLR	4.69	0.13	0.31
SCLR	4.60	0.17	0.36
exp[b]		0.35	

[a] *Ref. [191]*
[b] *Ref. [192]. The value in water is evaluated using averaged values of pyrimidine and pyrazine.*

153 (C153), IDMN and JM. Calculations in solution were carried out using the SMD [190] definition of the cavities implemented in Gaussian 09. Excited state energies and dipoles of all molecular systems were calculated using the M06/6-311+G(2df,2p) combination.
We investigated two type of transitions: $n-\pi^*$(acetone and pyridine) and $\pi-\pi^*$ (C153, JM and IDMN) in polar and non polar solvents: n-hexane and water for acetone and pyridine, cyclohexane and dimethyl sulfoxide for C153 and cyclohexane and acetonitrile (ACN) for JM and IDMN.

In this study, two types of analysis can be made. The first is an internal comparison of the three approaches adopted to analyze the effect of the solvent description on the transitions. The second is a comparison with experimental data. However, it is important to note that the comparison of a model for the vertical excitation energies in solution with respect to experimental data is a problematic issue, since different aspects come into play: the description of the electronic structure of the solute (in this case due to the XC functional

used), dispersion, short range and electrostatic effects.
Assuming that both the effects of the QM level and the dispersion (and other minor nonelectrostatic terms) are not very sensitive to the nature of the solvent, we prefer to conduct our analysis in terms of solvatochromic shifts from apolar to polar solvents, because only electrostatic effects are treated explicitly in all the three adopted approaches. Our considerations are in line with the study of Weijo et Al. [193] which shows that dispersion is a significant contribution to the overall solvent effect, but unlike the electrostatic contribution, it does not depend strongly on the specific solvent. As a result, if one is interested in solvatochromic shifts, results obtained with the electrostatic model often yield satisfactory results in comparison to experimental shifts due to the almost exact cancellation of the dispersion contributions.

In table 3.9 the $n - \pi^*$ transitions of acetone and pyridine in n-hexane and water are reported. For these excitations, one can expect blue shifts moving from apolar to polar solvent because the dipole moment in these molecules substantially decreases upon the electronic excitation (Table 3.6.1), and, therefore, the excited electronic state is solvated less favorably than the ground state.
This expectation is correctly reproduced by all methods and confirmed by experiments. Solvatochromic shifts in acetone can be qualitatively accounted for by considering only dielectric polarization, but in order to get a quantitative agreement in water, hydrogen bonding effects have to be considered. To do that we introduce small solute-solvent clusters in which the water molecules needed to saturate the solute hydrogen bonding sites are included in the QM part of the system while the rest of the solvent is still treated as a continuum dielectric.
If we apply such a cluster description for acetone in water and we include two explicit water molecules, an overestimation of the solvatochromic shift is found.
These findings, however, are in line with the QM/MM/PCM study of Steindal et al.[194]. They show that a satisfactory estimate of the solvent shift is achieved by treating the bulk solvent using PCM, but taking the dynamics of the hydrogen bonding into explicit account . If the latter point is neglected via the use of the supermolecule approach based on the energy-minimized solute-solvent cluster, as in our case, a considerable overestimation of the solvent shift of the $n - \pi^*$ excitation energy is obtained due to the overestimated strength of the solute-solvent hydrogen bonding, i.e. due to the dynamical effect, in average, the interaction could be modeled as less than two water molecules have to be explicitly taken in account.
As a matter of fact, the average of the solvatochromic shifts in the case of zero

and two explicit water molecules is 0.26 eV for LR and 0.25 eV for cLR and SCLR, close to the experimentally estimated one (0.23 eV).
In the case of pyridine, the results obtained with one explicit water molecule taken in account are in good agreement with the experiments. This can be explained considering that for pyridine there is only one strong hydrogen bonding site and in this case the simulation of short-range effects of water by a single hydrogen bonded water molecule is physically correct. The lowest $\pi - \pi^*$ electronic transition of C153, IDMN, and JM is accompanied by a red shift due to an increase of the dipole moment upon the corresponding transition, which makes the excited state more favorably solvated than in the ground state. All the methods yield qualitatively correct predictions of the red shift, as reported in table 3.10.

Moving now to a comparison of the different approaches, we note that for $\pi - \pi^*$ systems the SCLR approach gives the best estimation of the solvatochromic shifts, with the exception of the IDMN case. This is probably due to a more "correlated" solute-solvent polarization description of the solvation energy by SCLR with respect to cLR in this case. This will be more clear introducing an analysis in function of the index δ defined in section 3.3.2 and figure 3.1. By definition, δ values greater than one are associated to a positive correction to LR, and viceversa for $0 < \delta < 1$.

In the case of $n - \pi^*$ transitions, for both molecules the correction of cLR and SCLR with respect to LR is negative, with a decrease of dipole moments in passing from ground to excited state. For these systems, the values of δ index are zero, as the transition dipole moments associated are zero, and this explain the sign of correction. Moreover, from the small values of dipole moment variation ($\Delta\mu_{EXC-GS}$) in table 3.6.1 (cfr. figure 2.1), we can infer that $\omega^{LR} - \omega^{cLR}$ and $\omega^{LR} - \omega^{SCLR}$ are small, in particular in the case of acetone. As a matter of fact, we obtain -0.01 eV (acetone) and -0.04 eV (pyridine) from cLR, and -0.05 eV (acetone) and -0.15 eV (pyridine) for SCLR with respect to LR. In the same line, the solvatochromic shifts of the three approaches are very similar, due to the fact that the correction to the $\mathbf{P}^{\Delta}$ is small for both cLR and SCLR,as we can deduce comparing the $\Delta\mu_{EXC-GS}$ in table 3.6.1.

In the case of $\pi - \pi^*$ transitions, we found an increasing of cLR and SCLR values with respect to LR ones (table 3.10), in line whit the values of δ index reported in table 3.6.1, that are greater than one. We cannot make a direct comparison of δ values between cLR and SCLR, because the $\mathbf{P}^{\Delta}$ matrix obtained is different. However, whitin the same approach, we can see that greater values of solvatochromic shifts are obtained increasing the difference between δ s from apolar to polar solvents. This can explain the value of solvatochromic

Table 3.10: $\pi - \pi^*$ **transitions (eV) to the first excited state of Coumarin 153, IDMN and JM.** $\Delta\omega$ **(eV) are the solvatochromic shifts in passing from cyclohexane to dimethyl solfoxide (DMSO) or to acetonitrile (ACN).**

	C153	
	cyclohexane	$\Delta\omega$ DMSO-cyclohexane
LR	3.24	-0.13
cLR	3.27	-0.16
SCLR	3.39	-0.17
exp[a]		-0.28
	IDMN	
	cyclohexane	$\Delta\omega$ ACN-cyclohexane
LR	3.22	-0.00
cLR	3.38	-0.02
SCLR	3.41	-0.11
exp[b]		-0.05
	JM	
	cyclohexane	$\Delta\omega$ ACN-cyclohexane
LR	3.06	-0.06
cLR	3.20	-0.07
SCLR	3.29	-0.13
exp[c]		-0.12

[a] *Ref. [195]*
[b] *Ref. [145]*
[c] *Ref. [143]*

Table 3.11: **Dipole moment variation (Debye) in passing from ground to excited state ($\Delta\mu_{EXC-GS}$) for $n-\pi^*$ and $\pi-\pi^*$ excitations. LR and SCLR calculations are reported.**

	$n-\pi^*$					
	Non polar solvent			Polar solvent[a]		
		LR	SCLR		LR	SCLR
	μ_{GS}	$\Delta\mu_{EXC-GS}$	$\Delta\mu_{EXC-GS}$	μ_{GS}	$\Delta\mu_{EXC-GS}$	$\Delta\mu_{EXC-GS}$
acetone	3.47	-1.45	-1.33	4.68	-2.08	-1.56
pyridine	2.65	-2.25	-2.63	3.36	-3.04	-2.52

	$\pi-\pi^*$					
	Non polar solvent			Polar solvent		
		LR	SCLR		LR	SCLR
	μ_{GS}	$\Delta\mu_{EXC-GS}$	$\Delta\mu_{EXC-GS}$	μ_{GS}	$\Delta\mu_{EXC-GS}$	$\Delta\mu_{EXC-GS}$
C153	8.36	6.64	5.37	10.33	8.39	5.17
IDMN	12.35	3.14	2.95	15.59	3.27	2.36
JM	13.67	4.40	3.27	17.62	4.60	2.53

[a] *Values reported are dipole moments in water without explicit water molecules included.*

Table 3.12: **Values of the index δ for the $\pi-\pi^*$ excitations of systems studied[a].**

	cLR		SCLR	
	non polar	polar	non polar	polar
C153	1.6	1.1	1.3	1.5
IDMN	37.3	34.1	26.3	43.4
JM	16.1	16.5	17.3	34.6

[a] *Values for acetone and pyridine are not reported, as the transition dipole moments are zero or close to zero for the $n-\pi^*$ first excited state*

shift obtained by SCLR in the case of IDMN, a value analogous to the JM one. In both cases, the value of δ is almost double in passing from cyclohexane to acetonitrile (see table 3.6.1).

To conclude, the corrections to LR due to a better description of the electrostatic solvent effects are expected to be small in the case of vertical excitation energies during the absorption process. In particular, the SCLR correction is always greater than the cLR one, because a larger "correlation" between the molecular and the polarization density of the solvent is introduced. However we can expect that the differences among the different approaches will be more pronounced in the case of emissions, where the LR approach gives a non-physical picture of the processes involved, as it is not possible to take in account a non-equilibrium ground state with a frozen solvent potential due to the excited state. This is not the case of both cLR and SCLR, as in these approaches a state specific description is recovered.

Chapter 4

Conclusions

The whole research presented in this Thesis is adressed to investigate the potentiality of TD-DFT methods and the reliability offered by a combined TD-DFT/PCM approach to determine excitation energies, structures and properties of excited states of molecules in gas phase and in solution. More in detail, this Thesis has focused on two main topics. The first was the critical analysis of TD-DFT methods when applied to the calculation of molecular excited state energies and properties. The goal was to assess the performance of XC functionals and to find diagnostic tools to analyse the achieved results. The first part can be seen as a preliminary step to individuate a good computational protocol whitin the LR-KS scheme to be coupled with the TD-PCM approach to treat solute-solvent interactions in describing excited states of solvated molecules. To this aim, two alternative couplings between TD-DFT and PCM (i.e. LR-PCM and cLR) have been tested to describe charge transfer excitations of large systems in solution and to assess the excitation mechanism in TICT and/or PICT systems. Finally, a new self-consistent strategy (SCLR) for describing solvated excited states has been developed and implemented whitin the TD-DFT method.

In particular, in chapter 2 we have presented an analysis on the performances of the Linear Response (LR) TD-DFT approach in determining electronic excitation energies. The analysis was focused on local or nonlocal changes in the electronic density and on the role played by the Hartree Fock Exchange (HF-X). A new diagnostic index, called Γ,was introduced. It is connected to the difference of the variance of the electronic position moving from occupied to virtual orbitals. Such an index can be seen as the difference between the size of the molecular orbitals involved in the description of the transition, if we represent the *size* by a sphere of radius equal to the root mean square of the distance of the electron in the orbital from the centroid

of charge [76]. Its performances for local, Rydberg and charge-transfer (CT) excitations have been tested. It has been shown how this index can be used as a diagnostic tool for the description of the nature of the excitation studied by different hybrid functionals. In general, it is in fact difficult to achieve a clear and unequivocal picture by only looking at the molecular orbitals involved, especially for large systems. We have compared the new index with the $\mathbf{\Lambda}$ index proposed by Tozer and collaborators [72], which is based on the overlap of the absolute value of the molecular orbitals involved in the excitation, and we have analysed the respective potentialities in achieving a good diagnosis of TDDFT accuracy with Rydberg excitations. In particular, we have shown that the principal effect of increasing the HF-X percentage is to increase orbital energy differences, thus making any analysis based only on the evaluation of the shape and extension of molecular orbitals not sufficient to obtain an exhaustive diagnostic index for TDDFT users. Since in the case of CT excitations in push-pull chromophores (where the ground and excited states are delocalized) we cannot define separated regions for the charge transfer, the Coulombic interactions between the occupied and virtual orbitals (that are described by the nonlocal HF potential) need to be reduced. If the local Coulomb and XC part of the functional are not able to reduce these interactions, smaller errors with respect more correlated methods, are obtained with hybrid functionals presenting low HF-X percentage. This is the case for example of DMABN in the planar structure, IDMN, JM and Prodan, where Λ and Γ have very small values if compared to those typical of Rydberg cases. One can also expect that the Coulomb and the local part of the first order terms in the LR-KS energy become more important in the case of a push pull chromophore, where the transition involves a larger spatial reorganization of charge, but still very delocalized on the molecule. This study suggests that a possible future extension in the direction of more effective diagnostic tools could be represented by localization techniques of the transition density matrix in terms of natural transition orbitals [84].

In the second part of the chapter 2, we have presented a study on the performances of several TD-DFT functionals in describing excited-state geometries and properties for $n - \pi^*$ and $\pi - \pi^*$ valence excitations. There, we have selected small organic systems so to have a direct comparison with CASPT2 data available in the literature. Our study shows that all functionals generally give a qualitatively good description of excitation energies and excited-state structures and properties. For these small molecular systems, it is a general behavior of DFT functionals to overestimate single bond lengths and underestimate the double ones, which means that DFT gives a more lo-

calized picture, with respect to CASPT2, which is known to provide accurate results [196]. For this kind of system, where the electron density reorganization remains relatively limited, the best performances are obtained by using low percentage HF-X hybrids functionals, particularly for carbon-heteroatom double bonds. Higher percentage HF-X functionals and CAM-B3LYP work better in the case of a stronger modification of the electron density after excitation in $n - \pi^*$ and in extended $\pi - \pi^*$ systems. However, the amount of the change of electron density remains too small during the vertical process in the case of small molecules to outperform B3LYP and PBE0, which provide absorption and emission spectra with similar accuracies. Obviously, for transitions with large charge delocalization, as those involved in $\pi - \pi^*$ or $n - \pi^*$ excitations in large conjugated systems or push-pull chromophores [120],[121], as well as for Rydberg excitations [28]-[30],[88],[80], one expects that the inclusion of corrections to the long-range correlation and exchange potential may become mandatory [197], as we found for the case of the three PSB model systems, in particular to reproduce bond length alternation, as yet pointed out for the analogous ground state case [95]. Our constitues, to the best of our knowledge, the first systematic investigations of excited-state structures [32], and it is our intention to extend in a near future our studies to larger systems, including also different types of excitations and solvent effects.

In chapter 3, we have combined the TD-DFT methods studied in chapter 2 with the PCM to study structures and properties of excited-state chromophores in homogeneous solutions. The applications here presented show potentialities and limits of this scheme to probe structures and properties of excited states of solvated chromophores, from their formation from a vertical electronic transition within a nonequilibrium solvation regime up to their decay, or relaxation, using a detailed QM description coherently coupled with the dynamics of the solvent. The results of the study of absorption, emission, structures and resonant Raman spectra computed for two push-pull chromophores (JM and IDMN) have shown the critical role of the functional used and the possibility to achieve better results using a mixed approach to the DFT/TD-DFT part of the calculation, i.e. different functionals for the ground and excited state, respectively. In particular, as alredy pointed out by the study on the TD-DFT performance in reproducing structures and properties of excited states (see chapter 2), the long range correction becomes mandatory to achieve a good description of the shape of the PES of large molecular systems, where in general hybrids functional correctly describe the structure of the ground state (with the exception of particularly delocalized systems). In addition, the importance of this last aspect in solvated systems can be also connected to

the fact that at present only electrostatic solvent effects are included to model excited states.
Another example of the combined effect of TD-DFT and solvation models is represented by the study of the Nile Red system. For such a compound, we have investigated the nature and the structures of the electronic excited states involved in the absorption and emission spectra by using a TD-DFT approach explicitly accounting for solvent effects. It turned out that the functional selected has a major impact not only on the absorption and fluorescence maxima but also on the shape of the potential energy surface obtained through rotation of the amino group. Indeed, with B3LYP, a second minima at nearly perpendicular geometry is obtained. This twisted geometry associated with a strong charge-transfer between the donor and acceptor moieties, corresponds to a TICT mechanism implying a dual fluorescence process originating from two different structures. However, SAC-CI calculations show that this second minimum is a computational artefact. The correct one-minimum shape is reproduced by range separated hybrids, such as CAM-B3LYP. These accurate CAM-B3LYP results indicate that the suggested dual fluorescence in Nile Red is in fact the result of a strongly active vibronic coupling, thus supporting the PICT, rather than the TICT process. These conclusions are in agreement with the most recent spectroscopic studies [169],[186], and also with the negligible viscosity effect on fluorescence properties, inconsistent with the TICT hypothesis [198]. It is our hope that this work nicely illustrates that TD-DFT may allow to take the inner track for investigating complex excited-states mechanisms, once chosen an adequate exchange–correlation functional and a correct description of the solvent effects is taken into account.

Finally, we have proposed a self-consistent state-specific vertical excitation model for electronic excitations in solution, that we called Self Consistent Linear Response (SCLR). This model uses a nonequilibrium formulation of the excited-state reaction field and the excited-state polarization energy. We have called this model "self-consistent" because it evaluates the excited-state reaction field iteratively (i.e. self-consistently), and we have called it "state-specific" because the model computes the excited-state polarization energy by using the excited-state (i.e. state-specific) electronic density.
We tested the two other protocols (LR and cLR) used in this Thesis as approximations to the SCLR approach. We found that more accurate Stokes shift can be obtained using the SCLR/PCM protocol, but the effects of the correction to LR are small in the case of vertical excitation enegies during the absorption process. In particular, the SCLR correction is always greater than the cLR one, because a larger "correlation" between the molecular and the

polarization density of the solvent is introduced. However we can expect that the differences among the various approaches will be more pronounced in the case of emission, where the LR approach gives a non-physical picture of the processes involved, as it is not possible to take into account a non-equilibrium ground state with a frozen solvent potential proper of the excited state. This is not the case of both cLR and SCLR, as in these approaches a state specific description is recovered. Therefore, further extensions of the PCM methodology to study phenomena involving excited electronic states are also expected in the near future, both to overcome some actual limitations and to expand the variety of phenomena to be studied. For example, the SCLR approach here presented (as also the cLR) is now limited to the energy evaluation for single point calculations, and it would be desirable to extend this method to include the analytical gradient, so to be able to compute excited-state equilibrium geometries at this level of theory. In addition, at present, in SCLR (as in cLR case) only electrostatic solvent effects are included in the model used for the excited states; this is a clear approximation that is realistic in polar environments, whereas, as soon as the solvent polarity decreases, further nonelectrostatic effects such as repulsion and dispersion can become important especially when considering excited states.

It is worth noticing that all the solvation models used belong to the continuum framework. This is indeed an approximation in which all the microscopic aspects of the environment are neglected. Recent studies have shown that in many cases this apparently crude approximation properly compares with methods based on the explicit treatment of the environment molecules (such as QM/MM) if a refined version of continuum models is used [199],[200],[201]. Obviously, this is true in the cases in which we do not have strong specific intermolecular interactions between the system of interest and the environment or when these interactions are averaged out in the measurement process. In all the other cases, in fact, a purely continuum approach does not manage to obtain a complete picture of the environment effects. Also in these difficult cases, however, the continuum approach can still represent a simple and effective way to take into account the "mean field" part of the environment effect, whereas all the short-range interactions which do not average to zero, can be introduced by using a "supermolecule" or "cluster" picture. This combined approach in which three different shells are involved (the molecular system under study, the strongly interacting environment molecules and the rest) is indeed very powerful as it accounts not only for both short and long-range effects but can also be easily extended to explicitly include mutual polarization among the various shells once the explicit additional molecules are treated at a QM

level or using a polarizable force field [194]. In addition, the same approach can be extended to a real dynamic description, in which the molecular degrees of freedom of the system of interest are coupled to those of the strongly interacting environment in the presence of the mean field of the remainder. Both these aspects become particularly important when we want to simulate excited states formation and relaxation.

Appendix A

Basis set dependence of excited state structures

Excited state bond lengths, mean values and relative standard deviations are reported in tables A.1 - A.7.
Values are in function of basis set used, namely Pople's 6-31G(d), 6-311G(d) and Dunning's cc-pVDZ, cc-pVTZ, aug-cc-pVDZ, and aug-cc-pVTZ [89].

In general, the introduction of polarization function or triple-zeta basis set expansion gives a shortening of bond lengths, with a dispersion of data around 0.2-0.4 %, as it can be argued by RSD values.
Pyrrole and propenoic acid anion constitute exceptions: in this case values are more basis set dependent with a dispersion of data around 1-2 %. Moreover, the behaviors of functional performances in passing from 6-31G* to AUG-cc-pVTZ are not so regular as in the other systems studied.

Table A.1: **Cis buta-1,3-diene excited state bond lengths (Å) in function of basis set and functional used.**

Basis set	B3LYP	B3P86	PBE0	BMK	BH&HLYP	CAM-B3LYP
			C-C			
6-31+G*	1.420	1.418	1.417	1.426	1.411	1.416
6-31G*	1.424	1.420	1.420	1.428	1.414	1.418
6-311G*	1.421	1.417	1.417	1.425	1.412	1.416
cc-pVDZ	1.426	1.421	1.421	1.430	1.416	1.420
cc-pVTZ	1.417	1.413	1.414	1.422	1.408	1.412
AUG-cc-pVDZ	1.422	1.418	1.418	1.427	1.413	1.417
AUG-cc-pVTZ	1.413	1.411	1.411	1.419	1.405	1.409
average	**1.420**	**1.417**	**1.417**	**1.425**	**1.411**	**1.415**
RSD	**0.003**	**0.002**	**0.002**	**0.002**	**0.002**	**0.003**
			C=C			
6-31+G*	1.406	1.401	1.400	1.405	1.390	1.395
6-31G*	1.406	1.402	1.401	1.405	1.389	1.394
6-311G*	1.402	1.398	1.397	1.400	1.386	1.391
cc-pVDZ	1.407	1.404	1.402	1.407	1.391	1.396
cc-pVTZ	1.397	1.394	1.393	1.396	1.382	1.386
AUG-cc-pVDZ	1.405	1.401	1.400	1.404	1.390	1.395
AUG-cc-pVTZ	1.397	1.393	1.393	1.395	1.382	1.386
average	**1.403**	**1.399**	**1.398**	**1.402**	**1.387**	**1.392**
RSD	**0.003**	**0.003**	**0.002**	**0.003**	**0.002**	**0.003**

Table A.2: **Trans buta-1,3-diene excited state bond lengths (Å) in function of basis set and functional used**

Table A.3: **Pyrrole excited state bond lengths (Å) in function of basis set and functional used.**

Basis set	B3LYP	B3P86	PBE0	BMK	BH&HLYP	CAM-B3LYP
			C-C			
6-31+G*	1.369	1.366	1.365	1.371	1.358	1.362
6-31G*	1.441	1.438	1.436	1.463	1.422	1.428
6-311G*	1.440	1.372	1.435	1.442	1.423	1.359
cc-pVDZ	1.445	1.442	1.440	1.449	1.428	1.433
cc-pVTZ	1.371	1.434	1.433	1.441	1.350	1.425
AUG-cc-pVDZ	1.429	1.426	1.425	1.434	1.421	1.425
AUG-cc-pVTZ	1.422	1.419	1.419	1.427	1.414	1.418
average	**1.417**	**1.414**	**1.422**	**1.432**	**1.402**	**1.407**
RSD	**0.021**	**0.021**	**0.017**	**0.019**	**0.022**	**0.021**
			C=C			
6-31+G*	1.450	1.449	1.446	1.461	1.442	1.448
6-31G*	1.472	1.467	1.465	1.363	1.452	1.459
6-311G*	1.470	1.495	1.463	1.469	1.450	1.491
cc-pVDZ	1.474	1.468	1.466	1.474	1.453	1.460
cc-pVTZ	1.497	1.461	1.460	1.465	1.484	1.453
AUG-cc-pVDZ	1.375	1.372	1.372	1.377	1.367	1.371
AUG-cc-pVTZ	1.371	1.368	1.364	1.368	1.359	1.362
average	**1.444**	**1.440**	**1.434**	**1.425**	**1.430**	**1.435**
RSD	**0.032**	**0.032**	**0.029**	**0.034**	**0.031**	**0.031**
			C-N			
6-31+G*	1.394	1.397	1.387	1.402	1.383	1.391
6-31G*	1.402	1.395	1.394	1.334	1.395	1.401
6-311G*	1.399	1.356	1.390	1.392	1.391	1.367
cc-pVDZ	1.400	1.393	1.391	1.395	1.392	1.398
cc-pVTZ	1.359	1.388	1.386	1.386	1.360	1.392
AUG-cc-pVDZ	1.366	1.361	1.359	1.359	1.354	1.359
AUG-cc-pVTZ	1.357	1.352	1.353	1.351	1.347	1.353
average	**1.382**	**1.377**	**1.380**	**1.374**	**1.374**	**1.380**
RSD	**0.014**	**0.013**	**0.011**	**0.018**	**0.013**	**0.013**

Table A.4: **Acrolein excited state bond lengths (Å) in function of basis set and functional used.**

Basis set	B3LYP	B3P86	PBE0	BMK	BH&HLYP	CAM-B3LYP
			C=O			
6-31+G*	1.293	1.286	1.284	1.284	1.280	1.289
6-31G*	1.292	1.285	1.284	1.284	1.280	1.288
6-311G*	1.284	1.276	1.275	1.277	1.273	1.280
cc-pVDZ	1.287	1.280	1.278	1.279	1.276	1.283
cc-pVTZ	1.282	1.275	1.274	1.275	1.271	1.278
AUG-cc-pVDZ	1.289	1.282	1.281	1.280	1.276	1.284
AUG-cc-pVTZ	1.283	1.275	1.274	1.274	1.278	1.278
average	**1.287**	**1.280**	**1.279**	**1.279**	**1.276**	**1.283**
RSD	**0.003**	**0.003**	**0.003**	**0.003**	**0.002**	**0.003**
			C-C			
6-31+G*	1.392	1.388	1.392	1.420	1.412	1.411
6-31G*	1.391	1.387	1.391	1.419	1.411	1.409
6-311G*	1.388	1.384	1.389	1.415	1.409	1.407
cc-pVDZ	1.393	1.389	1.393	1.421	1.413	1.411
cc-pVTZ	1.385	1.381	1.386	1.413	1.406	1.403
AUG-cc-pVDZ	1.393	1.389	1.393	1.421	1.413	1.412
AUG-cc-pVTZ	1.385	1.382	1.387	1.413	1.404	1.404
average	**1.390**	**1.386**	**1.390**	**1.417**	**1.410**	**1.408**
RSD	**0.002**	**0.002**	**0.002**	**0.002**	**0.002**	**0.002**
			C=C			
6-31+G*	1.388	1.385	1.380	1.371	1.353	1.361
6-31G*	1.385	1.383	1.378	1.369	1.350	1.359
6-311G*	1.384	1.381	1.376	1.365	1.348	1.356
cc-pVDZ	1.388	1.386	1.380	1.372	1.353	1.362
cc-pVTZ	1.381	1.378	1.374	1.362	1.345	1.354
AUG-cc-pVDZ	1.389	1.386	1.381	1.372	1.354	1.362
AUG-cc-pVTZ	1.381	1.378	1.373	1.362	1.353	1.353
average	**1.385**	**1.383**	**1.377**	**1.368**	**1.351**	**1.358**
RSD	**0.002**	**0.002**	**0.002**	**0.003**	**0.002**	**0.003**

Table A.5: **Acetone excited state bond lengths (Å) in function of basis set and functional used.**

Basis set	B3LYP	B3P86	PBE0	BMK	BH&HLYP	CAM-B3LYP
			C=O			
6-31+G*	1.331	1.325	1.320	1.304	1.297	1.315
6-31G*	1.330	1.325	1.320	1.304	1.298	1.314
6-311G*	1.325	1.320	1.315	1.298	1.292	1.309
cc-pVDZ	1.328	1.323	1.318	1.302	1.296	1.313
cc-pVTZ	1.324	1.308	1.308	1.308	1.308	1.308
AUG-cc-pVDZ	1.328	1.323	1.318	1.301	1.295	1.312
AUG-cc-pVTZ	1.322	1.317	1.312	1.295	1.289	1.306
average	**1.327**	**1.320**	**1.316**	**1.302**	**1.296**	**1.311**
RSD	**0.002**	**0.004**	**0.003**	**0.003**	**0.004**	**0.002**
			C-C			
6-31+G*	1.497	1.490	1.491	1.516	1.499	1.499
6-31G*	1.496	1.489	1.490	1.515	1.498	1.497
6-311G*	1.495	1.488	1.489	1.512	1.497	1.496
cc-pVDZ	1.495	1.488	1.489	1.514	1.497	1.497
cc-pVTZ	1.491	1.493	1.493	1.493	1.493	1.493
AUG-cc-pVDZ	1.496	1.489	1.490	1.515	1.500	1.498
AUG-cc-pVTZ	1.491	1.485	1.487	1.512	1.496	1.494
average	**1.494**	**1.489**	**1.490**	**1.511**	**1.497**	**1.496**
RSD	**0.001**	**0.002**	**0.001**	**0.005**	**0.001**	**0.001**

Table A.6: **Diazomethane excited state bond lengths (Å) in function of basis set and functional used.**

Basis set	B3LYP	B3P86	PBE0	BMK	BH&HLYP	CAM-B3LYP
			C-N			
6-31+G*	1.305	1.302	1.297	1.285	1.274	1.291
6-31G*	1.303	1.301	1.296	1.284	1.273	1.289
6-311G*	1.304	1.301	1.296	1.283	1.273	1.290
cc-pVDZ	1.308	1.305	1.300	1.288	1.277	1.294
cc-pVTZ	1.302	1.298	1.294	1.281	1.270	1.287
AUG-cc-pVDZ	1.309	1.305	1.300	1.288	1.278	1.294
AUG-cc-pVTZ	1.301	1.298	1.294	1.280	1.271	1.287
average	**1.305**	**1.301**	**1.297**	**1.284**	**1.274**	**1.290**
RSD	**0.002**	**0.002**	**0.002**	**0.002**	**0.002**	**0.002**
			N-N			
6-31+G*	1.205	1.202	1.201	1.227	1.203	1.204
6-31G*	1.206	1.203	1.202	1.228	1.205	1.205
6-311G*	1.199	1.196	1.196	1.220	1.199	1.198
cc-pVDZ	1.204	1.201	1.201	1.226	1.203	1.203
cc-pVTZ	1.194	1.192	1.192	1.216	1.194	1.194
AUG-cc-pVDZ	1.204	1.201	1.200	1.225	1.202	1.203
AUG-cc-pVTZ	1.193	1.191	1.191	1.215	1.192	1.193
average	**1.201**	**1.198**	**1.198**	**1.222**	**1.200**	**1.200**
RSD	**0.004**	**0.004**	**0.004**	**0.004**	**0.004**	**0.004**

Table A.7: **Propenoic acid anion excited state bond lengths (Å) in function of basis set and functional used.**

Basis set	B3LYP	B3P86	PBE0	BMK	BH&HLYP	CAM-B3LYP
			C-C			
6-31+G*	1.424	1.419	1.417	1.418	1.401	1.407
6-31G*	1.428	1.424	1.420	1.419	1.400	1.408
6-311G*	1.426	1.422	1.419	1.417	1.399	1.407
cc-pVDZ	1.433	1.428	1.424	1.424	1.403	1.413
cc-pVTZ	1.421	1.418	1.415	1.412	1.396	1.403
AUG-cc-pVDZ	1.480	1.421	1.473	1.419	1.402	1.408
AUG-cc-pVTZ	1.475	1.415	1.470	1.482	1.466	1.402
average	**1.441**	**1.421**	**1.434**	**1.427**	**1.409**	**1.407**
RSD	**0.016**	**0.003**	**0.017**	**0.016**	**0.016**	**0.002**
			C=C			
6-31+G*	1.415	1.413	1.410	1.413	1.391	1.400
6-31G*	1.417	1.413	1.411	1.413	1.391	1.401
6-311G*	1.415	1.412	1.410	1.410	1.391	1.400
cc-pVDZ	1.421	1.417	1.415	1.418	1.396	1.406
cc-pVTZ	1.412	1.409	1.407	1.408	1.387	1.396
AUG-cc-pVDZ	1.335	1.413	1.333	1.414	1.392	1.401
AUG-cc-pVTZ	1.325	1.405	1.324	1.324	1.315	1.392
average	**1.391**	**1.412**	**1.387**	**1.400**	**1.380**	**1.399**
RSD	**0.028**	**0.003**	**0.027**	**0.022**	**0.020**	**0.003**
			C-O cis			
6-31+G*	1.295	1.290	1.288	1.288	1.283	1.294
6-31G*	1.292	1.287	1.286	1.287	1.285	1.291
6-311G*	1.288	1.284	1.282	1.282	1.280	1.286
cc-pVDZ	1.290	1.285	1.284	1.284	1.282	1.288
cc-pVTZ	1.287	1.283	1.282	1.281	1.278	1.286
AUG-cc-pVDZ	1.268	1.289	1.262	1.286	1.282	1.293
AUG-cc-pVTZ	1.261	1.283	1.256	1.252	1.247	1.287
average	**1.283**	**1.286**	**1.277**	**1.280**	**1.277**	**1.289**
RSD	**0.010**	**0.002**	**0.009**	**0.009**	**0.010**	**0.002**
			C-O trans			
6-31+G*	1.293	1.286	1.286	1.288	1.287	1.288
6-31G*	1.286	1.281	1.281	1.282	1.282	1.283
6-311G*	1.281	1.277	1.277	1.278	1.279	1.279
cc-pVDZ	1.283	1.279	1.279	1.280	1.280	1.281
cc-pVTZ	1.281	1.277	1.277	1.279	1.279	1.279
AUG-cc-pVDZ	1.260	1.286	1.254	1.287	1.288	1.288
AUG-cc-pVTZ	1.252	1.280	1.246	1.241	1.236	1.282
average	**1.277**	**1.281**	**1.272**	**1.277**	**1.276**	**1.283**
RSD	**0.011**	**0.003**	**0.011**	**0.012**	**0.013**	**0.003**

Appendix B

List of Papers

Part of the material presented in this Thesis has been already published (or is in preparation for publication) in the following papers:

1. **How locally does the electron density change during an electronic excitation: new diagnostic tools and critical analysis**
   C. A. Guido, B. Mennucci and C. Adamo (in preparation)

2. **Practical Computational Methods for Electronic Excitation in Solution: Vertical Excitation Model**
   A. V. Marenich, C. J. Cramer, D. G. Truhlar, C. A. Guido, B. Mennucci, G. Scalmani and M. J. Frisch (Chem. Sci., 2011, Advance Article, DOI: 10.1039/C1SC00313E)

3. **On the TD-DFT Accuracy in Determining Single and Double Bonds in Excited-State Structures of Organic Molecules**
   C. A. Guido, D. Jacquemin, C. Adamo and B. Mennucci, *J. Chem. Phys. A*, **114**, 13402 (2010)

4. **Planar vs. twisted intramolecular charge transfer mechanism in Nile Red: new hints from theory**
   C. A. Guido,B. Mennucci,D. Jacquemin and C. Adamo, *Phys. Chem. Chem. Phys.*, **12**, 8016 (2010)

5. **Structures and Properties of Electronically Excited Chromophores in Solution from the Polarizable Continuum Model Coupled to the Time-Dependent Density Functional Theory**

B. Mennucci, C. Cappelli, C. A. Guido, R. Cammi and J. Tomasi, *J. Chem. Phys. A*, **113**, 3009 (2009)

Bibliography

[1] J. Laane, *Structure and Dynamics of Electronic Excited States* , Springer, 1999.

[2] M. Klessinger and J. Michl, *Excited States and Photochemistry of Organic Molecules* , Wiley-VCH, 1995.

[3] M. Christie, *Colour Chemistry* , The Royal Society of Chemistry, 1971.

[4] L. Serrano-Andreś and M. Merchań, J. Mol. Struct. (THEOCHEM) **729**, 99 (2005).

[5] J. Geertsen, M. Rittby, and R. J. Bartlett, Chem. Phys. Lett. **164**, 57 (1989).

[6] R. J. Bartlett, *Coupled Cluster Theory: An Overview of recent developments*, volume 2 of *Modern Electronic Structure Theory-Part II*, World Scientific, 1995.

[7] H. J. Knowles, P. J.and Werner, Chem. Phys. Lett. **145**, 514 (1988).

[8] P. J. Werner, H. J.and Knowles, J. Chem. Phys. **89**, 5803 (1988).

[9] K. Andersson, P. A. Malmqvist, B. O. Roos, A. J. Sadlej, and K. Wolinski, J. Phys. Chem. **94**, 5483 (1990).

[10] K. Andersson, P. A. Malmqvist, and Roos, J. Chem. Phys. **96**, 1218 (1992).

[11] L. Serrano-Andreś, M. Merchań, I. Nebot-Gil, R. Lindh, and B. O. Roos, J. Chem. Phys. **98**, 3151 (1993).

[12] H. Nakatsuji and K. Hirao, J. Chem. Phys. **68**, 2053 (1978).

[13] T. Nakajima and H. Nakatsuji, Chem. Phys. **242**, 177 (1999).

[14] R. M. Dreizler and E. K. U. Gross, *Density Functional Theory*, Springer-Verlag, 1990.

[15] E. Runge and E. K. U. Gross, Phys. Rev. Lett. **52**, 997 (1984).

[16] M. E. Casida, *Time-Dependent Density Functional Response Theory for Molecules*, volume 1 of *Recent Advances in Density Functional Methods*, World Scientific, 1995.

[17] D. Bohm and D. Pines, Phys. Rev. **92**, 609 (1953).

[18] A. L. Fetter and J. D. Walecka, *Quantum Theory of Many-Particle Systems*, McGraw-Hill, 1971.

[19] C. van Caillie and R. D. Amos, Chem. Phys. Lett. **308**, 249 (1999).

[20] F. Furche and R. Ahlrichs, J. Chem. Phys. **117**, 7433 (2002).

[21] M. Chiba, T. Tsuneda, and K. Hirao, J. Chem. Phys. **124**, 144106 (2006).

[22] N. C. Handy and H. F. Schaefer, J. Chem. Phys. **81**, 5031 (1984).

[23] R. G. Parr and W. Yang, *Density-Functional Theory for Atoms and Molecules*, Oxford Univeristy Press, 1989.

[24] A. Dreuw and M. Head-Gordon, Chem. Rev. **105**, 500 (2005).

[25] M. E. Casida, J. Mol. Struct. (THEOCHEM) **914**, 3 (2009).

[26] D. Jacquemin, V. Wathelet, E. A. Perpète, and C. Adamo, J. Chem. Theory Comput. **5**, 2420 (2009).

[27] M. Caricato, G. W. Trucks, M. J. Frisch, and K. B. Wiberg, J. Chem. Theory Comput. **6**, 370 (2010).

[28] M. A. Rohrdanz and J. M. Herbert, J. Chem. Phys. **129**, 034107 (2008).

[29] L. Goerigk, J. Moellmann, and S. Grimme, Phys. Chem. Chem. Phys. **11**, 4611 (2009).

[30] L. Goerigk and S. Grimme, J. Chem. Phys. **132**, 184103 (2010).

[31] C. A. Guido, B. Mennucci, and C. Adamo, In preparation, J. Chem. Phys. (2011).

[32] C. A. Guido, D. Jacquemin, C. Adamo, and B. Mennucci, J. Phys. Chem. A **114**, 13402 (2010).

[33] R. McWeeny, *Methods of Molecular Quantum Mechanics, Second Edition*, Academic Press, 1992.

[34] P. Hohenberg and W. Kohn, Phys. Rev. **136**, B864 (1964).

[35] M. Levy, Phys. Rev. A **26**, 1200 (1982).

[36] E. H. Lieb, Int. J. Quant. Chem. **24**, 243 (1983).

[37] C. Fiolhais, F. Nogueira, and M. Marques, *A Primer in Density Functional Theory*, Springer-Verlag, 2003.

[38] W. Kohn and L. J. Sham, Phys. Rev. **140**, A1133 (1965).

[39] P. A. M. Dirac, Proc. Cambridge Phil. Soc. **26**, 376 (1930).

[40] D. M. Ceperley and B. J. Alder, Phys. Rev. Lett. **45**, 566 (1980).

[41] S. Vosko, L. Wilk, and M. Nusair, Can. J. Phys./Rev. Can. Phys. **58**, 1200 (1980).

[42] J. P. Perdew and A. Zunger, Phys. Rev. B **23**, 5048 (1981).

[43] L. A. Cole and J. P. Perdew, Phys. Rev. A **25**, 1265 (1982).

[44] J. P. Perdew and Y. Wang, Phys. Rev. B **45**, 13244 (1992).

[45] J. P. Perdew, K. Burke, and M. Ernzerhof, Phys. Rev. Lett. **77**, 3865 (1996).

[46] A. D. Becke, Phys. Rev. A **38**, 3098 (1988).

[47] C. Lee, W. Yang, and R. G. Parr, Phys. Rev. B **37**, 785 (1988).

[48] R. Colle and O. Salvetti, Theor. Chim. Acta **37**, 329 (1975).

[49] B. Miehlich, A. Savin, H. Stoll, and P. H., Chem. Phys. Lett **157**, 200 (1989).

[50] A. D. Becke, J. Chem. Phys. **98**, 5648 (1993).

[51] R. D. Adamson, P. M. W. Gill, and J. A. Pople, Chemical Physics Letters **284**, 6 (1998).

[52] L. A. Curtiss, K. Raghavachari, G. W. Trucks, and J. A. Pople, The Journal of Chemical Physics **94**, 7221 (1991).

[53] L. A. Curtiss, K. Raghavachari, P. C. Redfern, and J. A. Pople, The Journal of Chemical Physics **112**, 7374 (2000).

[54] C. Adamo and V. Barone, J. Chem. Phys. **110**, 6158 (1999).

[55] E. Fermi and E. Amaldi, Accad. Ital. Roma **6**, 119 (1934).

[56] C. Legrand, E. Suraud, and P. G. Reinhard, J. Phys. B **35**, 1115 (2002).

[57] I. Ciofini, H. Chermette, and C. Adamo, Chem. Phys. Lett. **380**, 12 (2003).

[58] A. Savin and H. J. Flad, Int. J. Quant. Chem. **56**, 327 (1995).

[59] A. Savin, page 327, Recent Developments and Applications of Modern Density Functional Theory, Elsevier, 1996.

[60] H. Iikura, T. Tsuneda, T. Yanai, and K. Hirao, J. Chem. Phys. **115**, 3540 (2001).

[61] O. A. Vydrov, J. Heyd, A. Krukau, and G. E. Scuseria, J. Chem. Phys. **125**, 074106 (2006).

[62] J. Song, S. Tokura, T. Sato, M. A. Watson, and K. Hirao, J. Chem. Phys. **127**, 154109 (2007).

[63] T. Yanai, D. P. Tew, and N. C. Handy, Chem. Phys. Lett. **393**, 51 (2004).

[64] M. J. G. Peach, T. Helgaker, P. Salek, T. W. Keal, O. B. Lutnaes, D. J. Tozer, and N. C. Handy, Phys. Chem. Chem. Phys. **8**, 558 (2006).

[65] M. J. G. Peach, A. J. Cohen, and D. J. Tozer, Phys. Chem. Chem. Phys. **8**, 4543 (2006).

[66] D. Jacquemin, E. A. Perpète, G. Scalmani, M. J. Frisch, R. Kobayashi, and C. Adamo, J. Chem. Phys. **126**, 144105 (2007).

[67] J. Song, T. Hirosawa, T. Tsuneda, and K. Hirao, J. Chem. Phys. **126**, 154105 (2007).

[68] L. Ferrighi, L. Frediani, C. Cappelli, P. Salek, H. Agren, T. Helgaker, and K. Ruud, Chem. Phys. Lett. **425**, 267 (2006).

[69] S. Hirata and M. Head-Gordon, Chem. Phys. Lett. **314**, 291 (1999).

[70] C. P. Hsu, S. Hirata, and M. Head-Gordon, J. Phys. Chem. A **105**, 451 (2001).

[71] D. J. Tozer, R. D. Amos, N. C. Handy, B. J. Roos, and L. L. Serrano-Andreś, Mol. Phys. **97**, 859 (1999).

[72] M. J. G. Peach, P. Benfield, T. Helgaker, and D. J. Tozer, J. Chem. Phys. **128**, 044118 (2008).

[73] A. Dreuw, J. L. Weisman, and M. Head-Gordon, J. Chem. Phys. **119**, 2945 (2003).

[74] M. J. G. Peach, P. Benfield, T. Helgaker, and D. J. Tozer, Phys. Chem. Chem. Phys. **11**, 4465 (2009).

[75] T. Ziegler, M. Seth, M. Krykunov, and J. Autschbach, J. Chem. Phys. **129**, 184114 (2008).

[76] M. Robb, W. J. Haines, and I. Csizamadia, J. Am. Chem. Soc. **95**, 42 (1973).

[77] J. Preat, C. Michaux, A. Lewalle, E. A. Perpète, and D. Jaquemin, Chem. Phys. Lett. **451**, 37 (2008).

[78] M. J. Frisch, G. W. Trucks, H. B. Schlegel, G. E. Scuseria, M. A. Robb, J. R. Cheeseman, J. A. Montgomery, Jr., T. Vreven, G. Scalmani, B. Mennucci, V. Barone, G. A. Petersson, M. Caricato, H. Nakatsuji, M. Hada, M. Ehara, K. Toyota, R. Fukuda, J. Hasegawa, M. Ishida, T. Nakajima, Y. Honda, O. Kitao, H. Nakai, X. Li, H. P. Hratchian, J. E. Peralta, A. F. Izmaylov, K. N. Kudin, J. J. Heyd, E. Brothers, V. N. Staroverov, G. Zheng, R. Kobayashi, J. Normand, J. L. Sonnenberg, F. Ogliaro, M. Bearpark, P. V. Parandekar, G. A. Ferguson, N. J. Mayhall, S. S. Iyengar, J. Tomasi, M. Cossi, N. Rega, J. C. Burant, J. M. Millam, M. Klene, J. E. Knox, J. B. Cross, V. Bakken, C. Adamo, J. Jaramillo, R. Gomperts, R. E. Stratmann, O. Yazyev, A. J. Austin, R. Cammi, C. Pomelli, J. W. Ochterski, P. Y. Ayala, K. Morokuma, G. A. Voth, P. Salvador, J. J. Dannenberg, V. G. Zakrzewski, S. Dapprich, A. D. Daniels, M. C. Strain, O. Farkas, D. K. Malick, A. D. Rabuck, K. Raghavachari, J. B. Foresman, J. V. Ortiz, Q. Cui, A. G. Baboul, S. Clifford, J. Cioslowski, B. B. Stefanov, G. Liu, A. Liashenko, P. Piskorz, I. Komaromi, R. L. Martin, D. J. Fox, T. Keith, M. A. Al-Laham, C. Y. Peng, A. Nanayakkara, M. Challacombe, W. Chen, M. W. Wong and

J. A. Pople, **G09 and Gaussian Development Version (GDV), GDVH09, GDVH10, Gaussian, Inc.**, 2009, Wallingford, CT.

[79] A. D. Becke, J. Chem. Phys. **98**, 1372 (1993).

[80] M. Schreiber, M. R. Silva-Junior, S. P. A. Sauer, and W. Thiel, J. Chem. Phys. **128**, 134110 (2008).

[81] K. P. Huber and G. Herzberg, *Constants of Diatomic Molecules, Molecular Spectra and Molecular Structure*, volume 4, Van Nostrand, 1979.

[82] M. E. Casida, C. Jamorski, K. C. Casida, and D. R. Salahub, J. Chem. Phys. **108**, 4439 (1998).

[83] H. H. Falden, K. R. Falster-Hansen, K. L. Bak, S. Rettrup, and S. P. A. Sauer, J. Phys. Chem. A **113**, 11995 (2009).

[84] R. L. Martin, J. Chem. Phys. **118**, 4775 (2003).

[85] J. P. Perdew, Phys. Rev. B **33**, 8822 (1986).

[86] A. D. Boese and J. M. L. Martin, J. Chem. Phys. **121**, 3405 (2004).

[87] D. Jacquemin, E. A. Perpète, I. Ciofini, and C. Adamo, Acc. Chem. Res. **42**, 326 (2009).

[88] I. Ciofini and C. Adamo, J. Phys. Chem. A **111**, 5549 (2007).

[89] T. H. Dunning, J. Chem. Phys. **90**, 1007 (1989).

[90] C. S. Page and M. Olivucci, J. Comput. Chem. **24**, 298 (2002).

[91] O. Valsson and C. Filippi, J. Chem. Theory Comput. **6**, 1275 (2010).

[92] S. Grimme and F. Neese, J. Chem. Phys. **127**, 154116 (2007).

[93] D. Jacquemin, E. A. Perpète, I. Ciofini, C. Adamo, R. Valero, Y. Zhao, and D. G. Truhlar, J. Chem. Theory Comput. **6**, 2071 (2010).

[94] M. Schreiber, V. Bub, and M. P. Fulscher, Phys. Chem. Chem. Phys. **3**, 3906 (2001).

[95] D. Jacquemin, A. Femenias, H. Chermette, I. Ciofini, C. Adamo, J. André, and E. A. Perpète, J. Phys. Chem. A **110**, 5952 (2006).

[96] J. L. Brèdas, Adv. Mater. **7**, 263 (1995).

[97] L. Serrano-Andreś, B. O. Roos, and M. Merchań, Theor. Chim. Acta **87**, 387 (1994).

[98] F. Aquilante, V. Barone, and B. O. Roos, J. Chem. Phys. **119**, 12323 (2003).

[99] A. Munoz Losa, I. Fdez Galva`n, M. Aguilar, and M. E. Martin, J. Phys. Chem. B **111**, 9864 (2007).

[100] J. F. Arenas, I. Lopez-Tocon, J. C. Otero, and J. Soto, J. Am. Chem. Soc. **124**, 1728 (2002).

[101] C. Reichardt, *Solvents and Solvent Effects in Organic Chemistry* , Wiley-VCH, 2003.

[102] C. H. Wang, *Spectroscopy of condensed media.*, Academic Press, 1985.

[103] A. Douhal and J. Santamaria, *Femtochemistry and Femtobiology: Ultrafast Dynamics in Molecular Science*, World Scientific, 2002.

[104] M. Olivucci, *Computational photochemistry*, volume 16 of *Theoretical and Computational Chemistry*, Elsevier, 2005.

[105] M. Persico and G. Granucci, *Photochemistry in Condensed Phase*, Continuum solvation models in chemical physics, from theory to applications, Wiley, 2007.

[106] J. Gao, *Methods and Applications of Combined Quantum Mechanical and Molecular Mechanical Potentials*, volume 7 of *Reviews in Computational Chemistry*, page 119, John Wiley & Sons, Inc., 2007.

[107] R. A. Friesner and V. Guallar, Ann. Rev. Phys. Chem. **56**, 389 (2005).

[108] C. J. Cramer and D. G. Truhlar, Chem. Rev. **99**, 2161 (1999).

[109] J. Tomasi, B. Mennucci, and R. Cammi, Chem. Rev. **105**, 2999 (2005).

[110] B. Mennucci and R. Cammi, editors, *Continuum solvation models in chemical physics, from teory to applications*, Wiley, 2007.

[111] J. Gao, J. Am. Chem. Soc. **116**, 9324 (1994).

[112] R. Rajamani and J. Gao, J. Comput. Chem. **23**, 96 (2002).

[113] K. Coutinho and S. Canuto, J. Chem. Phys. **113**, 9132 (2000).

[114] S. Coutinho, K. Canuto and M. C. Zerner, J. Chem. Phys. **112**, 9874 (2000).

[115] T. Cusati, G. Granucci, and M. Persico, J. Am. Chem. Soc. **133**, 5109 (2011).

[116] J. Kongsted, A. Osted, K. V. Mikkelsen, P. O. Astrand, and O. Christiansen, J. Chem. Phys. **121**, 8435 (2004).

[117] C. R. Jacob, J. Neugebauer, L. Jensen, and L. Visscher, Phys. Chem. Chem. Phys. **8**, 2349 (2006).

[118] I. Fdez Galván, M. L. Sánchez, M. E. Martín, F. J. Olivares del Valle, and M. A. Aguilar, Comp. Phys. Comm. **155**, 244 (2003).

[119] N. Rega, G. Brancato, and V. Barone, Chem. Phys. Lett. **422**, 367 (2006).

[120] B. Mennucci, C. Cappelli, C. A. Guido, R. Cammi, and J. Tomasi, J. Phys. Chem. A **113**, 3009 (2009).

[121] C. A. Guido, B. Mennucci, D. Jacquemin, and C. Adamo, Phys. Chem. Chem. Phys. **12**, 8016 (2010).

[122] J. D. Jackson, *Classical Electrodynamics*, John Wiley Sons, 1998.

[123] S. Miertus, E. Scrocco, and J. Tomasi, J. Chem. Phys. **117**, 55 (1981).

[124] Brebbia, C. A. and Dominguez, J., Appl. Math. Mod. **372**, 1 (1977).

[125] E. Cancès and B. Mennucci, J. Math. Chem. **23**, 309 (1998).

[126] E. Cancès, B. Mennucci, and J. Tomasi, J. Chem. Phys. **107**, 3032 (1997).

[127] V. Barone and M. Cossi, J. Phys. Chem. A **102**, 1995 (1998).

[128] J. Tomasi and M. Persico, Chem. Rev. **94**, 2027 (1994).

[129] C. J. F. Bottcher and P. Bordewijk, *Theory of Electric Polarization, 2nd ed.*, Elsevier, 1978.

[130] L. D. Landau and E. M. Lifshitz, *Electrodynamics of Continuous Media*, Butterworth-Heinemann, 1999.

[131] Y. Georgievskii, C. P. Hsu, and R. A. Marcus, J. Chem. Phys. **110**, 5307 (1999).

[132] R. A. Marcus, J. Chem. Phys. **24**, 966 (1956).

[133] S. I. Pekar, *Introduction into Electronic Theory of Crystals*, Technical Literature Publishers, 1951.

[134] M. A. Aguilar, J. Phys. Chem. A **105**, 10393 (2001).

[135] R. Cammi, S. Corni, B. Mennucci, and J. Tomasi, J. Chem. Phys. **122**, 104513 (2005).

[136] R. Cammi and B. Mennucci, J. Chem. Phys. **110**, 9877 (1999).

[137] M. Cossi and V. Barone, J. Chem. Phys. **115**, 4708 (2001).

[138] S. Corni, R. Cammi, B. Mennucci, and J. Tomasi, J. Chem. Phys. **123**, 134512 (2005).

[139] M. Caricato, B. Mennucci, J. Tomasi, F. Ingrosso, R. Cammi, S. Corni, and G. Scalmani, J. Chem. Phys. **124**, 124520 (2006).

[140] R. Improta, V. Barone, G. Scalmani, and M. J. Frisch, J. Chem. Phys. **125**, 054103 (2006).

[141] G. Scalmani, M. J. Frisch, B. Mennucci, J. Tomasi, R. Cammi, and V. Barone, J. Chem. Phys. **124**, 094107 (2006).

[142] R. Cammi, B. Mennucci, and J. Tomasi, J. Phys. Chem. A **104**, 5631 (2000).

[143] A. M. Moran, D. S. Egolf, M. Blanchard-Desce, and A. M. Kelley, J. Chem. Phys. **116**, 2542 (2002).

[144] A. M. Kelley, Int. J. Quantum Chem. **104**, 602 (2005).

[145] W. Leng, F. Wurthner, and A. Kelley, J. Phys. Chem. A **109**, 1570 (2005).

[146] B. Mennucci, C. Cappelli, R. Cammi, and J. Tomasi, Theor. Chem. Acc. **117**, 1029 (2007).

[147] J. Guthmuller and B. Champagne, J. Chem. Phys. **127**, 164507 (2007).

[148] M. Dierksen and S. Grimme, J. Chem. Phys. **122**, 244101 (2005).

[149] M. Dierksen, *FCFast Ver.1.0*, 2005, Universität Münster, Münster Germany.

[150] S. R. Marder, J. W. Perry, G. Bourhill, C. B. Gorman, B. G. Tiemann, and K. Mansour, Science **261**, 186 (1993).

[151] S. R. Marder, L. T. Cheng, B. G. Tiemann, A. C. Friedli, M. Blanchard-Desche, J. W. Perry, and J. Skindhoj, Science **263**, 511 (1994).

[152] D. R. Kanis, M. A. Ratner, and T. J. Marks, Chem. Rev. **94**, 195 (1994).

[153] D. M. Bishop, Adv. Chem. Phys. **104**, 1 (1998).

[154] B. H. Besler, K. M. Merz, and P. A. Kollman, J. Comput. Chem. **11**, 431 (1990).

[155] C. A. Guido, *Quantum Mechanical Methods for Resonant Raman Scattering of Molecules in Solution.*, Master's thesis, University of Pisa, Pisa Italy, 2007, on-line: http://etd.adm.unipi.it/theses/available/etd-09202007-184159/, in italian.

[156] W. L. Peticolas and T. Rush, J. Comput. Chem. **16**, 1261 (1995).

[157] S.-Y. Lee and E. J. Heller, J. Chem. Phys. **71**, 4777 (1979).

[158] E. J. Heller, R. L. Sundberg, and D. Tannor, J. Phys. Chem. **86**, 1822 (1982).

[159] J. R. Lakowicz, *Topics in Fluorescence Spectroscopy*, Plenum Press, 1992.

[160] D. Basting, D. Ouw, and F. P. Schäfer, Opt. Commun. **18**, 260 (1976).

[161] P. Greenspan, E. P. Mayer, and S. D. Fowler, J. Cell Biol. **100**, 965 (1985).

[162] G. B. Dutt, S. Doraiswamy, and N. Periasamy, J. Chem. Phys. **94**, 5360 (1991).

[163] A. K. Dutta, K. Kamada, and K. Ohta, Photochem. Photobiol. A **93**, 57 (1996).

[164] C. M. Golini, B. W. Williams, and J. B. Foresman, J. Fluoresc. **8**, 395 (1998).

[165] A. K. Dutta, K. Kamada, and K. Ohta, Chem. Phys. Lett. **93**, 57 (1996).

[166] N. Sarkar, K. Das, D. N. Nath, and K. Bhattacharya, Langmuir **10**, 326 (1994).

[167] K. Rotkiewicz, K. H. Grellmann, and Z. R. Grabowski, Chem. Phys. Lett **19**, 315 (1973).

[168] A. Siemiarczuk, Z. R. Grabowski, A. Krowczynski, M. Asher, and M. Ottolenghi, Chemical Physics Letters **51**, 315 (1977).

[169] A. Kawski, P. Bojarski, and B. Kuklinski, Chem. Phys. Lett. **463**, 410 (2008).

[170] A. Datta, D. Mandal, S. K. Pal, and K. Bhattacharyya, J. Phys. Chem. B **101**, 10221 (1997).

[171] K. Rotkiewicz, K. H. Grellmann, and Z. R. Grabowski, Chem. Phys. Lett. **19**, 19 (1973).

[172] K. Rotkiewicz, K. H. Grellmann, and Z. R. Grabowski, Chem. Phys. Lett. erratum **21**, 121 (1973).

[173] W. Rettig, B. Bliss, and K. Dirnberger, Chem. Phys. Lett. **305**, 8 (1999).

[174] K. A. Zachariasse, Chem. Phys. Lett. **320**, 8 (2000).

[175] A. Demeter, S. Druzhinin, M. George, E. Haselbach, J. L. Roulin, and K. A. Zachariasse, Chem. Phys. Lett. **323**, 351 (2000).

[176] K. A. Zachariasse, S. Druzhinin, W. Bosch, and R. Machinek, J. Am. Chem. Soc. **126**, 1705 (2004).

[177] T. Yoshihara, S. Druzhinin, and K. A. Zachariasse, J. Am. Chem. Soc. **126**, 8535 (2004).

[178] C. Hättig, A. Hellweg, and A. Köhn, J. Am. Chem. Soc. **128**, 15672 (2006).

[179] D. Rappoport and F. Furche, J. Am. Chem. Soc. **126**, 1277 (2004).

[180] B. Mennucci, A. Toniolo, and J. Tomasi, J. Am. Chem. Soc. **122**, 10621 (2000).

[181] I. Ciofini, P. P. Lainé, F. Bedioui, and C. Adamo, J. Am. Chem. Soc **126**, 10763 (2004).

[182] L. CamargoDias, R. Custodio, and F. B. T. Pessine, Chem. Phys. Lett. **302**, 505 (1999).

[183] P. O. Tuck, R. C. Mawhinney, and M. Rappon, Phys. Chem. Chem. Phys. **11**, 4471 (2009).

[184] P. Wiggins, J. A. Gareth Williams, and D. J. Tozer, J. Chem. Phys. **131**, 91101 (2009).

[185] F. Santoro, *FCclasses a Fortran 77 code*, see http://village.ipcf.cnr.it.

[186] A. Kawski, B. Kuklinski, and P. Bojarski, Chem. Phys. **359**, 58 (2009).

[187] Y. Tawada, T. Tsuneda, S. Yanagisawa, T. Yanai, and K. Hirao, J. Chem. Phys. **120**, 8425 (2004).

[188] R. Cammi, L. Frediani, B. Mennucci, and K. Ruud, J. Chem. Phys. **119**, 5818 (2003).

[189] Y. Zao and D. G. Truhlar, Theor. Chem. Acc. **120**, 215 (2008).

[190] A. V. Marenich, C. J. Cramer, and D. G. Truhlar, J. Phys. Chem. B **113**, 6378 (2009).

[191] I. Renge, J. Phys. Chem. A **113**, 10678 (2009).

[192] S. F. Mason, J. Chem. Soc. , 1240 (1959).

[193] V. Weijo, B. Mennucci, and L. Frediani, J. Chem. Theory Comput. **6**, 3358 (2010).

[194] A. H. Steindal, K. Ruud, L. Frediani, K. Aidas, and J. Kongsted, J. Phys. Chem. B **115**, 3027 (2011).

[195] M. L. Horng, J. A. Gardecki, A. Papazyan, and M. Maroncelli, J. Phys. Chem. **99**, 17311 (1995).

[196] K. Andersson and B. O. Roos, Int. J. Quantum Chem. **45**, 591 (1992).

[197] R. Burcl, R. D. Amos, and N. C. Handy, Chem. Phys. Lett. **355**, 8 (2002).

[198] A. Cser, K. Nagy, and L. Biczok, Chem. Phys. Lett. **360**, 473 (2002).

[199] F. Santoro, V. Barone, T. Gustavsson, and R. Improta, J. Am. Chem. Soc. **128**, 16312 (2006).

[200] J. Kongsted and B. Mennucci, J. Phys. Chem. A **111**, 9890 (2007).

[201] B. Mennucci, *Solvation models for molecular properties: continuum versus discrete approaches.*, volume 6 of *Solvation Effects on Molecules and Biomolecules: Challenges and Advances in Computational Chemistry and Physics*, Springer, 2008.

Un pensiero...

La pagina finale di una tesi é di solito l'occasione per i ringraziamenti. Trovo, tuttavia, riduttivo usare questo spazio per un mero elenco di tutte le persone che mi sono state accanto durante questi tre anni di perfezionamento alla Scuola Normale...

Nella coinvolgente piena dei miei trascorsi
bruciati dal tempo che non passa mai
ai miei tre "compari" canto il mio bene.

Un saluto si soffi via da queste pagine
alle coscenze di chi mi ha vissuto all'ombra della torre.

Lascio le birre con cui filosofeggiando del vissuto
io e te, Francesco, abbiam cullato le sere.

Al buon Vincenzo, fraterno amico e consigliere
brindo tra le risate appese ai muri.

E il candido affetto di Ilaria terrò nei poster dei miei ricordi,
e le serate con Anna Chiara e Chicca, a farmi monito che non si è mai troppo lontani.

Si dipingeranno le risate sulla vita e i suoi costumi
nel ricordar la mia casa di via Trento.
Del "Purpiceddu", tra il caffè e l'amicizia,
dell'Augusto imperator della chitarra,

Delle gentil "patate berlusconane" e il loro abbraccio,
ho fatto un cesto di rose senza spine.

Riparerò dal vento il soffice dente di Leone
di Claudia e Vincenza,
di Ilaria, di Arianna.

Ai tanti amici che la fortuna copiosa m'ha sbocciato,
tra gli alti e i bassi di Parigi e la Toscana,
che non si cruccino se qui non compare il nome:
Nel mio poema ciascun di voi è ben segnato
Lasciatemi sol riverirvi e ringraziare.

Ma nel mio ultimo rigo di pensiero,
che nasce dal mattino fino a sera,
ci sono il viso e le mani di Simona:
Alla fine, non ero una chimera...

Ciro